PhD-FSTM-2020-37
The Faculty of Sciences, Technology and Medicine

DISSERTATION

Defense held on 31/08/2020 in Luxembourg

to obtain the degree of

DOCTEUR DE L'UNIVERSITÉ DU LUXEMBOURG

EN SCIENCES DE L'INGÉNIEUR

by

Sasan Rafii-Tabrizi
Born on 27 January 1989 in Luxembourg (Luxembourg)

SMART ELECTRICAL AND THERMAL ENERGY SUPPLY FOR NEARLY ZERO ENERGY BUILDINGS

Dissertation defense committee

Prof. Dr.-Ing. Jean-Régis Hadji-Minaglou, Dissertation Supervisor
Professor, Université du Luxembourg

Prof. Dr.-Ing. Frank Scholzen, Chairman
Professor, Université du Luxembourg

Dr.-Ing. Florin Capitanescu
Researcher, Luxembourg Institute of Science and Technology

Dr.-Ing. Patrick Kobou Ngani
Researcher, HeatOnTarget Company

Prof. Dr.-Ing. Stefan Maas, Vice Chairman
Professor, Université du Luxembourg

Abstract

The European Union (EU) intends to reduce the greenhouse gas emissions to 80-95 % below 1990 levels by 2050. To achieve this goal, the EU focuses on higher energy efficiency mainly within the building sector and a share of renewable energy sources (RES) of around 30 % in gross final energy consumption by 2030 [1]. In this context, the concept of nearly zero-energy buildings (nZEB) is both an emerging and relevant research area.

Balancing energy consumption with on-site renewable energy production in a cost-effective manner requires to develop suitable energy management systems (EMS) using demand-side management strategies.

This thesis develops an EMS using certainty equivalent (CE) economic model predictive control (EMPC) to optimally operate the building energy system with respect to varying electricity prices. The proposed framework is a comprehensive mixed integer linear programming model that uses suitable linearised grey box models and purely data-driven model approaches to describe the system dynamics.

For this purpose, a laboratory prototype is available, which is capable of covering most building-relevant types of energy, namely thermal and electrical energy. Thermal energy for space heating, space cooling and domestic hot water is buffered in thermal energy storage systems. A dual source heat pump provides thermal energy for space heating and domestic hot water, whereas an underground ice storage covers space cooling. The environmental energy sources of the heat pump are ice storage or wind infrared sensitive collectors. The collectors are further used to regenerate the ice storage. Photovoltaic panels produce electrical energy which can be stored in a battery storage system. The electrical energy system is capable of selling and buying electricity from the public power grid. The laboratory test bench interacts with a virtual building model which is integrated into the building simulation software TRNSYS Simulation Studio.

The EMS prototype is tested and validated on the basis of various simulations and under close to real-life laboratory conditions. The different test scenarios are generated using the typical day approach for each season.

List of Figures

List of Tables

Contents

Nomenclature

Abbreviations

ACF	Auto correlation function
AHU	Air handling unit
BES	Building energy system
BSS	Battery storage system
CE	Certainty equivalent
DHW	Domestic hot water
DPC	Data predictive control
DR	Demand response
DSHP	Dual source heat pump
DSM	Demand side management
EMS	Energy management system
EPBD	Energy performance of buildings directive
EU	European Union
EV	Electric vehicles
FCU	Fan coil unit
FHS	Floor heating system
GHG	Greenhouse gas
GSHP	Ground source heat pump
HMI	Human machine interface
HVAC	Heating, ventilation, and air conditioning
ICT	Information and communication technologies
IST	Ice storage tank
LTI	Linear time-invariant
ML	Machine learning
MPC	Model predictive control
MPP	Maximum power point
NGO	Non-governmental organisation
NZEB	Nearly zero energy building
PID	Proportional-integral-derivative
P&ID	Piping and Instrumentation Diagram
PCS	Phase change slurry
PV	Photovoltaic
QoS	Quality of Service
PRBS	Pseudo random binary sequence

RBC	Rule based control
RC	Resistive capacitive
RES	Renewable energy sources
RHC	Receding horizon control
RMSE	Root mean squared error
SC	Space cooling
SDE	Stochastic differential equation
SH	Space heating
SOC	State of charge
STC	Standard testing conditionsl
TABS	Thermally activated building structure
TES	Thermal energy storage
WISC	Wind infrared sensitive collector

Indices

a	Ambient
avg	Average
ch	Charge
dch	Discharge
d	Discrete
h	Heater
i	Sampling point
k	Time step
L	Load
lw	Long-wave
OC	Open circuit
SC	Short circuit
slp	Standard load profile
S	Source
t	Time

Parameters

A	Area	[m^2]
$\boldsymbol{A}, \boldsymbol{B}, \boldsymbol{C}, \boldsymbol{D}$	State space matrices	
c	specific thermal capacity	[kWh/kg.K]
dhw	On/off status domestic hot water	
G	Radiation	[kW/m^2]
I	Current	[A]
$\boldsymbol{e}$	Measurement error	
kA	Heat transfer coefficient	[kW/°C]
m	Mass	[kg]
M	Penalty constant	
R	Thermal resistance	[K/kW]
$\boldsymbol{R}$	Covariance matrix	
U	Voltage	[V]
η	Efficiency	[-]
$\boldsymbol{\epsilon}$	Residuals	
$\boldsymbol{Y}$	Vector of output vector	
ρ	Cost penalty	[€/°C][€]
$\boldsymbol{\omega}$	Standard Wiener process	

Binary Decision Variables

$\boldsymbol{buy}$	On/off status electricity import	
$\boldsymbol{sc}$	On/off status space cooling	
$\boldsymbol{sell}$	On/off status electricity export	
$\boldsymbol{sh}$	On/off status space heating	
$\boldsymbol{S}$	On/off status	

Continuous Decision Variables

$\dot{\boldsymbol{P}}$	Electrical power	[kW]
$\dot{\boldsymbol{Q}}$	Thermal power	[kW]
$\boldsymbol{s}$	Slack variable	
$\boldsymbol{SOC}$	State of charge	[-]
$\boldsymbol{T}$	Temperature	[K]
$\boldsymbol{\phi}$	Heating power	[kW]

Chapter 1

Introduction

1.1 Context and Motivation

On 4 November 2016, the European Union (EU) and its member states officially ratified the Paris agreement stating as one of the main goals to keep global warming below 2°C and to pursue efforts to limit it to 1.5°C above pre-industrial levels [6]. To attain these limits, it is mandatory to reduce the GHG emissions by 80-95 % below 1990 levels in 2050 [7]. Residential and commercial buildings make up 36 % of Europe's CO_2 emissions and therefore represent an essential sector [8]. To decarbonise the building sector, the European Parliament approved the energy performance of buildings directive (EPBD) 2010/31/EU [9]. This Directive covers a wide range of policies and supporting measures to help national EU governments improve the energy efficiency of buildings, of which two are of particular relevance for this project:

1. New buildings must be nearly zero energy buildings (NZEB) beginning late 2020, which presupposes the on-site renewable energy production and consumption to be nearly balanced on a yearly basis.

2. Promotion of information and communication technologies (ICT) and smart technologies to ensure buildings operate efficiently.

The points mentioned above are theoretically and practically addressed in a real construction project of an eco-village in Luxembourg City, which aims to demonstrate the feasibility of a sustainable settlement. For this purpose, the One Planet Living framework was adopted, which was created by the non-governmental organisation (NGO) Bioregional during the development of the BedZED eco-village in South London in 2002 [2]. Illustrated on Figure 1.1, this framework provides ten principles that cover all aspects of social, environmental and economic sustainability. The present work focuses on the zero carbon energy principle which emphasises increased energy efficiency in buildings and supply of energy through renewable energy sources (RES). According to the European Energy Roadmap 2050, photovoltaics (PV) and wind power will play an increasing role in coming decades [1]. These RES offer limited predictability and variability, which is a major challenge in an electricity grid where demand and supply must match at all times. To align electricity consumption and electricity production through variable RES, demand response (DR) will play an important role in the future energy system. The U.S. Federal Energy Regulatory Commission defines DR as [10]:

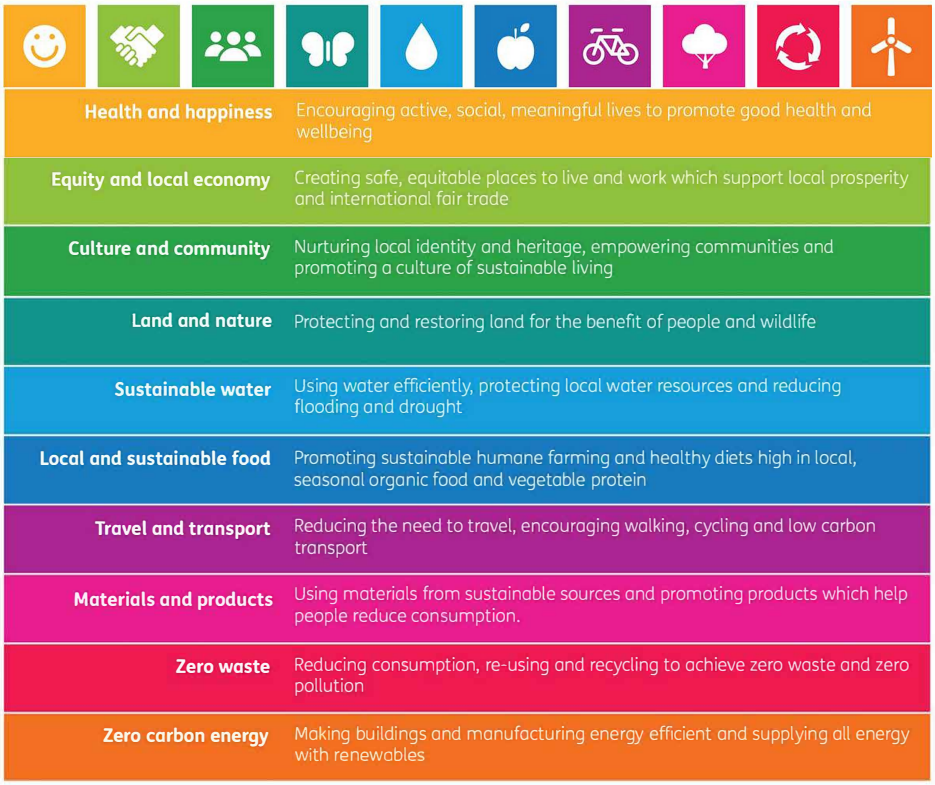

Figure 1.1: Ten One Planet Living Principles [2].

Changes in electric usage by demand-side resources from their normal consumption patterns in response to changes in the price of electricity over time, or to incentive payments designed to induce lower electricity use at times of high wholesale market prices or when system reliability is jeopardized.

Concerning NZEB, DR strategies are implemented with appropriate home energy management systems (HEMS). HEMS enable demand to be shifted or reduced in order to improve the energy consumption and production profile of a building through optimal operational schedules [11]. Model predictions and the fusion of the building energy system (BES) with ICT is crucial for assessing overall flexibility.

This work develops a model predictive controller to investigate DR for a NZEB in a simulative and laboratory setting. The setup encompasses thermal and electrical energy storing and generating devices such as a heat pump, thermal energy storage systems, photovoltaic panels and a battery storage system. The optimal scheduling of the energy system is determined by solving a mixed integer linear programming (MILP) problem formulation, which uses suitable linearization techniques modelling the behaviour of the system components. A major outcome of this work is an elaborate MILP-model of an energy system, whose level of detail is validated under laboratory conditions with a reduced scale energy system. This thesis omits both frequency and voltage control. The investigated control strategies operate in the order of minutes and apply to active power and energy planning.

Research Goals and Outline

The following points summarise the aim of this work:

- Design, planning and construction of an energy system capable of covering any building-relevant types of energy, namely thermal and electrical energy
- Develop suitable models to describe the energy system dynamics in the context of optimal control
- Design of a model predictive controller
- Testing and validating these models through simulations and test runs in the laboratory

The research goals are addressed in the following chapters.

Chapter 2 , 3 and 4 are introductory chapters.

Chapter 2 outlies the idea of economic model predictive control (MPC) with its extension to certainty equivalent (CE) economic MPC.

Chapter 3 provides an overview of the state of the art literature on model predictive control for building energy systems.

Chapter 4 deals with the concept of grey box models and the associated techniques for parameter estimation and state estimation.

Chapter 5 provides the linear dynamic models of thermal and electrical BES components in the framework of a MILP.

Chapter 6 defines the objective function and energy balance of the optimal control problem.

Chapter 7 illustrates the different profiles used in this thesis and the functionality of the model predictive controller.

Chapter 8 assesses the performance of the model predictive controller using a reference scenario. This allows evaluating the potential of DR taking into account variable electricity prices.

Chapter 9 describes the laboratory test bench with its components.

Chapter 10 evaluates the performance of the model predictive controller and the accuracy of the BES models during a test run in the laboratory.

Chapter 11 summarises the conclusions of the different chapters and provides an outlook on future research.

Publications

The following papers were published in conference proceedings and one international journal during the project period:

A Sasan Rafii-Tabrizi, Jean-Régis Hadji-Minaglou, Frank Scholzen, and Florin Capitanescu. Methodology for Optimally sizing a Green Electric and Thermal EcoVillage. In *From Science To Society*. Springer, Cham, 2018. (Accepted) [12]

B Sasan Rafii-Tabrizi, Jean-Régis Hadji-Minaglou, and Frank Scholzen. Mixed integer linear programming model for the optimal operation of a dual source heat pump. *2019 6th International Conference on Control, Decision and Information Technologies, CoDIT 2019*, 2019. (Accepted) [13]

C Sasan Rafii-Tabrizi, Jean-Régis Hadji-Minaglou, Frank Scholzen, and Florin Capitanescu. Optimal Operation of Nearly Zero Energy Buildings using Mixed Integer Linear Programming. In *2019 International Conference on Smart Energy Systems and Technologies (SEST)*, Porto, sep 2019. IEEE. (Accepted) [14]

D Steffen Bechtel, Sasan Rafii-Tabrizi, Frank Scholzen, and Jean-Régis Hadji-Minaglou. Demand-Side-Management Potentials for Heat Pumps in Residential Buildings. In V. et al. Corrado, editor, 16*th International Conference of the International Building Performance Simulation Association*, Rome, 2019. International Building Performance Simulation Association. (Accepted) [15]

E Steffen Bechtel, Sasan Rafii-Tabrizi, Frank Scholzen, Jean-Régis Hadji-Minaglou, and Stefan Maas. Influence of thermal energy storage and heat pump parametrization for demand-side-management in a nearly-zero-energy-building using model predictive control. *Energy and Buildings*, nov 2020. (Accepted) [16]

Chapter 2

Model Predictive Control

Model Predictive Control (MPC) originated in the late seventies with the publications of [17] and [18]. Since then, MPC has not only aroused the interest of the academic world, but has also become the state of the art control approach in process industries [19, 20, 21]. Due to its manifold advantages such as the possibility to formulate constrained problems intuitively, intrinsic compensation for time delays, possible incorporation of forecasts or ability to use multiple variables, MPC is increasingly used to optimally operate energy systems [22, 3, 23, 14, 24, 25].

The essence of MPC is to compute the optimal control action of a process by using a model to predict the system dynamics over a finite horizon. At regular time intervals, a real-time optimisation problem is solved. The main objective of the optimisation problem may be to maximise stakeholders profit, minimise operating costs or minimise the deviation of the process state from a reference trajectory. The solution of the optimisation is a sequence of control inputs of which only the first input is applied to the physical system. The models used to predict the system dynamics are abstractions of the real world process. The variance of the model increases with incremental time steps. For this reason, the process state is repeatedly estimated and updated when a new measurement becomes available. These feedback characteristics of a model predictive controller create a forward shifting horizon. This principle is often referred to as Receding Horizon Control (RHC) as shown in Figure 2.1.

The chapter starts by outlining the idea of economic MPC with its extension to certainty equivalent (CE) economic MPC. Last but not least, a brief overview of state of the art solving methods and solvers is provided.

2.1 Economic Model Predictive Control

In conventional MPC formulations, the objective function ϕ_{sp} penalizes deviations from a given set point $\bar{y}_k$ and $\bar{u}_k$ by summing the weighted squares [21]:

$$\phi_{sp} = \frac{1}{2} \sum_{k=0}^{N-1} \|(y_k - \bar{y}_k)\|_Q^2 + \|(u_k - \bar{u}_k)\|_R^2 \,, \tag{2.1}$$

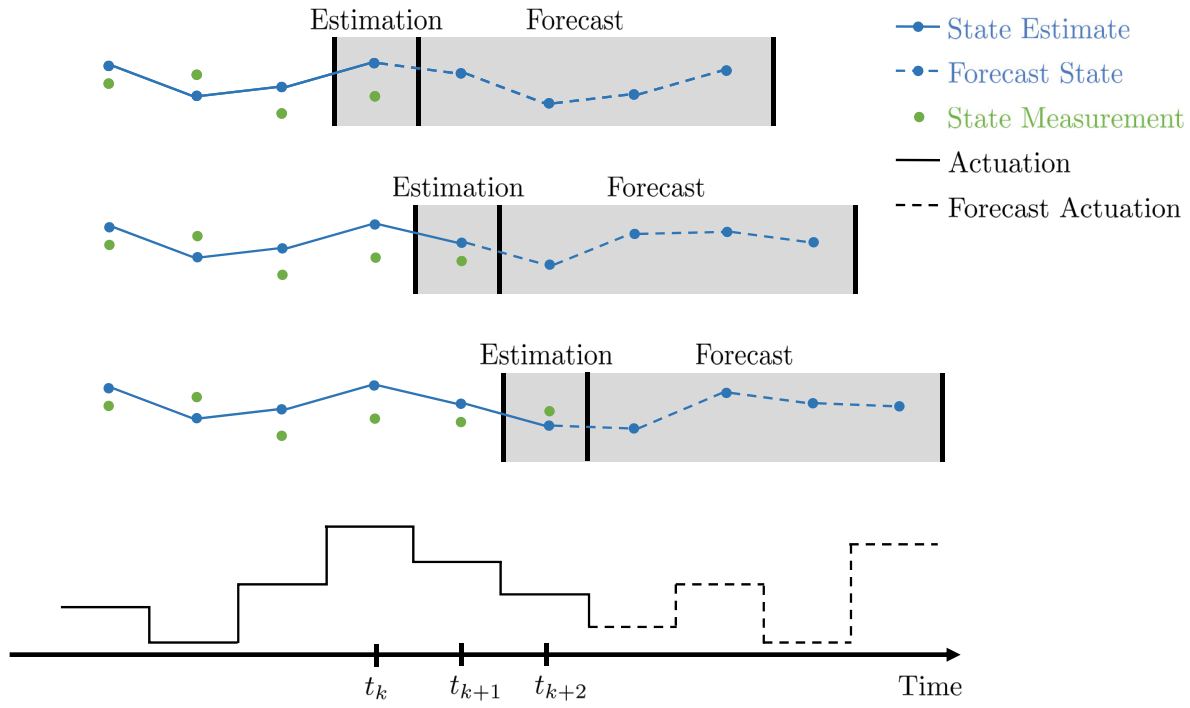

Figure 2.1: A model predictive controller repeatedly applies estimations and forecasts.

where N is the prediction horizon. The matrices Q and R are tuning parameters. Large values of Q in comparison to R drive the state to $\bar{y}_k$ quickly at the expense of large control actions u_k. On the contrary, large values of R relative to Q reduces the speed at which the system reaches a given reference point. Finding the optimal parameters for Q and R is one of the main challenges for industrial applications.

Economic MPC on the other hand, executes an economic optimisation of the process operation. The optimal solution is found by minimising a linear or non-linear economic cost function ϕ_{eco}. The cost function considered in this thesis is linear, with c_k the costs incurred by every control action u_k [26]:

$$\phi_{eco} = \sum_{k=0}^{N-1} c_k^T u_k. \tag{2.2}$$

Certainty Equivalent Economic MPC

A CE assumption is made to handle random variables. This requires that the regulator uses the conditional expectations of the predicted states, disturbances and costs. The conditional mean and covariance matrix of the states is computed using a Kalman filter as illustrated in section 4.4. By using the mean value predictions, the system under investigation becomes deterministic, which significantly reduces the computational burden compared to approaches based on Monte Carlo simulations or uncertainty handling via probability constraints.

Discrete-valued actuators are found in many energy systems due to the on/off behavior of the installed equipment such as heat pumps (HP) or combined heat and power (CHP) units. In many industrial applications, discrete control actions are removed from the MPC control layer. The discrete-valued actuation of the equipment is executed at a low-level control layer of the automation system using heuristic or rule based control (RBC), which generally results in a sub-optimal solution to the control problem. Solving the discrete decisions in the MPC control layer could greatly improve the overall process performance. This argument is supported by the increased computing power and improving mixed-integer solvers in the last years. For this reason, the optimal control problem to be solved in this thesis consists of continuous and discrete control actions. The economic objective function is linearly constrained. Thereby, the problem to be solved is a a mixed integer linear program (MILP).

The MPC regulator determines the optimal control action at time k by minimising the objective function ϕ_{eco}, subject to constraints related to thermal or electrical power production units p and thermal or electrical energy storage systems s [27, 28]. For every time step k a MILP is solved. Only the first input $\hat{u}_{k|k}$ of the control sequence is considered. As new information becomes available, this procedure is repeated.

$$\underset{\hat{u}}{\text{minimise}} \quad \phi_{eco} = \sum_{j=0}^{N-1} \hat{c}_{k+j|k}^{T} \hat{u}_{k+j|k} \tag{2.3a}$$

$$\text{s.t.} \quad \hat{x}_{k+1+j|k} = A_d \hat{x}_{k+j|k} + B_d \hat{u}_{k+j|k} + E_d \hat{d}_{k+j|k}, \tag{2.3b}$$

$$\hat{z}_{k+1+j|k} = C_{d,z} \hat{x}_{k+1+j|k}, \tag{2.3c}$$

$$\hat{r}_{k+1+j|k}^{\min} \leq \hat{z}_{k+1+j|k} \leq \hat{r}_{k+1+j|k}^{\max}, \tag{2.3d}$$

$$u_p^{\min} \hat{S}_{p,k+j} \leq \hat{u}_{p,k+j|k} \leq u_p^{\max} \hat{S}_{p,k+j}, \tag{2.3e}$$

$$\Delta u_p^{\min} \leq \Delta \hat{u}_{p,k+j|k} \leq \Delta u_p^{\max}, \tag{2.3f}$$

$$UT_p(\hat{S}_{p,k+j|k} - \hat{S}_{p,k-1+j|k}) \leq \hat{T}_{p,k+j|k}^{on}, \tag{2.3g}$$

$$DT_p(\hat{S}_{p,k-1+j|k} - \hat{S}_{p,k+j|k}) \leq \hat{T}_{p,k+j|k}^{off}, \tag{2.3h}$$

$$\hat{u}_{s,k+j|k} \leq u_s^{dch,max} \hat{f}_{s,k+j|k} - u_s^{ch,min} \hat{g}_{s,k+j|k}, \tag{2.3i}$$

$$u_s^{dch,min} \hat{g}_{s,k+j|k} - u_s^{ch,max} \hat{f}_{s,k+j|k} \leq \hat{u}_{s,k+j|k}, \tag{2.3j}$$

$$\hat{f}_{s,k+j|k} + \hat{g}_{s,k+j|k} \leq 1. \tag{2.3k}$$

The constraints Eq. (2.3b) and Eq. (2.3c) are the discrete state-space formulation of the process under investigation. Eq. (2.3d) ensures, that the controlled outputs $\hat{z}_{k+1+j|k}$ are bound by lower and upper thresholds. Power generation units are subject to minimum and maximum generation capacity limits in Eq. (2.3e), rate-of-movement constraints $\Delta \hat{u}_{p,k+j|k} = \hat{u}_{p,k-1+j|k} - \hat{u}_{p,k+j|k}$ in Eq. (2.3f), and minimum up and down time limits in Eq. (2.3g) and Eq. (2.3h). $\hat{S}_{p,k+j} \in \{0, 1\}$ is a unit commitment state, which is one when a unit is committed and zero otherwise. UT_p and DT_p are parameters quantifying minimum up time and down time. $\hat{T}_{p,k+j|k}^{on}$ and $\hat{T}_{p,k+j|k}^{off}$ are variables indicating the number of successive on and off hours. Eq. (2.3i) and Eq. (2.3j) apply minimum and maximum charging limits $u_s^{ch,min}$ and $u_s^{ch,max}$ and discharging limits $u_s^{dch,min}$ and $u_s^{dch,max}$ to the energy storage

system. The binary variables $\hat{f}_{s,k+j|k}$ and $\hat{g}_{s,k+j|k}$ indicate whether the system is in charge or discharge mode. Simultaneous charging and discharging of the energy storage unit is made impossible by Eq. (2.3k).

In terms of energy systems, Eq. (2.3d) may translate a desired temperature range for a thermal energy storage system or a room of a building. However, in various situations it turns out to be impossible to maintain the outputs $\hat{z}_{k+1+j|k}$ within the range $\left[\hat{r}^{\min}_{k+1+j|k}, \hat{r}^{\max}_{k+1+j|k}\right]$. To guarantee feasibility of the optimisation during online operation, the hard output constraints in Eq. (2.3d) are softened with a positive slack variable $\hat{s}_{k+1+j|k}$ [29]:

$$\hat{r}^{\min}_{k+1+j|k} - \hat{s}_{k+1+j|k} \leq \hat{z}_{k+1+j|k} \leq \hat{r}^{\max}_{k+1+j|k} + \hat{s}_{k+1+j|k}, \tag{2.4}$$

$$\hat{s}_{k+1+j|k} \geq 0. \tag{2.5}$$

Non-zero values of $\hat{s}_{k+1+j|k}$ are penalized in the objective function with the penalty cost function $\hat{\rho}_{k+j|k}$. Eq. (2.3a) is reformulated as follows:

$$\phi_{eco} = \sum_{j=0}^{N-1} \hat{c}^T_{k+j|k} \hat{u}_{k+j|k} + \hat{\rho}^T_{k+1+j|k} \hat{s}_{k+1+j|k} \tag{2.6}$$

The procedure applied within the certainty equivalent model predictive controller is listed in Algorithm 1. The optimal value for $\hat{u}_{k|k}$ is calculated based on the current measurement y_k, the control action $\hat{u}_{k-1|k-1}$, the state estimate $\hat{x}_{k-1|k-1}$ and state covariance matrix $R^{xx}_{k-1|k-1}$. Further external forecasts are needed to solve the optimal control problem (OCP). With regard to energy systems, $\mathcal{D}_k$,$\mathcal{R}_k$,$\mathcal{F}_k$ can refer to forecasting weather, consumer preferences or electricity market prices. Most of the computing power in Algorithm 1 is consumed by the regulator.

2.2 Solving Mixed Integer Linear Programs

A mixed-integer linear program is a linear program (LP) in which some of the variables are integers. Problems belonging to the LP class are solvable in polynomial time. Common solution techniques for LPs are the simplex algorithm and interior point methods [30, 31]. Unless $\mathbf{P} = \mathbf{NP}$, polynomial time algorithms are not applicable for MILP problems, which are $\mathbf{NP-complete}$ [32]. Instead, linear-programming based branch and bound (B&B) or branch and cut (B&C) algorithms are applied.

Branch and Bound Algorithm

The B&B method originated with the publications of [33] and [34]. The most fundamental concept of the B&B algorithm is the LP-relaxation. In the area of mathematical optimisation, the relaxation of a MILP is the problem that arises when the integrality constraint of the variables is removed. Hence, the resulting relaxation of a MILP becomes a LP with continuous variables. The minimum and maximum values of the variables are the same as in the original model.

Algorithm 1: CE economic MPC

Require:
Input: y_k, $\hat{u}_{k-1|k-1}$, $\hat{d}_{k-1|k}$
Memory: $\hat{x}_{k|k-1}$, $R^{xx}_{k-1|k-1}$
Forecast:

$$\mathcal{D}_k = \left\{\hat{d}_{k+j|k}\right\}_{j=0}^{N-1}, \tag{2.7a}$$

$$\mathcal{R}_k = \left\{\hat{r}^{min}_{k+1+j|k}, \hat{r}^{max}_{k+1+j|k}\right\}_{j=0}^{N-1}, \tag{2.7b}$$

$$\mathcal{F}_k = \left\{\hat{c}_{k+j|k}, \hat{\rho}_{k+1+j|k}\right\}_{j=0}^{N-1}. \tag{2.7c}$$

Prediction Step:

$$\hat{x}_{k|k-1} = A_d\hat{x}_{k-1|k-1} + B_d\hat{u}_{k-1|k-1} + E_d\hat{d}_{k-1|k}, \tag{2.8a}$$

$$R^{xx}_{k|k-1} = A_d R^{xx}_{k-1|k-1} A_d^T + R_1^d. \tag{2.8b}$$

Reconstruction Step:

$$\hat{x}_{k|k} = \hat{x}_{k|k-1} + K_k\left(y_k - C_d\hat{x}_{k|k-1}\right), \tag{2.9a}$$

$$R^{xx}_{k|k} = R^{xx}_{k|k-1} - K_k C_d R_{k|k-1}. \tag{2.9b}$$

Regulator:
Compute $\hat{u}_{k|k} = f(\hat{x}_{k|k}, u_{k-1|k-1}, \mathcal{D}_k, \mathcal{R}_k, \mathcal{F}_k)$ by solving a MILP.
Return:
Control action: $\hat{u}_{k|k}$
Update memory: $\hat{x}_{k|k}$,$R^{xx}_{k|k}$

B&B is recursively breaking down the search space of the original problem into subproblems by using a divide-and-conquer strategy. It involves the construction of a search tree. Each tree node contains the LP relaxation of the original MILP along with some additional constraints for the integer variables. Starting with the root node at the top of the three, there are three possible outcomes [35].

- The LP relaxation problem of the root node is infeasible, which results in an infeasible MILP problem.

- The LP relaxation problem produces an optimal solution where integer constrained variables have integer values. The solution is considered optimal for the MILP problem.

- The LP relaxation problem produces fractional values for at least one integer constrained variable. In the further course of events, one fractional value is considered and two subproblems are created. The first subproblem considers the upper bounding integer of the fractional value as an additional lower bound. The second subproblem considers the lower bounding integer of the fractional value as an additional upper bound.

The size of the search tree grows exponentially. Hence, the explicit enumeration of every node can become computationally intractable at certain point. The strength of the B&B algorithm lies in its ability to skip unnecessary sub-problems. This process is called pruning and is applied as soon as a region of the search space does not contain better solutions than the incumbent one. In a minimisation problem, fractional solutions to LP relaxations are lower bounds whereas integral solutions are as upper bounds. The solution is considered optimal when the difference between the best upper bound and lower bound equals zero.

Branch and Cut Algorithm

The B&C algorithm extends the B&B algorithm. It strengthens the LP relaxation using cutting planes [36, 37]. Linear inequality constraints are added to cut off part of the feasible region of the LP relaxation, without cutting off integer points. As a consequence, it is possible to obtain first of all an integer-feasible solution for the linear relaxation and secondly a better upper bound, which improves the performance of the algorithm. Most of the modern solvers apply the B&C algorithm to solve MILPs optimally.

Solvers

This thesis considers solvers which interface intuitively with Matlab/Simulink and Yalmip [38]. A variety of commercial and open source MILP solvers are available on the market. Leading commercial solvers providing an academic license for students and researchers are Gurobi and Cplex [39, 40]. In this thesis, Gurobi 8.1 is used to solve the MILP problem, as it has proven to be computationally more efficient for this particular application.

Chapter 3

Model Predictive Control for Building Energy Systems

With increasing market penetration of decentralized energy generation and storage facilities, the needs in advanced control systems for a continuous high quality of service (QoS) are growing. Various approaches are being pursued in research in this respect. These deal with improved system control logic, controllers based on artificial neural networks or model predictive control (MPC) [41].

Building energy systems are generally equipped with energy storage systems, limited rated power characterised by time-dependent efficiencies and operating costs [42]. In general, a distinction is made between the building level and the system level. The building level and its related comfort zones provide a thermal capacitance constituted by the building envelope, underfloor heating or thermally activated building structures. Storage of thermal energy on the system level is implemented in different ways such as sensible heat storage, ice storage or the ground. The storage of electrical energy on the system level in a building is usually realized with electrochemical batteries. Other storage systems less common for building applications have mechanical or chemical properties such as flywheels or hydrogen storage [43]. The time dependence of efficiency applies to devices such as heat pumps or dry coolers, where efficiency depends on operating conditions such as temperatures on the primary and secondary side. Time-dependent energy costs apply to electrically operated devices and in some cases to fossil fuel operated devices.

In the following, section 3.1 provides a literature overview of MPC for the building and system level in real world applications. Section 3.2 summarises the findings and draws the necessary conclusions.

3.1 Predictive control at building and system level

Flexibility of building energy systems (BES) is one solution to address the challenges related to market penetration of renewable energies. The flexibility services of BES are provided in various ways, such as thermal mass of storage systems, adjustable HVAC systems, charging/discharging of batteries storage systems (BSS) or electric vehicles (EV) and shiftable loads. Flexibility services with regard to demand response (DR) or demand

side management (DSM) strategies could minimise the power grid congestions, reduce the costs for building stakeholders and increase the energy efficiency of the BES [44]. However, these strategies require more sophisticated predictive control approaches.

A considerable proportion of heating and cooling systems in residential and commercial buildings are controlled with simple binary or proportional-integral-derivative (PID) controllers [41]. Binary controllers are characterised by two switching points and a deadband, which makes them susceptible to overshoots [45]. Properly functioning PID controllers require sensitive tuning of the proportional, integral and derivative terms. However, the performance of PID controllers deteriorates in conditions differing from the PID controller's tuning conditions due do HVAC non-linearities [46].

MPC is known to outperform binary control and PID control approaches in buildings in terms of cost, energy consumption and comfort [3]. Figure 3.1 shows an exemplary comparison between a PID ontroller and MPC. A significant temperature drop at time t_0 leads to an increased heating energy demand. The behaviour of the PID controller shows that it increases the heat supply whenever there is a deviation between the actual value and the setpoint value of the room temperature. Due to the large time constants of the building, the incremental increase in heating power is not sufficient to guarantee thermal comfort. MPC uses a building model and ambient temperature predictions to estimate the time variation of the room temperature. As a consequence, MPC preheats the building before the temperature drop at t_0.

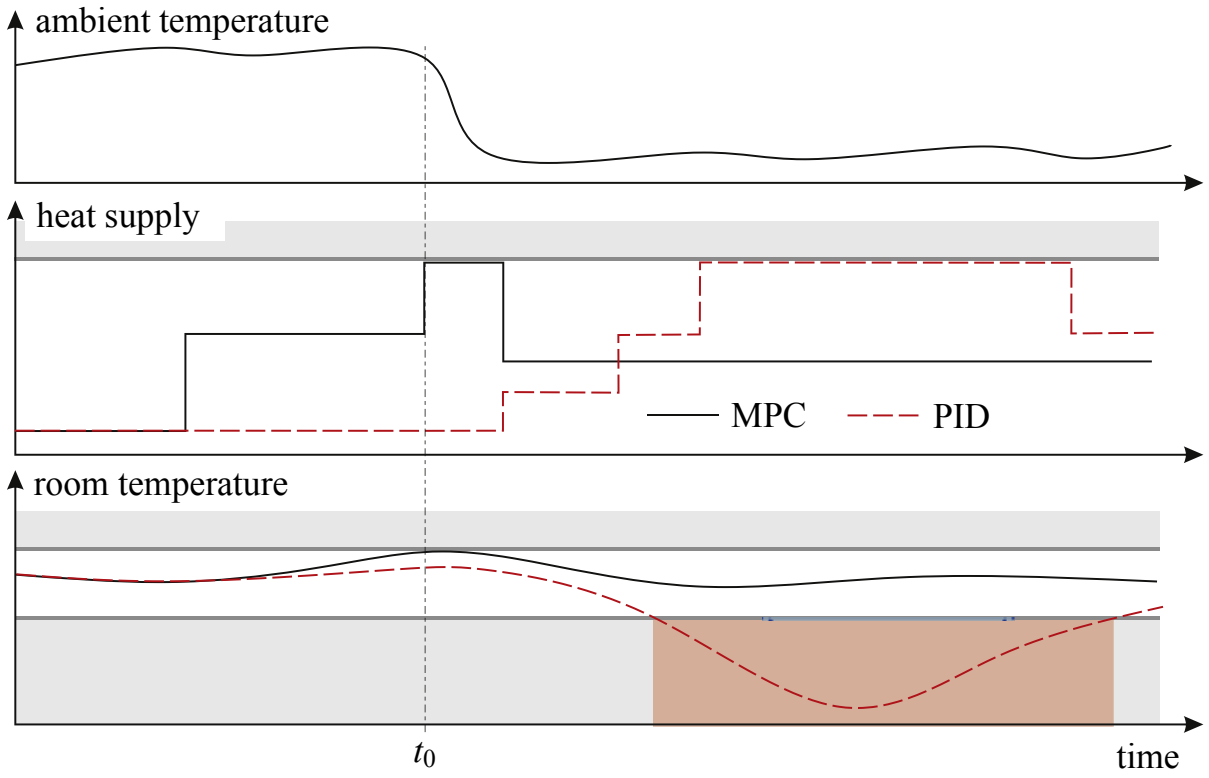

Figure 3.1: Graph illustrating the time series of the ambient temperature, heating power and room temperature for PID control and MPC [3].

Although MPC improves the system performance of buildings from an economic and thermal comfort point of view, practical applications are mainly found in the academic world. The reason for this is the time-consuming and costly identification of adequate building models. Common methods for system identification apply white box, grey box or black box models. A more differentiated distinction between these methods is made in Chapter 4.

MPC formulations that use white-box models in real world applications are scarcely found in the literature. However, [47] implemented a cloud-based white box MPC in a fully occupied office building in Belgium, which is equipped with a thermally activated building structure (TABS) and a ground source heat pump heat pump (GSHP). The control-oriented building model is derived from a detailed building model developed using the Modelica IDEAS library. Non-linearities of the building envelope are are addressed using fix-point linearization. HVAC dynamics and weather disturbances are decoupled from the linearized building model to form a Hammerstein-Wiener model structure. The final linearized state space model has 712 states, 21 inputs and 301 disturbances. MPC computes the optimal heat flows on a building level. The optimal control inputs are subsequently post-processed on a system level by solving a non-linear optimisation problem. The predictive controller is tested during the most challenging heating and cooling seasons. The performance is quantified using a reference scenario, which applies a rule-based control strategy. The final energy savings are 53.5 % and the improvement in thermal comfort is 36.9 %.

[48] and [49] use a grey box oriented MPC approach for an experimental conference room in Bordeaux (France). The room has a surface of 200 m^2 and is equipped with a floor heating system (FHS), three fan coil units (FCU) and a dual-flow air handling unit (AHU). A 5R4C resistive-capacitive (RC) thermal network is used to capture the dynamics of the building, whereby the FHS is described by a single resistive-capacitive node. Building parameters are estimated using an interior-point algorithm to minimise the quadratic sum of the difference between the measured and the simulated indoor temperature. A reduction in the number of parameters to be identified is achieved by using the Morris method, which is a sensitivity analysis method to determine low-impact parameters that have the least influence on the room temperature. The experimental study shows the advantage of predictive control over reference scenarios in terms of comfort and energy savings. The first reference scenario adjusts the flow temperature of the FHS according to a heating curve. The FHS operates continuously. The second reference scenario controls the FHS according to a fixed time schedule that is adapted to the room occupancy. During operation, the flow temperature is also determined using a heating curve. Over the entire heating period, the predictive control achieves an approximate energy saving of 40 % with improved or constant thermal comfort.

In a study by [50] the predictive control of a thermo-electric energy system is validated experimentally. Thermal energy is generated by a heat pump and an auxiliary heating rod. A heat storage tank filled with phase change slurry (PCS) provides thermal energy for space heating (SH) and domestic hot water (DHW). The system has a grid connection point that allows bi-directional power flows. Power electronics emulate a photovoltaic (PV) system with 6 kWp. Tubular lead gel batteries with a useful capacity of 13.65 kWh

enable the local storage of electrical energy. The models of the energy system units are based on first principles laws whose relevant parameters are estimated using a grey box modelling approach. The main objective is to minimise the energy consumption and set-point tracking error. The MPC operates in a supervisory control layer. This means that the calculated energy flows are translated at a lower control level. Finally, the results show an increased self-consumption of PV production and a promising load shifting potential due to energy storage possibilities. Real-time requirements are met without violating the security-relevant functionality.

[51] use a black box oriented data driven model predictive control (DPC) approach for a bedroom in an appartment in Dübendorf (Switzerland). The bedroom has a living area of 17.6 m^2 and a large window area that faces south-east. The entire apartment is equipped with combined heating and cooling ceiling panels, which are supplied with water. The authors use random forest with affine functions and convex optimisation to control the room temperature. The random forest has 200 trees and is trained on 10 months of historical measurement data. The training set contains measurements of the room temperature, weather data, information regarding the time of day and data that potentially has an influence on the room temperature. There is an identical second bedroom in the apartment, which is equipped with a standard hysteresis controller and is used as a reference scenario. The performance of both controllers is compared over a period of six days. DPC achieves energy savings of 24.9 % and reduces it the integral of comfort constraint violations by 72.0 %.

Another machine learning (ML) approach is used by [52] to optimally operate the first floor of a university building in Aquila (Italy). The floor consists of five rooms, four zones and one lobby, which can be controlled individually. A split heat pump supplies every room with heating energy. The authors use neural networks to determine piece-wise affine functions, which can predict energy consumption and temperature. Data collected over a period of 18 weeks are used for training the neural networks. The final MPC problem minimises energy consumption or set point tracking error. In both cases a hysteresis controller is used as reference scenario. The controller reduces energy consumption by dynamically changing the temperature setpoints. Furthermore, by minimising the tracking error, the variance of the rooms temperatures is reduced. In both cases any boundary conditions for thermal comfort are maintained.

3.2 Summary

This chapter has shown how MPC outperforms classical control strategies in real-world applications in terms of cost, energy efficiency and comfort. Different approaches are pursued, all of which having their advantages and disadvantages. White box models accurately represent the dynamics of the building and system level. However, creating these models requires a lot of time, money and expert knowledge. These characteristics make white box models unsuitable for the big-volume market. In contrast, black box MPC reduces the engineering and time required for modeling. Problematic with this approach are the dependence on high-quality training data, lack of interpretability and model deficiencies with longer prediction horizons. Grey box models combine the best

features of white and black box models: physical interpretability and reduced modeling time. The concept of grey box modeling is explained in the subsequent chapter.

Chapter 4

Grey Box Approach to Model System Dynamics

Over the last several decades, a variety of methods have been proposed to model dynamic systems, with the primary objective to predict future responses. These methods can be assigned to different model approaches, namely white box, black box and grey box models [53].

Describing the dynamics of a real-world application in a deterministic manner requires a fundamental understanding of the system and all relevant subprocesses. This is generally realised using first principles laws, i.e. conservation of mass, energy and momentum. Models whose structure and parameters are well known are placed in the category of white box models.
Black box models or so-called input-output models use statistical methods to capture the system dynamics. Such models generally do not have a direct relationship to first principles.
The models proposed in this thesis apply physical information to capture the system dynamics. The determination of the parameters through statistical methods makes possible concrete techno-physical statements about the system. Stochastic terms are added to cope with uncertainties arising from the model formulation and the measurements. On the one hand, the basic structure is derived from the white box models using ordinary differential equations (ODE). The parameters and the uncertainty, on the other hand are obtained using statistical methods. These models are generally called grey box models. The concept is further illustrated on Figure 4.1, showing how grey box models bridge the gap between white box and the black box approaches. The chapter starts by explaining the importance of stochastic differential equations (SDE) in state-space form, the governing equation behind the grey box modelling approach. Further sections introduce the maximum likelihood method for parameter estimation. Subsequently, the concept of state estimation, using the Kalman filter, is introduced. The theoretical principles illustrated in this chapter are presented for linear time-invariant (LTI) systems.

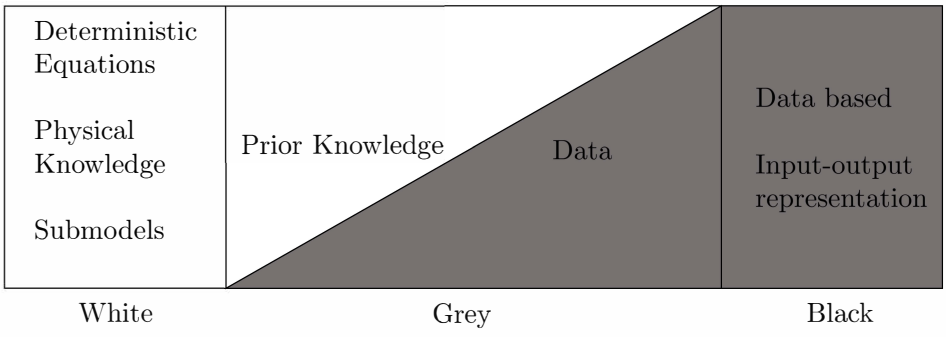

Figure 4.1: Prior knowledge from physics and available data from measured inputs and outputs are combined in a grey box modelling approach [4].

4.1 Linear Stochastic Differential Equations in State Space Form

ODEs are a common tool to describe the dynamics of a physical system. In modern control theory, ODEs are generally formulated using state-space models [21]:

$$d\boldsymbol{X}_t = [\boldsymbol{A}(\boldsymbol{\theta})\boldsymbol{X}_t + \boldsymbol{B}(\boldsymbol{\theta})\boldsymbol{U}_t]\, dt, \tag{4.1}$$

$$\boldsymbol{Y}_k = \boldsymbol{C}(\boldsymbol{\theta})\boldsymbol{X}_k + \boldsymbol{\epsilon}_k, \tag{4.2}$$

where Eq. (4.1) is the system equation describing the time course of the physical states in continuous time and Eq. (4.2) the observation equation that maps the observations to the states in discrete time. Continuous-time is indicated with t and discrete-time with k, respectively. $\boldsymbol{X} \in \mathbb{R}^n$ is a vector of states describing the temporal trajectory of the physics, $\boldsymbol{U} \in \mathbb{R}^m$ the input vector and $\boldsymbol{Y} \in \mathbb{R}^l$ the vector of output variables. The dynamic behaviour of the system is characterised by the matrix $\boldsymbol{A} \in \mathbb{R}^{n\times n}$. $\boldsymbol{B} \in \mathbb{R}^{n\times m}$ specifies how the input signal enters the system and $\boldsymbol{C} \in \mathbb{R}^{l\times n}$ the output matrix that establishes the relationship between the system state with residuals $\boldsymbol{\epsilon} \in \mathbb{R}^l$ and the system output $\boldsymbol{Y}$. $\boldsymbol{\theta} \in \mathbb{R}^q$ are the unknown parameters of the system, which are subsequently determined using the maximum likelihood approach.

The system equation Eq. (4.1) describes a deterministic linear state-space model since it does not account for uncertainty. As a consequence, the residuals $\boldsymbol{\epsilon}$ contain not only the noise part related to model approximations but also the measurement noise. To describe the deviation between Eq. (4.1) and the true variation of the states, it is recommended to make the distinction between process noise, which accounts for model and input approximation, and measurement noise. There are several arguments for introducing process noise: (1) model abstractions, (2) unknown and unmodelled inputs, (3) noise corrupted measurements of the inputs. The measurement noise arises from sensors taking measures affected by noise and drift. Eq. (4.1) and Eq. (4.2) are extended with process and measurement noise, which results in the formulation of SDEs [54]:

$$d\boldsymbol{X}_t = [\boldsymbol{A}(\boldsymbol{\theta})\boldsymbol{X}_t + \boldsymbol{B}(\boldsymbol{\theta})\boldsymbol{U}_t]\, dt + d\boldsymbol{\omega_t}, \tag{4.3}$$

$$\boldsymbol{Y}_k = \boldsymbol{C}(\boldsymbol{\theta})\boldsymbol{X}_k + \boldsymbol{e}_k, \tag{4.4}$$

where $\boldsymbol{\omega}_t \in \mathbb{R}^n$ is a standard Wiener process with incremental covariance $\boldsymbol{R}_{1,t}^c$. The measurement noise $\boldsymbol{e}_k \in \mathbb{R}^l$ is normally distributed with mean 0 and covariance $\boldsymbol{R}_2^c$. It is assumed that the process and measurement noise are uncorrelated.

4.2 From Continuous to Discrete State Space Models

Continuous-time SDEs are unsuitable for numerical evaluation using computers. It is necessary, to transform the continuous-time state-space model into discrete-time. In many cases, this transformation is realised using the method of finite differences. However, the finite difference approach is merely an approximation. Under the assumption, that $\boldsymbol{U}_t$ is constant in a sample interval (zero-order hold), the system evolution between two discrete time steps t and $t+t_s$ can be determined exactly, with t_s the sampling time. The discrete-time state-space model of Eq. (4.3) and Eq. (4.4) is rewritten as following:

$$\boldsymbol{X}_{t+t_s} = \boldsymbol{A}_d \boldsymbol{X}_t + \boldsymbol{B}_d \boldsymbol{U}_t + \boldsymbol{v}_t, \tag{4.5}$$

$$\boldsymbol{Y}_t = \boldsymbol{C}_d \boldsymbol{X}_t + \boldsymbol{e}_t, \tag{4.6}$$

where

$$\boldsymbol{A}_d = e^{\boldsymbol{A}t_s}, \quad \boldsymbol{B}_d = \int_0^{t_s} e^{\boldsymbol{A}s}\boldsymbol{B}ds, \quad \boldsymbol{v}_t = \int_t^{t+t_s} e^{\boldsymbol{B}(t+t_s-s)}d\boldsymbol{\omega}(s), \quad \boldsymbol{C}_d = \boldsymbol{C}. \tag{4.7}$$

Since $\boldsymbol{\omega}_t$ is a Wiener process, $\boldsymbol{v}(t)$ becomes normally distributed white noise with zero mean. The covariance matrix $\boldsymbol{R}_1^d$ of the process noise and covariance of the measurement noise $\boldsymbol{R}_2^d$ are computed as followed:

$$\boldsymbol{R}_1^d = \int_0^{t_s} \boldsymbol{A}_d(s)\boldsymbol{R}_1^c\boldsymbol{A}_d(s)^T ds, \tag{4.8}$$

$$\boldsymbol{R}_2^d = \boldsymbol{R}_2^c t_s. \tag{4.9}$$

Integrals involving the matrix exponential are computed using an algorithm presented by [55].

4.3 Maximum Likelihood Estimation

Maximum Likelihood Estimation (MLE) is a method used to estimate the unknown parameters $\boldsymbol{\theta}$ including the unknown covariance $\boldsymbol{R}_1^c$ of the system equation and the covariance $\boldsymbol{R}_2^c$ of the measurement equation. Considering a given sequence of observation, $\mathcal{Y}_N$ is a matrix containing the observations up to time $t = N$.

$$\mathcal{Y}_N = [Y_N, Y_{N-1}, \ldots, Y_1, Y_0]^T \tag{4.10}$$

The likelihood function is the joint probability distribution of all observations. Successively applying the probability rule $P(A \cap B) = P(A|B)P(B)$ makes it possible to express

the likelihood function L as a product of conditional probability densities of one step ahead predictions. [56]:

$$\begin{aligned} L^T(\boldsymbol{\theta}; \mathcal{Y}_N) &= p(\mathcal{Y}_N|\boldsymbol{\theta}) \\ &= p(\boldsymbol{Y}_N|\mathcal{Y}_{N-1}, \boldsymbol{\theta}) p(\mathcal{Y}_{N-1}|\boldsymbol{\theta}) \\ &= \left(\prod_{t=1}^{N} p(\boldsymbol{Y}_t|\mathcal{Y}_{t-1}, \boldsymbol{\theta}) \right) p(\boldsymbol{Y}_0|\boldsymbol{\theta}). \end{aligned} \tag{4.11}$$

The conditional probability densities are normally distributed since $\boldsymbol{v}_t$ and $\boldsymbol{e}_t$ are normal. The normal distribution is characterised by its mean and variance:

$$\hat{\boldsymbol{Y}}_{t|t-1} = E[\boldsymbol{Y}_t|\mathcal{Y}_{t-1}, \boldsymbol{\theta}], \tag{4.12}$$

$$\boldsymbol{R}_{t|t-1} = V[\boldsymbol{Y}_t|\mathcal{Y}_{t-1}, \boldsymbol{\theta}], \tag{4.13}$$

where $\hat{\boldsymbol{Y}}_{t|t-1}$ is also called the one-step prediction. The one-step prediction error $\boldsymbol{\epsilon}_t$, also referred to as innovation, is then defined as following:

$$\boldsymbol{\epsilon}_t = \boldsymbol{Y}_t - \hat{\boldsymbol{Y}}_{t|t-1}. \tag{4.14}$$

Using Eq. (4.12) - Eq. (4.14), the likelihood function L is reformulated:

$$L\left(\boldsymbol{\theta}; \mathcal{Y}_N\right) = \left(\prod_{t=1}^{N} \frac{\exp\left(-\frac{1}{2}\boldsymbol{\epsilon}_t^\top \boldsymbol{R}_{t|t-1}^{-1} \boldsymbol{\epsilon}_t\right)}{\sqrt{\det\left(\boldsymbol{R}_{t|t-1}\right)}(\sqrt{2\pi})^l} \right) p\left(\boldsymbol{Y}_0|\boldsymbol{\theta}\right) \tag{4.15}$$

where the conditional mean $\hat{\boldsymbol{Y}}_{t|t-1}$ and the conditional variance $\boldsymbol{R}_{t|t-1}$ are recursively computed using a Kalman filter. Finally, the MLE of the unkown parameters $\boldsymbol{\theta}$, is the set of parameters $\hat{\boldsymbol{\theta}}$ that maximises the likelihood function:

$$\hat{\boldsymbol{\theta}} = \underset{\boldsymbol{\theta} \in \Theta}{\arg\max} \left\{ \log\left(L\left(\boldsymbol{\theta}; \mathcal{Y}_N\right)\right) \right\}. \tag{4.16}$$

The parameter estimation problem is solved by using the open-source software CTSM-R [57].

4.4 State Estimation

Knowing the states of a system is vital in many modern control theory problems, such as predicting the future dynamic behaviour of the system using model predictive control (MPC). However, for most applications, it is not possible to determine the full process state $\boldsymbol{X}_t$ by direct measurements. In this context, the concept of observability is introduced.

A system is observable if $\boldsymbol{O}$ has full rank n, with n indicating the number of states in $\boldsymbol{X}_t$. Observability guarantees that all the states $\boldsymbol{X}_t$ can be estimated.

$$\boldsymbol{O} = \begin{bmatrix} C \\ CA \\ CA^2 \\ \vdots \\ CA^{n-1} \end{bmatrix} \tag{4.17}$$

The state estimate of $\boldsymbol{X}_t$ is denoted with $\hat{\boldsymbol{X}}_{t|t}$ and is defined as followed:

$$\hat{\boldsymbol{X}}_{t|t} = E[\boldsymbol{X}_t|\mathcal{Y}_t]. \tag{4.18}$$

$\hat{\boldsymbol{X}}_{t|t}$ is obtained by using the Kalman filter [58]. The Kalman filter is a recursive algorithm, which applies a reconstruction step and prediction step. Given the initial conditions of the state estimate $\hat{\boldsymbol{X}}_{1|0} = \boldsymbol{X}_0$ and state covariance $\boldsymbol{R}^{xx}_{1|0} = \boldsymbol{V}_0$, the reconstruction step is composed of equation Eq. (4.19) and Eq. (4.20):

$$\hat{\boldsymbol{X}}_{t|t} = \hat{\boldsymbol{X}}_{t|t-1} + \boldsymbol{K_t}\left(\boldsymbol{Y}_t - \boldsymbol{C}_d\hat{\boldsymbol{X}}_{t|t-1}\right), \tag{4.19}$$

$$\boldsymbol{R}^{xx}_{t|t} = \boldsymbol{R}^{xx}_{t|t-1} - \boldsymbol{K}_t\boldsymbol{C}_d\boldsymbol{R}^{xx}_{t|t-1}, \tag{4.20}$$

where the Kalman gain $\boldsymbol{K_t}$ is computed by

$$\boldsymbol{K}_t = \boldsymbol{R}^{xx}_{t|t-1}\boldsymbol{C}_d^T\left(\boldsymbol{C}_d\boldsymbol{R}^{xx}_{t|t-1}\boldsymbol{C}_d^T + \boldsymbol{R}^d_2\right)^{-1}. \tag{4.21}$$

The prediction step extrapolates the state estimate and state covariance:

$$\hat{\boldsymbol{X}}_{t+1|t} = \boldsymbol{A}_d\hat{\boldsymbol{X}}_{t|t} + \boldsymbol{B}_d\boldsymbol{U}_t, \tag{4.22}$$

$$\boldsymbol{R}^{xx}_{t|t+1} = \boldsymbol{A}_d\boldsymbol{R}^{xx}_{t|t}\boldsymbol{A}_d^T + \boldsymbol{R}^d_1. \tag{4.23}$$

The Kalman filter estimates the process state $\boldsymbol{X}_t$ for each time step. To do so, the model structure and parameters of the state space model must be known in advance. However, the Kalman filter merely provides the one step prediction. The k-step predictions of the process state and state covariance are determined based on equation Eq. (4.5) and Eq. (4.6):

$$\hat{\boldsymbol{X}}_{t+k+1|t} = \boldsymbol{A}_d\hat{\boldsymbol{X}}_{t+k|t} + \boldsymbol{B}_d\boldsymbol{U}_{t+k}, \tag{4.24}$$

$$\boldsymbol{R}^{xx}_{t+k+1|t} = \boldsymbol{A}_d\boldsymbol{R}^{xx}_{t+k|t}\boldsymbol{A}_d^T + \boldsymbol{R}^d_1. \tag{4.25}$$

Chapter 5

Models for Smart Energy System Units

The components and system topology of a building energy system (BES) determine to a large extent its demand side management (DSM) capabilities. The concept of DSM encompasses all activities aimed at changing the demand profile of the consumer in time and/or form to match supply, while at the same time aiming at the efficient integration of renewable energy sources [59]. Control concepts that include DSM strategies are usually based on optimisation methods [60]. In this chapter, the linear dynamic models of individual BES components are introduced in the framework of a MILP. These components are categorized into thermal & electrical energy generation and storage systems, which are chosen according to a laboratory setup that is described in detail in Chapter 9:

- Dual Source Heat Pump (DSHP)
- Ice Storage Tank (IST)
- Wind Infrared Solar Collector (WISC)
- Thermal Energy Storage (TES) for Space Heating (SH), Domestic Hot Water (DHW) and Space Cooling (SC)
- Battery Storage System (BSS)

The thermal and electrical interconnection of the energy system under investigation is illustrated in Figure 5.1 and 5.2. The demand for space heating and space cooling results from a nearly zero energy building (NZEB) model which is created with TRNSYS Simulation Studio [61]. Internal control of the heat pump decides whether the solar collectors or the ice storage tank is the heat source. Furthermore, solar collectors are used to regenerate the ice storage tank in winter. The dual source heat pump provides thermal energy to space heating and domestic hot water thermal energy storage. The ice storage tank provides natural cooling to space cooling thermal energy storage. PV panels produce electricity from solar radiation. The battery storage system is able to bridge the time delay between electrical energy production and consumption. The energy system is capable of buying/selling electricity from/to the public power grid. Model-specific parameters of prior mentioned components are determined by means of the CTSM-R [1]

[1] Continuous Time Stochastic Modelling for R

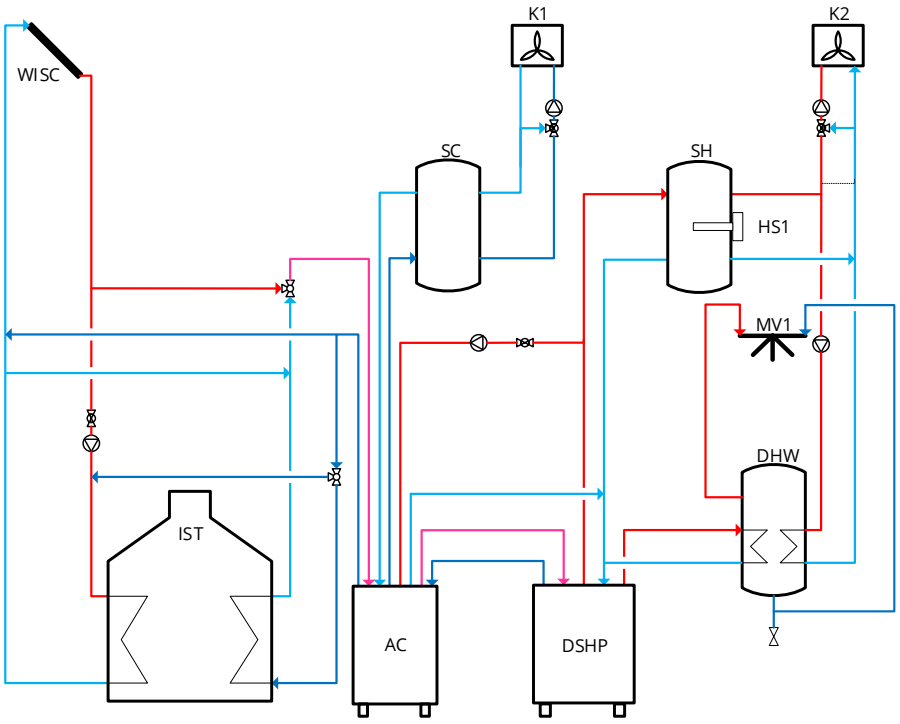

Figure 5.1: Simplified P&ID for smart energy system units.

software, which applies the maximum likelihood estimation method explained in 4.3. Decision variables (binary and continuous) are shown in bold in the remainder of this thesis. The mathematical models partially originate from the publications [13] and [14].

5.1 Dual Source Heat Pump Model

Heat pumps are a highly efficient technology to generate thermal energy for space heating, hot water and space cooling [62]. Two main features are used to categorise heat pumps: (1) thermodynamic cycle and (2) heat source of the evaporator. With regard to the thermodynamic cycle, a distinction is made between vapor compression and absorption. The former requires an electrically operated compressor, whereas the latter uses working fluids with different vapor pressures. Common heat sources for a HP are the ambient air (ASHP), exhaust air (EASHP), ground water (GWSHP), water (WSHP) and ground (GSHP). Within the scope of this thesis, merely electrically driven compressors are considered. The heat sources are an underground IST and WISC. This feature gives to the HP a dual character, hence the designation DSHP. The heat pump under investigation is Viessmann Vitocal 300-G BWC301.B06 with a nominal thermal output of 5600 W at the operating point B0W35 [63]. The Vitocal 300-G BWC301.B06 is a brine-to-water HP which does not have electrical power modulation capability.

Depending on the heat source and modulation capability, different mathematical for-

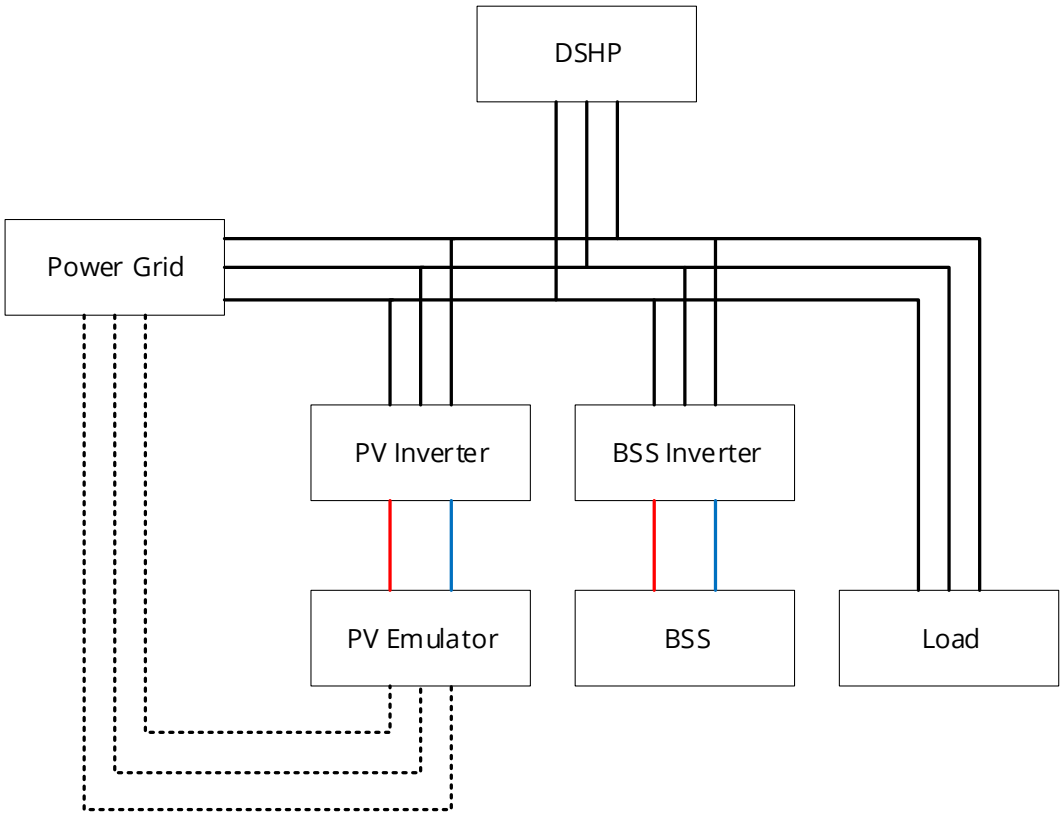

Figure 5.2: Three-phase electrical bus topology for smart energy system units.

mulations have to be applied. In this context, [64, 65, 66] study the optimal control of brine-to-water heat pumps with borehole heat exchangers and solar regeneration. To determine the thermal power output on the load side and the electrical power consumption, a multivariate linear regression model is applied according to [67]. The explanatory variables are mass flow rates and inlet temperatures of the source and load side. [68] uses economic MPC to optimally operate the floor heating system (FHS) of a building. Assuming constant ground temperatures, the GSHP dynamics are captured using a constant coefficient of performance (COP) approach. Further analytic linear and non-linear models are applicable to link at time t the electrical power consumption $\dot{\boldsymbol{P}}_t$, the thermal power on the source side $\dot{\boldsymbol{Q}}_{S,t}$ and load side $\dot{\boldsymbol{Q}}_{L,t}$ to the inlet temperatures on the source side $\boldsymbol{T}_{S,in,t}$ and load side $\boldsymbol{T}_{L,in,t}$.

This thesis proposes a data-driven approach, where the values of $\dot{\boldsymbol{P}}_t$, $\dot{\boldsymbol{Q}}_{S,t}$, $\dot{\boldsymbol{Q}}_{L,t}$, $\boldsymbol{T}_{S,in,t}$ and $\boldsymbol{T}_{L,in,t}$ are represented as a linear combination of the corresponding sampling points $\dot{P}_i$, $\dot{Q}_{S,i}$, $\dot{Q}_{L,i}$, $T_{S,in,i}$ and $T_{L,in,i}$, which are illustrated in the performance map in Figure 5.3. A positive variable $\boldsymbol{\theta}_i \in [0, 1]$ is associated with each sampling point i to enable a linear combination between points. The DSHP dynamics are linearly characterised as follows:

$$\dot{\boldsymbol{P}}_t = \sum_i \boldsymbol{\theta}_{i,t} \dot{P}_i, \tag{5.1}$$

$$\dot{\boldsymbol{Q}}_{S,t} = \sum_i \boldsymbol{\theta}_{i,t} \dot{Q}_{S,i}, \tag{5.2}$$

$$\dot{\boldsymbol{Q}}_{L,t} = \sum_i \boldsymbol{\theta}_{i,t} \dot{Q}_{L,i}, \tag{5.3}$$

$$\boldsymbol{T}_{S,in,t} = \sum_i \boldsymbol{\theta}_{i,t} T_{S,in,i}, \tag{5.4}$$

$$\boldsymbol{T}_{L,in,t} = \sum_i \boldsymbol{\theta}_{i,t} T_{L,in,i}, \tag{5.5}$$

$$1 = \sum_i \boldsymbol{\theta}_{i,t}, 0 \leq \boldsymbol{\theta}_{i,t}. \tag{5.6}$$

The heat pump operates in two discrete on/off modes, which are indicated by the binary variable $\boldsymbol{S}_{DSHP,t} \in \{0,1\}$. Simultaneous heating of the SH and DHW TES is not possible. Even though the natural cooling process does not require the compressor of the heat pump to be switched on, simultaneous heating and cooling is technically not possible. This constraint is mathematically expressed using the following equation:

$$\boldsymbol{S}_{SH,t} + \boldsymbol{S}_{DHW,t} + \boldsymbol{S}_{SC,t} = \boldsymbol{S}_{DSHP,t}, \tag{5.7}$$

where the binary variables $\boldsymbol{S}_{SH,t} \in \{0,1\}$, $\boldsymbol{S}_{DHW,t} \in \{0,1\}$ and $\boldsymbol{S}_{SC,t} \in \{0,1\}$ indicate whether the DSHP is in SH, DHW or SC mode. The dual source heat pump provides thermal power to the space heating and domestic hot water TES. This is mathematically expressed using Eq. (5.8) and (5.9), which couple the temperatures of space heating TES $\boldsymbol{T}_{SH,t}$ and DHW TES $\boldsymbol{T}_{DHW,t}$ to the heat pump inlet temperature $\boldsymbol{T}_{L,in,t}$. During the natural cooling process the space cooling TES temperature $\boldsymbol{T}_{SC,t}$ is equivalent to the inlet temperature $\boldsymbol{T}^{+}_{IST,in,t}$ of the IST regeneration heat exchanger. These conditions are mathematically expressed using the following equations:

$$-\left(1 - \boldsymbol{S}_{SH,t}\right) M_{SH} \leq \boldsymbol{T}_{SH,t} - \boldsymbol{T}_{L,in,t} \leq \left(1 - \boldsymbol{S}_{SH,t}\right) M_{SH}, \tag{5.8}$$

$$-\left(1 - \boldsymbol{S}_{DHW,t}\right) M_{DHW} \leq \boldsymbol{T}_{DHW,t} - \boldsymbol{T}_{L,in,t} \leq \left(1 - \boldsymbol{S}_{DHW,t}\right) M_{DHW}, \tag{5.9}$$

$$-\left(1 - \boldsymbol{S}_{SC,t}\right) M_{SC} \leq \boldsymbol{T}_{SC,t} - \boldsymbol{T}^{+}_{IST,in,t} \leq \left(1 - \boldsymbol{S}_{SC,t}\right) M_{SC}, \tag{5.10}$$

where M_{SH}, M_{DHW} and M_{SC} are sufficiently large penalty constants.

The inlet temperature $\boldsymbol{T}_{S,in,t}$ of the heat pump is determined by the temperature level of the environmental energy source. The binary variables $\boldsymbol{S}_{WISC->DSHP,t} \in \{0,1\}$ and $\boldsymbol{S}_{IST->DSHP,t} \in \{0,1\}$ indicate whether solar collectors or ice storage tank is the heat source:

$$\begin{aligned} -\left(1 - \boldsymbol{S}_{WISC->DSHP,t}\right) M_{WISC->DSHP,t} &\leq \boldsymbol{T}_{S,in,t} - \boldsymbol{T}_{WISC,out,t} \\ &\leq \left(1 - \boldsymbol{S}_{WISC->DSHP,t}\right) M_{WISC->DSHP}, \end{aligned} \tag{5.11}$$

$$\begin{aligned} -\left(1 - \boldsymbol{S}_{IST->DSHP,t}\right) M_{IST->DSHP} &\leq \boldsymbol{T}_{S,in,t} - \boldsymbol{T}^{-}_{IST,out,t} \\ &\leq \left(1 - \boldsymbol{S}_{IST->DSHP,t}\right) M_{IST->DSHP}, \end{aligned} \tag{5.12}$$

with $\boldsymbol{T}_{WISC,out,t}$ and $\boldsymbol{T}^{-}_{IST,out,t}$ the outlet temperatures of WISC and IST extraction heat exchanger. M_{SH}, M_{DHW} and M_{SC} are sufficiently large penalty constants.

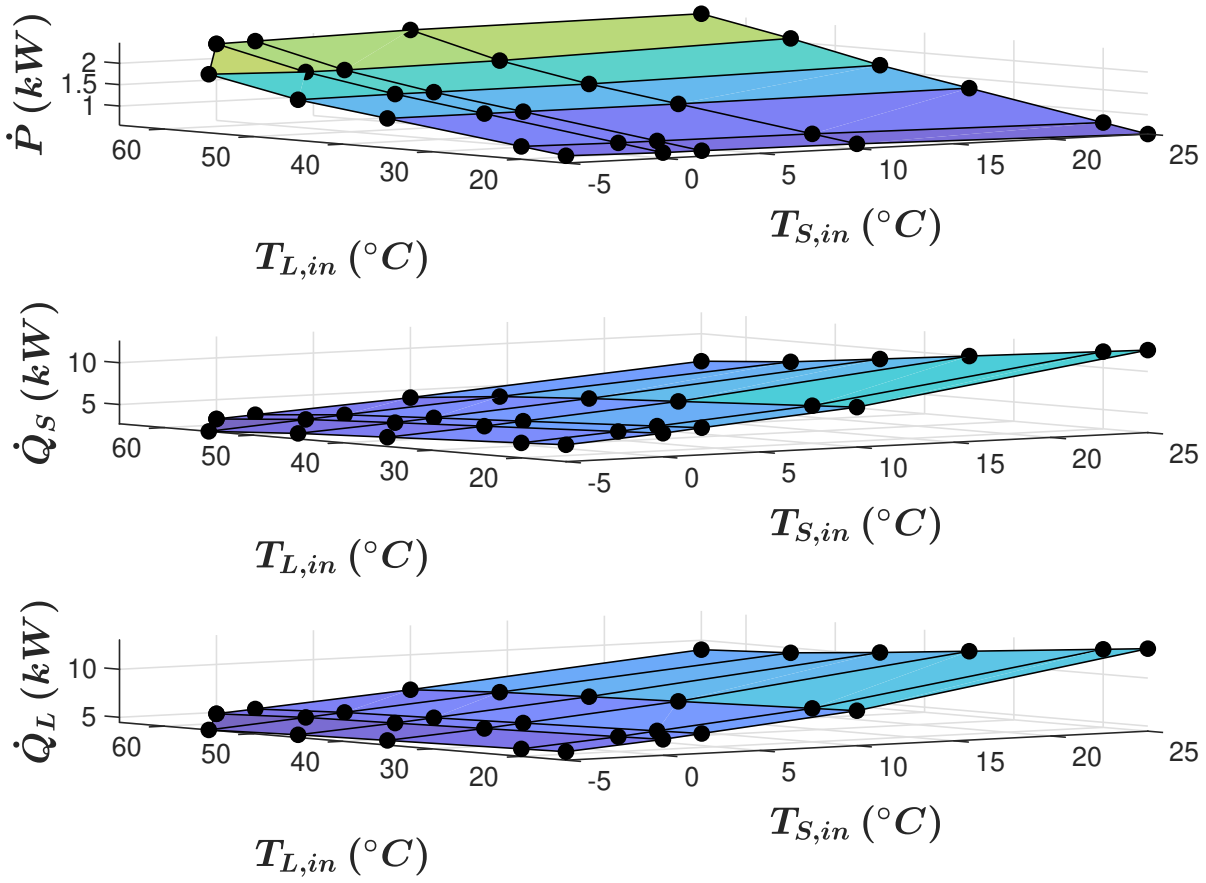

Figure 5.3: Vitocal 300-G BWC301.B06 performance map illustrating the dependence of electrical power and thermal power vs inlet temperatures.

5.2 Ice Storage Model

The ice storage tank is an underground concrete cistern, which has a cylindrical shape. The IST is in thermal exchange with the surrounding soil. It is equipped with two heat exchangers, which are used for regeneration and environmental energy source for the heat pump. Regeneration and heat extraction is achieved with two heat coils made of polyethylene (PE). The content of the ice storage tank is water with mass m_{IST}, whose phase changing properties take effect at 0°C. The IST under investigation is a Viessmann Vitofriocal type ES-B 10.

MPC formulations of ice storage tanks in connection with dual source heat pumps are scarcely found in the literature. However, [69, 70, 71] apply predictive control strategies of electric chillers and ice tanks to provide cooling energy to buildings. The ice storage tank model used in prior mentioned studies is based on the approach developed by [72]. The IST is considered as a system of heat exchangers, whose charging and discharging heat transfer effectiveness depends on the state of charge (SOC). The charging and discharging effectiveness were curve fit using cubic and quintic polynomial functions respectively, which results in a non-linear and non-convex optimisation problem. Simultaneous charging and discharging of the IST is not considered.

In this thesis, a state space model is applied to describe the thermal dynamics of the IST. The state $\boldsymbol{H}_{IST,t}$ is the IST enthalpy. $\Delta\boldsymbol{T}_t^+ = 0.5\left(\boldsymbol{T}_{IST,in,t}^+ + \boldsymbol{T}_{IST,out,t}^+\right)$ and $\Delta\boldsymbol{T}_t^- = 0.5\left(\boldsymbol{T}_{IST,in,t}^- + \boldsymbol{T}_{IST,out,t}^-\right)$ describe the arithmetic mean heat exchanger temperatures. The underground tank is thermally connected to the surrounding soil at temperature $T_{grd,t}$, the heat pump and the solar collectors. To determine the enthalpy, an energy balance approach is used. The temperature $\boldsymbol{T}_{IST,t}$ is homogeneously distributed inside the IST. Ice formation on the heat exchangers is neglected under the assumption that a decrease in thermal transmittance is compensated with an increased heat exchanger surface [73]. The following system equation is used to describe the heat dynamics of the tank:

$$\begin{aligned} d\boldsymbol{H}_{IST,t} = \Bigg(& \frac{1}{m_{IST} R_{IST}^{loss}} \left(T_{grd,t} - \boldsymbol{T}_{IST,t}\right) + \frac{kA^+}{m_{IST}} \left(\Delta\boldsymbol{T}_t^+ - \boldsymbol{T}_{IST,t}\right) \\ & + \frac{kA^-}{m_{IST}} \left(\Delta\boldsymbol{T}_t^- - \boldsymbol{T}_{IST,t}\right) \Bigg) dt + d\omega_{IST,t}, \end{aligned} \tag{5.13}$$

where R_{IST}^{loss} is the thermal resistance between the IST and the surrounding soil. kA^+ and kA^- designate the heat transfer coefficient of the regeneration and extraction heat exchanger respectively. $\omega_{IST,t}$ is a Wiener process with incremental covariance σ_1^2.

Phase changing properties of the water are described using an enthalpy-temperature correlation. The phase change process is represented with a temperature glide [73]. The temperature-enthalpy correlation is established using the sampling points in Table 5.1. Values lying in between these sampling points are determined through linear interpolation

Table 5.1: Temperature enthalpy sampling points

Temperature (° C)	Enthalpy (J/kg.K)
$T_1 = -10$	$H_1 = -10 \cdot 2060$
$T_2 = -3$	$H_2 = -3 \cdot 2060$
$T_3 = 0$	$H_3 = 3.35 \cdot 10^5$
$T_4 = 20$	$H_4 = 20 \cdot 4180 + 3.35 \cdot 10^5$

using positive weights $\boldsymbol{\lambda}_{t,i}$. The sum of these is equal to one:

$$\boldsymbol{\lambda}_{1,t} + \boldsymbol{\lambda}_{2,t} + \boldsymbol{\lambda}_{3,t} + \boldsymbol{\lambda}_{4,t} = 1 \tag{5.14}$$

The enthalpy-temperature correlation is finally computed with Eq. (5.15) and Eq. (5.16):

$$\boldsymbol{T}_{IST,t} = \boldsymbol{\lambda}_{1,t} T_1 + \boldsymbol{\lambda}_{2,t} T_2 + \boldsymbol{\lambda}_{3,t} T_3 + \boldsymbol{\lambda}_{4,t} T_4 \tag{5.15}$$

$$\boldsymbol{H}_{IST,t} = \boldsymbol{\lambda}_{1,t} H_1 + \boldsymbol{\lambda}_{2,t} H_2 + \boldsymbol{\lambda}_{3,t} H_3 + \boldsymbol{\lambda}_{4,t} H_4 \tag{5.16}$$

Furthermore, special ordered sets 2 (SOS2) are used for all weights, which implies that not more than two adjacent weights are non-zero.

Table 5.2: Parameter estimates of the IST

Parameter	Estimate	Units
m_{IST}	9989	kg
c_{IST}	$1.67 \cdot 10^{-3}$	$kWh/kg.K$
R_{IST}^{loss}	7.04	K/kW
kA^{+}	0.72	kW/K
kA^{-}	1.14	kW/K
σ_1	$7.01 \cdot 10^{-2}$	$°C$
σ_2	$9.10 \cdot 10^{-3}$	$°C$

Parameter Estimation Ice Storage Model

Enthalpy is a physical quantity that cannot be measured directly. For this reason, Eq. (5.17) is rewritten so that the enthalpy state variable is replaced by the temperature of the IST, with c_{IST} the thermal capacity:

$$\begin{aligned}\boldsymbol{T}_{IST,t} = \Bigg(& \frac{1}{m_{IST} c_{IST} R_{IST}^{loss}} \left(T_{grd,t} - \boldsymbol{T}_{IST,t}\right) + \frac{kA^{+}}{m_{IST} c_{IST}} \left(\Delta \boldsymbol{T}_t^{+} - \boldsymbol{T}_{IST,t}\right) \\ & + \frac{kA^{-}}{m_{IST} c_{IST}} \left(\Delta \boldsymbol{T}_t^{-} - \boldsymbol{T}_{IST,t}\right) \Bigg) dt + d\omega_{IST,t}.\end{aligned} \tag{5.17}$$

The measured state variable is the tank temperature $\boldsymbol{T}_{IST,t}$. The observation equation is written as follows:

$$Y_k = \boldsymbol{T}_{IST,k} + e_k, \tag{5.18}$$

with e_k the measurement noise of the temperature sensor. It is assumed that e_k is normally distributed white noise with zero mean and variance σ_2^2. Due to the large thermal mass, the time frame of the project did not allow to cover cover the entire temperature range. For this reason, the data used to estimate the parameters m_{IST}, c_{IST}, R_{IST}^{loss},kA^{+},kA^{-}, σ_1 and σ_2 originate from the simulation software Polysun, which provides a validated Viessmann tank model [74]. The time series used to estimate the parameters is shown in Figure 5.4. The numerical values of the parameter estimates are presented in Table 5.2.

5.3 Wind Infrared Sensitive Collector Model

The wind infrared sensitive collector is an unglazed solar absorber whose main purpose is twofold: (1) provide environmental energy to the DSHP and (2) regenerate the IST. WISC consists of two layers of PE-pipes and is especially sensitive to wind speed u_t and longwave radiation $G_{lw,t}$. The absorber used in the laboratory setup work is emulated with the help of an electric flow heater. This allows to run different test series independent of the weather. The flow heater emulates an absorber from Viessmann type SLK-S.

There are three main categories of solar collectors namely glazed flat plate collectors, vacuum tube collectors and unglazed collectors [75, 76]. The efficiency of the former two

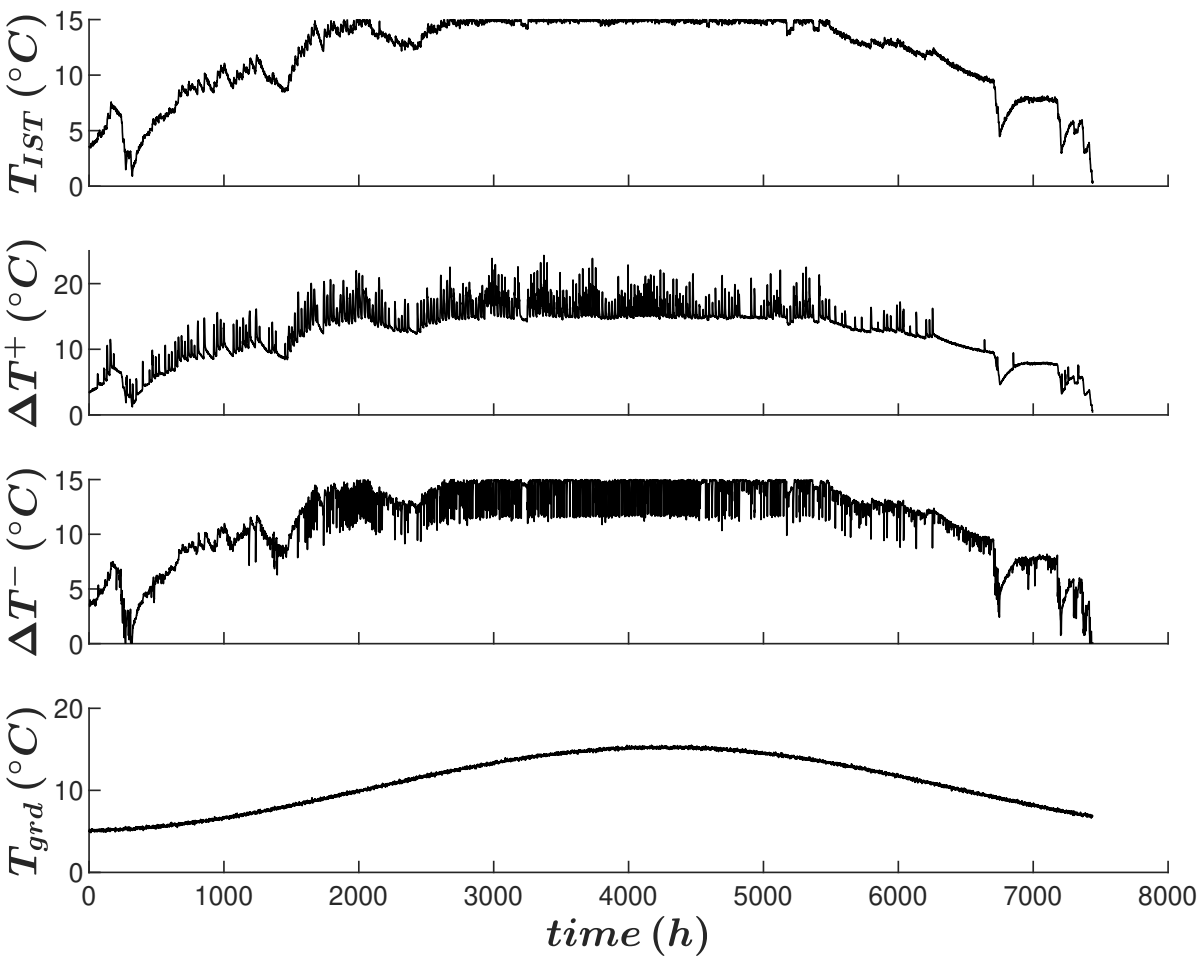

Figure 5.4: Time series used to estimate the parameters of the IST model.

is described by a second order polynomial, which relates the efficiency to the mean fluid temperature, ambient temperature and the incident solar radiation. Studies involving optimal control formulations for these collector types assume a constant efficiency [77, 78]. WISC are assigned to the category of unglazed collectors. According to the European Norm EN 12975 [79], the useful thermal power output $\dot{\boldsymbol{Q}}_{WISC,t}$ is computed using a linear model.

$$\begin{aligned}\frac{d\boldsymbol{T}_{WISC,avg,t}}{dt} = & -\frac{1}{n_{WISC}C_{WISC}}\dot{\boldsymbol{Q}}_{WISC,t} \\ & + \frac{A_{WISC}}{C_{WISC}}\eta_0 G''_t(1-p_u u_t) \\ & - \frac{A_{WISC}}{C_{WISC}}(p_1+p_2 u_t)(\boldsymbol{T}_{WISC,avg,t}-T_{a,t})\end{aligned} \tag{5.19}$$

Collector specific parameters are the aperture area A_{WISC}, the performance coefficients p_i, the efficiency η_0 and the thermal capacity C_{WISC}. A number n_{WISC} of WISC provides the useful thermal output power. The ambient temperature is reflected with $T_{a,t}$. The mean temperature $\boldsymbol{T}_{WISC,avg,t}$ is approximated by the arithmetic average of the in- and outlet temperatures $\boldsymbol{T}_{WISC,in}$ and $\boldsymbol{T}_{WISC,out}$ of WISC.

$$\boldsymbol{T}_{WISC,avg,t} = \frac{\boldsymbol{T}_{WISC,in,t}+\boldsymbol{T}_{WISC,out,t}}{2} \tag{5.20}$$

Table 5.3: Numerical parameter values for WISC

Parameter	Value	Units
n_{WISC}	4	–
A_{WISC}	2.34	m^2
C_{WISC}	10000	J/kg
ϵ/α	0.85	–
η_0	0.702	–
p_u	0.066	s/m
p_1	32.63	W/m^2K
p_2	3.59	Ws/m^3K
σ	$5.67 \cdot 10^{-8}$	W/m^2K^4

The net radiation G_t'' in Eq. (5.21) is composed of the radiation G_t' in the collector plane, the long-wave radiation $G_{lw,t}$, the ratio of hemispheric emissivity ϵ to solar absorbance α and the Stefan-Boltzmann constant σ.

$$G_t'' = G_t' + \left(\frac{\epsilon}{\alpha}\right)\left(G_{lw,t} - \sigma T_{a,t}^4\right) \tag{5.21}$$

The model presented in this chapter is used for the emulation of the solar collector as well as in the MPC formulation. For this reason, data-driven estimation techniques are redundant. The relevant parameters are chosen according to a Polysun data base for solar collectors [74]. The numerical values of the parameters are presented in Table 5.3.

5.4 Thermal Energy Storage Model

TES store heating and cooling energy and overcome the mismatch between thermal energy production and consumption. thermal energy storage systems are divided into three different categories [80]: (1) sensible heat storage, (2) latent heat storage and (3) thermochemical heat storage. Sensible storage systems are mainly used in building specific applications. Mainly cylindrical designs made of steel are deployed. To reduce thermal losses, thermal energy storage systems are jacketed with a low thermal conductivity insulation. In the case of space cooling TES, the insulation must also be diffusion-resistant. The test bench provides heat storage systems for space heating, space cooling and hot water. The space heating TES is a Viessmann Vitocell 100-E with a capacity of 2 m^3 of water. The space cooling TES is a ACF 500 with 0.5 m^3, whereas the domestic hot water TES is a Viessmann Vitocell 100-V with a capacity of 0.39 m^3 of water.

Different MPC formulations for thermal storage systems are proposed in the literature. A common approach is to consider the TES as a system with a single capacitance which has a homogeneously distributed internal energy [81, 11, 14]. However, these models do not consider vertical stratification which occurs due to temperature-related density differences of the water [75]. One-dimensional vertical stratification is investigated in studies presented by [82], [11] and [13]. Each layer is subject to convective and conductive heat

transfer mechanisms. Heat generators and space heating circuits are usually two-point controlled. This results in bilinear terms caused by the multiplication of mass flow and temperature. Bilinear formulations are usually circumvented with the big M formulation or a fixed point linearization.

This thesis pursues the single capacitance modeling approach, as it offers a good compromise between prediction accuracy and fast computation. Eq. (5.22) presents a generic approach to model a thermal energy storage by using the first law of thermodynamics:

$$\boldsymbol{T}_{i,t} = \left(\frac{1}{C_i R_i^{loss}} \left(T_{s,t} - \boldsymbol{T}_{i,t} \right) + \frac{1}{C_i} \dot{\boldsymbol{Q}}_{in,i,t} - \frac{1}{C_i} \dot{\boldsymbol{Q}}_{out,i,t} \right) dt + d\omega_{i,t}, \tag{5.22}$$

with R_i^{loss} the thermal resistance between the TES and the surrounding air at temperature $T_{s,t}$. C_i is the thermal capacitance and $\boldsymbol{T}_{i,t}$ the lumped temperature. $\dot{\boldsymbol{Q}}_{in,i,t}$ and $\dot{\boldsymbol{Q}}_{out,i,t}$ represent the thermal power injection and withdrawal. $\omega_{i,t}$ is a Wiener process with incremental covariance $\sigma_{1,i}^2$.

The temperatures in the storage systems are subject to further boundary conditions to guarantee thermal comfort. $T_{HC,t}$ and $T_{SC,t}$ are the heating and cooling curve temperatures. $T_{DHW,t}$ indicates the tapping temperatures of the domestic hot water. The hard constraints are softened using the slack variables $\boldsymbol{s}_{i,t}$ to guarantee feasibility beyond the limit temperatures $T_{SH,max}$, $T_{DHW,max}$ and $T_{SC,min}$.

$$T_{HC,t} \boldsymbol{sh}_t + T_{s,t} \left(1 - \boldsymbol{sh}_t \right) - \boldsymbol{s}_{SH,t} \leq \boldsymbol{T}_{SH,t} \leq T_{SH,max} + \boldsymbol{s}_{SH,t}, \tag{5.23}$$

$$T_{DHW,t} dhw_t + T_{s,t} \left(1 - dhw_t \right) - \boldsymbol{s}_{DHW,t} \leq \boldsymbol{T}_{DHW,t} \leq T_{DHW,max} + \boldsymbol{s}_{DHW,t}, \tag{5.24}$$

$$T_{SC,min} - \boldsymbol{s}_{SC,t} \leq \boldsymbol{T}_{SC,t} \leq \boldsymbol{sc}_t T_{SC} + T_{s,t} \left(1 - \boldsymbol{sc}_t \right) + \boldsymbol{s}_{SC,t}, \tag{5.25}$$

$$0 \leq \boldsymbol{s}_{i,t}, \tag{5.26}$$

The binary variables $\boldsymbol{sh}_t \in \{0,1\}$, $dhw_t \in \{0,1\}$ and $\boldsymbol{sc}_t \in \{0,1\}$ indicate whether heat is required at a given time step or not.

Parameter Estimation Thermal Energy Storage Models

The time series for the parameter estimation are generated by means of temperature measurements of the thermal storage systems. The measurement series for the domestic hot water and space cooling TES are recorded over a time window of 24 hours. The test cycle for the space heating TES is 48 hours due to its large volume. The results of the measurement series are shown in Figure 5.5, 5.6 and 5.7. The measured state variable is the TES temperature $\boldsymbol{T}_{i,t}$. The observation equation is written as follows:

$$Y_k = \boldsymbol{T}_{i,k} + e_{i,k}, \tag{5.27}$$

where $e_{i,k}$ is the measurement error with variance $\sigma_{2,i}^2$. The measured variable Y_k is the arithmetic mean of all temperature sensors attached to the corresponding TES. The parameter estimates are shown in Table 5.4.

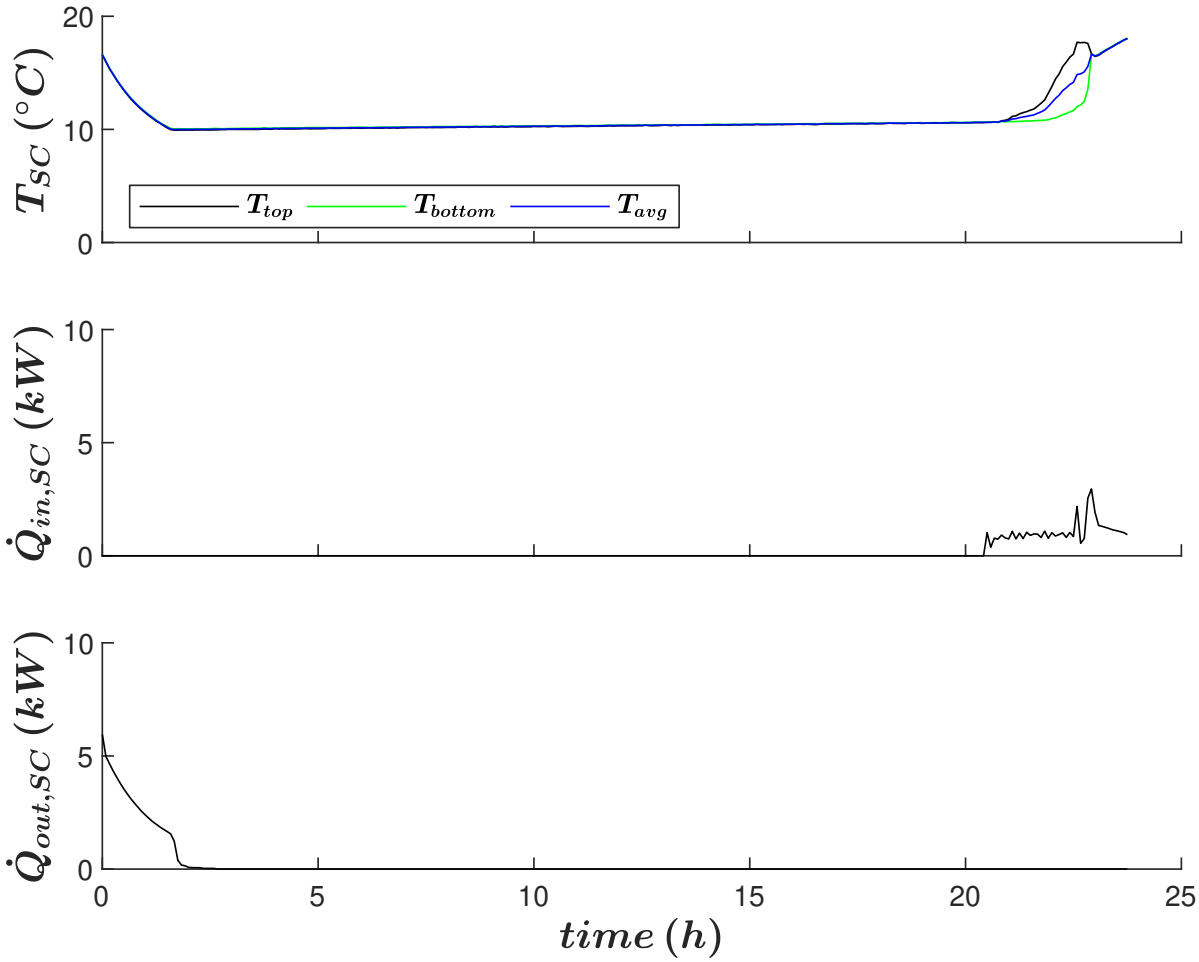

Figure 5.5: Time series used to estimate the SC TES parameters.

Table 5.4: Numerical parameter values for thermal energy storage systems.

Parameter	Value	Units
R_{SC}^{loss}	239.91	K/kW
R_{DHW}^{loss}	730.42	K/kW
R_{SH}^{loss}	131.39	K/kW
C_{SC}	0.63	kWh/K
C_{DHW}	0.46	kWh/K
C_{SH}	2.23	kWh/K
$\sigma_{1,SC}$	$2.48 \cdot 10^{-7}$	$°C$
$\sigma_{1,DHW}$	$1.06 \cdot 10^{-17}$	$°C$
$\sigma_{1,SH}$	0.09	$°C$
$\sigma_{2,SC}$	0.19	$°C$
$\sigma_{2,DHW}$	3.62	$°C$
$\sigma_{2,SH}$	$3.20 \cdot 10^{-12}$	$°C$

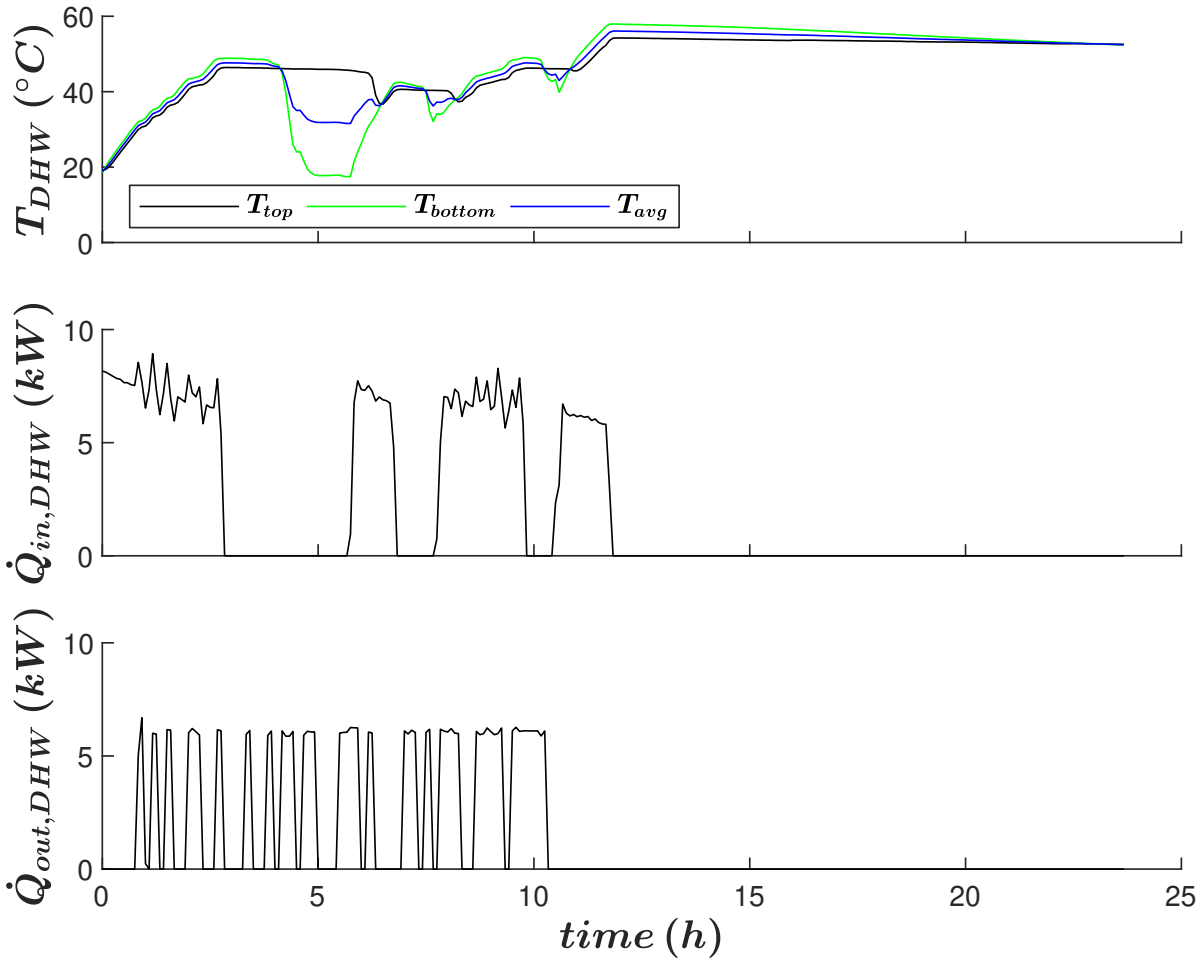

Figure 5.6: Time series used to estimate the DHW TES parameters.

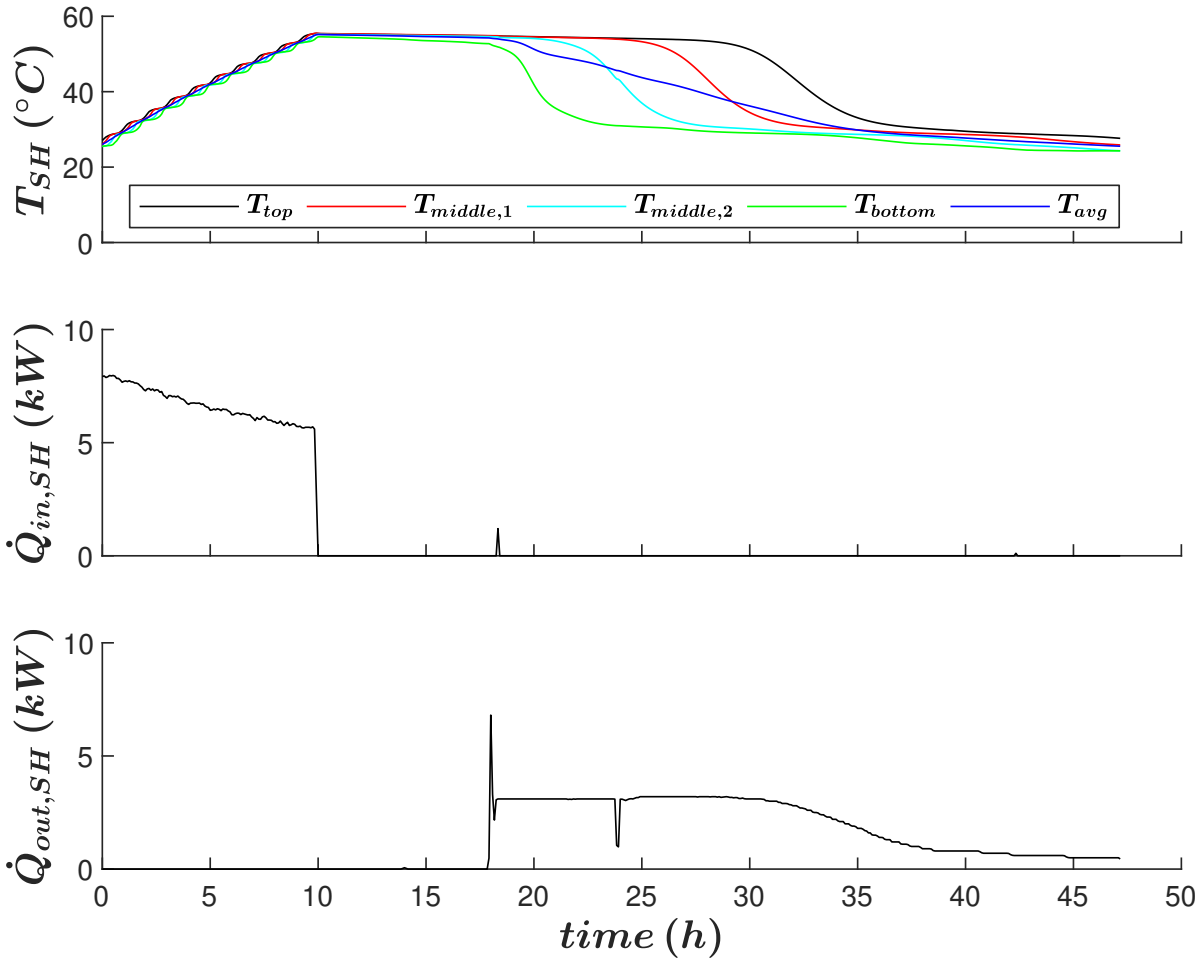

Figure 5.7: Time series used to estimate the SH TES parameters.

5.5 Battery Storage System Model

Batteries provide a possibility to store electricity in an electrochemical way. Usually electrochemical systems consist of electrodes and an electrolyte that conducts ions. Electrochemical battery storage systems are divided into two categories [43]: (1) low temperature batteries (lead, nickel and lithium) and (2) high temperature batteries (sodium-sulfur). In this work lead-gel batteries are used to store electricity, more precisely 24 Hoppecke VR L 2-520 connected in series with a nominal capacity of 470 Ah at C10.

Batteries can be illustrated with electrical equivalent circuit diagrams. The charging and discharging process of the battery is subject to certain losses due to the internal battery resistance and the inverter. According to Figure 5.8 the charging η_{ch} and discharging efficiency η_{dch} can be calculated as follows:

$$\eta_{ch} = \frac{\dot{P}_{in}}{\dot{P}_{ch}}, \tag{5.28}$$

$$\eta_{dch} = \frac{\dot{P}_{dch}}{\dot{P}_{out}}, \tag{5.29}$$

where $\dot{P}_{in}$ and $\dot{P}_{out}$ are the electrical power flows to and from the battery. P_{ch} and P_{dch} denote the power transferred to and from the electric grid. The state of charge of a BSS is usually determined by means of an energy balance approach [83, 11, 28, 14, 25]:

$$d\boldsymbol{SOC}_t = \left(\frac{\eta_{ch}}{C_{BSS}} \dot{\boldsymbol{P}}_{ch,t} + \frac{1}{C_{BSS}\eta_{dch}} \dot{\boldsymbol{P}}_{dch,t} \right) dt + d\omega_{BSS,t}, \tag{5.30}$$

with C_{BSS} the nominal capacity of the electrical energy storage and $\omega_{BSS,t}$ a Wiener process with incremental covariance $\sigma^2_{1,BSS}$. The state of charge $\boldsymbol{SOC}_t$ is constrained to lower and upper state of charge levels SOC_{min} and SOC_{max}. The slack variable $\boldsymbol{s}_{BSS,t}$ softens the hard constraint to guarantee feasibility during online operation:

$$SOC_{min} - \boldsymbol{s}_{BSS,t} \leq \boldsymbol{SOC}_t \leq SOC_{max} + \boldsymbol{s}_{BSS,t}, \tag{5.31}$$

$$0 \leq \boldsymbol{s}_{BSS,t}. \tag{5.32}$$

In addition, the charging and discharging power of the battery storage system should not exceed the maximum battery charging $\dot{P}_{ch,max}$ and discharging power $\dot{P}_{dch,max}$. In the literature, fixed values are often assumed for $\dot{P}_{ch,max}$ and $\dot{P}_{dch,max}$ [83, 26, 28, 14, 24, 25]. However, this is a oversimplification of reality, as lead-based batteries are usually charged using the IUoU method [84]. The IUoU method is a charging procedure which consists of three phases: (1) I-phase (constant electric current), (2) Uo-phase (constant over-voltage) and (3) U-phase (constant voltage). During the Uo-phase the battery is charged at constant overvoltage, while the charging current is constantly decreasing. This means that the maximum charge power decreases as shown in Figure 5.9. The main purpose of the IUoU charging procedure is to fully charge the battery and simultaneously guarantee an increased lifespan.

This thesis proposes a data-driven approach where the values of $\dot{\boldsymbol{P}}_{ch,t}$, $\dot{\boldsymbol{P}}_{dch,t}$ and $\boldsymbol{SOC}_t$ are represented as a linear combination of the corresponding sampling points $\dot{P}_{ch,i}$, $\dot{P}_{dch,i}$ and SOC_i. A positive variable $\boldsymbol{\theta}_i \in \{0, 1\}$ is associated with each sampling point i to enable a linear combination between points. The BSS charging and discharging dynamics are linearly characterised as follows:

$$\dot{\boldsymbol{P}}_{ch,t} = \sum_i \boldsymbol{\theta}_{i,t} \dot{P}_{ch,i}, \tag{5.33}$$

$$\dot{\boldsymbol{P}}_{dch,t} = \sum_i \boldsymbol{\theta}_{i,t} \dot{P}_{dch,i}, \tag{5.34}$$

$$\boldsymbol{SOC}_t = \sum_i \boldsymbol{\theta}_{i,t} SOC_i, \tag{5.35}$$

$$1 = \sum_i \boldsymbol{\theta}_{i,t}, 0 \leq \boldsymbol{\theta}_{i,t}. \tag{5.36}$$

Simultaneous charging and discharging of the battery is not possible. This condition is mathematically expressed, using the big M method. To do so, two penalty constants M_{ch} and M_{dch} are used:

$$\dot{\boldsymbol{P}}_{ch,t} - M_{ch}\boldsymbol{ch}_t \leq 0, \tag{5.37}$$

$$\dot{\boldsymbol{P}}_{dch,t} - M_{dch}\boldsymbol{dch}_t \leq 0, \tag{5.38}$$

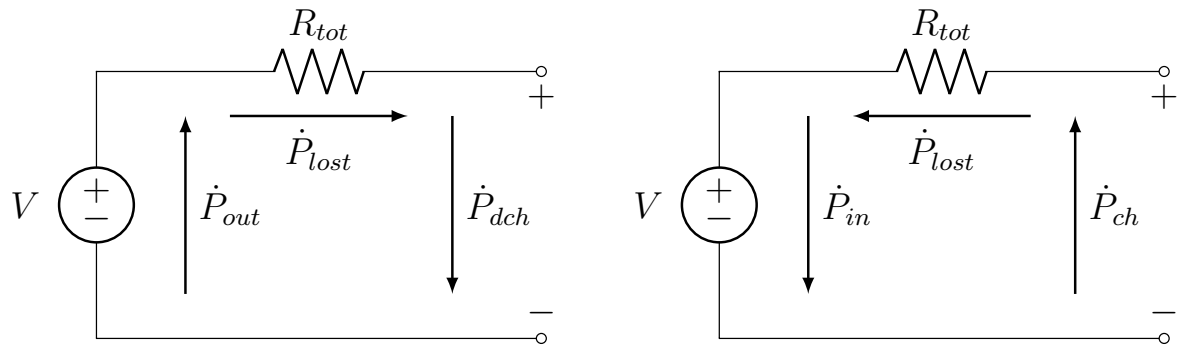

Figure 5.8: Battery equivalent circuit for discharging and charging cycle.

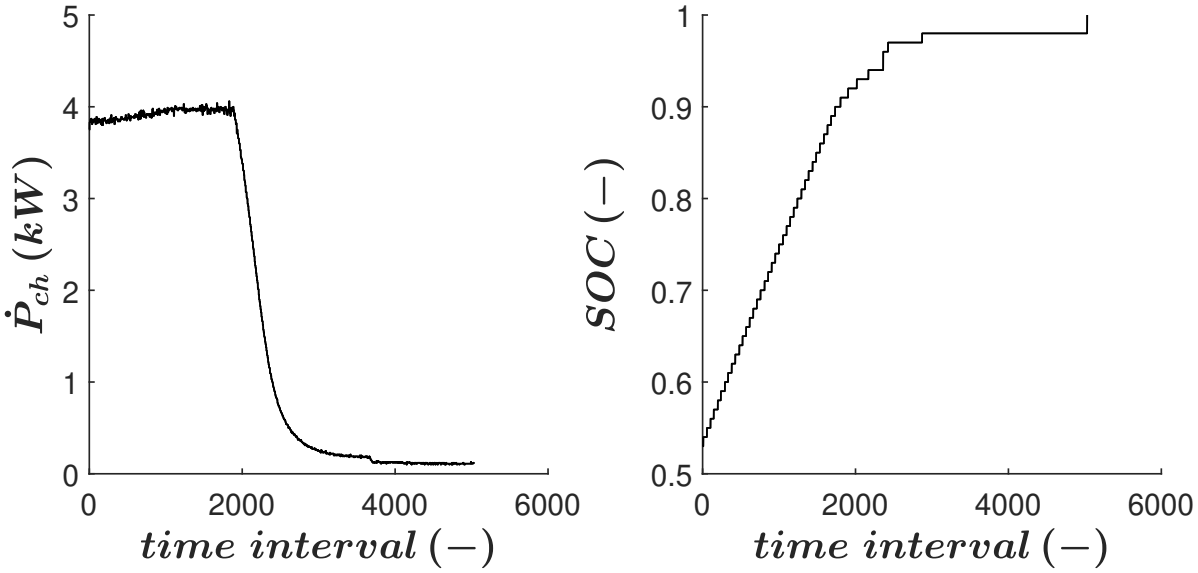

Figure 5.9: Charging cycle of Hoppecke VR L 2-520 lead-gel batteries using a Sunny Island 6.0

.

$$\boldsymbol{ch}_t + \boldsymbol{dch}_t \leq 1, \tag{5.39}$$

with $\boldsymbol{ch}_t \in \{0,1\}$ and $\boldsymbol{dch}_t \in \{0,1\}$ binary variables indicating whether the BSS is charged or discharged.

Parameter Estimation Battery Storage System Model

The time series for the parameter estimation are generated by means of state of charge measurements of the battery over a time window of seven hours. The results of the measurement series are shown in Figure 5.10. The measured state variable is the state of charge $\boldsymbol{SOC}_k$, which is calculated and communicated by the battery inverter. The observation equation is written as follows:

$$Y_k = \boldsymbol{SOC}_k + e_{BSS,k}, \tag{5.40}$$

where $e_{BSS,k}$ is the measurement error with variance $\sigma^2_{2,BSS}$. The parameter estimates are shown in Table 5.5.

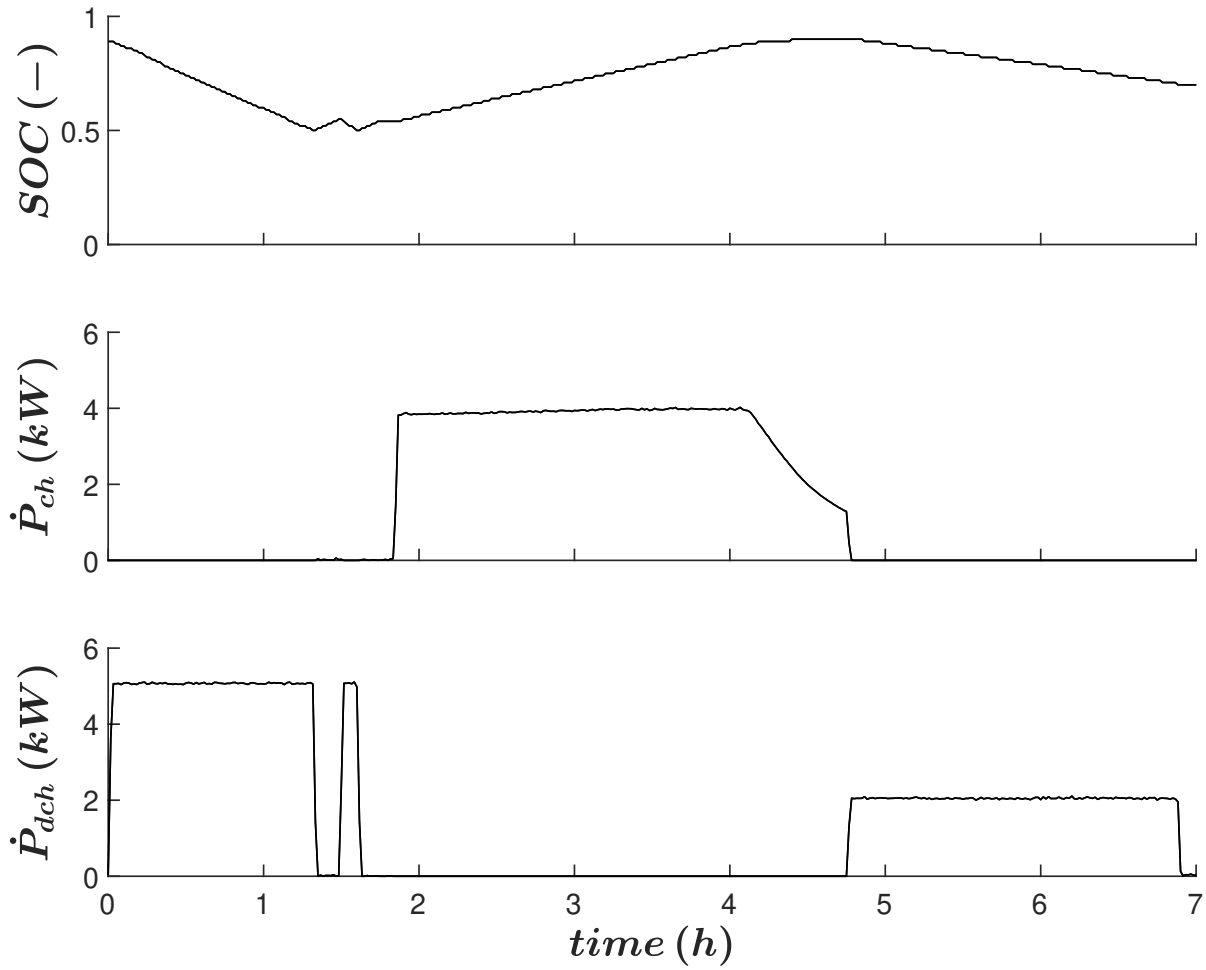

Figure 5.10: Time series used to estimate the BSS parameters.

Table 5.5: Numerical parameter values for thermal energy storage systems.

Parameter	Value	Units
C_{BSS}	21.62	kWh
η_{ch}	0.78	–
η_{dch}	0.82	–
$\sigma_{1,BSS}$	$1.97 \cdot 10^{-2}$	–
$\sigma_{2,BSS}$	$5.67 \cdot 10^{-6}$	–

5.6 Building Model

Buildings have a thermal mass that can be used for demand side management strategies. The main challenge is to accurately predict the thermal behaviour of the building to guarantee comfort of its occupants and technical limitations of HVAC equipment. Different approaches can be used to create an adequate building model for MPC. These can be categorized into white box, grey box and black box models [3]. In this context, [85]

investigates demand response strategies for a multi-purpose building using the building simulation tool Energy Plus. However, comparable approaches require a lot of physical information about the building structure, which are usually not available, as the plan data differ from the actually used materials during construction [3]. More black box oriented models are developed by measuring the requisite inputs and outputs of the system. Linear or non-linear mathematical functions are used to approximate the dynamics of the building. [86] investigates a predictive control strategy based on neural networks to optimally operate a boiler. The neural network is used to assess the time it takes to condition the building. This approach does not use a closed-loop optimisation scheme. [87] apply model-assisted batch reinforcement learning to determine the optimal control policy of a building subject to dynamic pricing. The disadvantage of the two prior mentioned studies is that most parameters do not have physical meaning. Therefore, they are not interpretable for building operators. In this work, grey box models are used, since they are able to accurately capture the system dynamics on the one hand and allow assessments of the thermal properties of the building on the other hand [88, 89, 90].

The main challenge of the greybox approach is to find a model that is neither under- or overfitting. A common approach is to select a suitable model from a set of models of increasing complexity. The underlying building structure is represented using resistive capacitive (RC) thermal networks. This thesis applies a statistical model selection procedure, which starts with the simplest model and iteratively extends complexity. The following steps must be considered [91]:

- Estimate the numerical values of the model parameters using the maximum likelihood estimation method.
- Use a likelihood ratio test to determine whether a larger model performs better than a sub-model. p values below 5% indicate whether the likelihood of a model extension is significantly higher than that of the sub model. The model selection procedure stops if none of the tests has a p value below 5%, otherwise the model extension with the lowest p-value is selected.
- Evaluate the selected model by checking for white noise characteristics of the residuals using the auto correlation function (ACF). Plotting the inputs, outputs and residuals provides information about which dynamics are not accurately captured by the model.

The set of deterministic model variations are illustrated in Figure 5.11 - 5.16. Applying the prior mentioned model selection procedure leads to the final $T_iT_hT_mp$ model illustrated in Figure 5.16:

$$\begin{aligned} d\boldsymbol{T}_i = \Bigg(&\frac{1}{C_iR_{im}}\left(\boldsymbol{T}_m - \boldsymbol{T}_i\right) + \frac{1}{C_iR_{ih}}\left(\boldsymbol{T}_h - \boldsymbol{T}_i\right) \\ &+ \frac{1}{C_iR_{ia}}\left(T_a - \boldsymbol{T}_i\right) + \frac{1}{C_i} p g_A G_h \Bigg) dt + d\omega_i, \end{aligned} \tag{5.41}$$

$$d\boldsymbol{T}_h = \left(\frac{1}{C_hR_{ih}}\left(\boldsymbol{T}_i - \boldsymbol{T}_h\right) + \frac{1}{C_h}\boldsymbol{\Phi}_h \right) dt + d\omega_h, \tag{5.42}$$

$$d\boldsymbol{T}_m = \left(\frac{1}{C_mR_{im}}\left(\boldsymbol{T}_i - \boldsymbol{T}_m\right) + \frac{1}{C_m}(1-p) g_A G_h \right) dt + d\omega_m. \tag{5.43}$$

The state variables are $\boldsymbol{T}_i$, $\boldsymbol{T}_h$ and $\boldsymbol{T}_m$. The measured state variable $\boldsymbol{T}_i$ designates the room temperature. The hidden states $\boldsymbol{T}_h$ and $\boldsymbol{T}_m$ represent the temperature of the heating system and walls or furniture respectively. The heating system injects the thermal power $\boldsymbol{\Phi}_h$ into the network. Each node has a thermal capacitance, which is indicated by C. Thermal resistances R connect neighboring nodes or a node with the ambient air at temperature T_a. The solar radiation G_h permeates through the windows into the building and is distributed proportionally to the respective nodes according to p. The windows are characterised by g_A, which indicates the solar heat gain coefficient multiplied by the window surface. $\omega_{i,t}$, $\omega_{h,t}$ and $\omega_{m,t}$ are Wiener processes with incremental covariance $\sigma^2_{1,i}$, $\sigma^2_{1,i}$ and $\sigma^2_{1,i}$.

The room temperature $\boldsymbol{T}_i$ is subject to further boundary conditions to guarantee thermal comfort. $T_{i,min}$ and $T_{i,max}$ indicate the minimum and maximum temperature treshold of the room. Hard constraints are softened using the slack variables $\boldsymbol{s}_{i,t}$ to guarantee feasibility:

$$T_{i,min} - \boldsymbol{s}_{i,t} \leq \boldsymbol{T}_{i,t} \leq T_{i,max} + \boldsymbol{s}_{i,t}, \tag{5.44}$$

$$0 \leq \boldsymbol{s}_{i,t}. \tag{5.45}$$

The heating system is subject to minimum and maximum heating capacity limits $\Phi_{h,min}$ and $\Phi_{h,max}$. $\Delta\Phi_{h,min}$ and $\Delta\Phi_{h,max}$ are used to express rate-of-movement constraints:

$$\Phi_{h,min} \leq \boldsymbol{\Phi}_h \leq \Phi_{h,max}, \tag{5.46}$$

$$\Delta\Phi_{h,min} \leq \Delta\boldsymbol{\Phi}_h \leq \Delta\Phi_{h,max}. \tag{5.47}$$

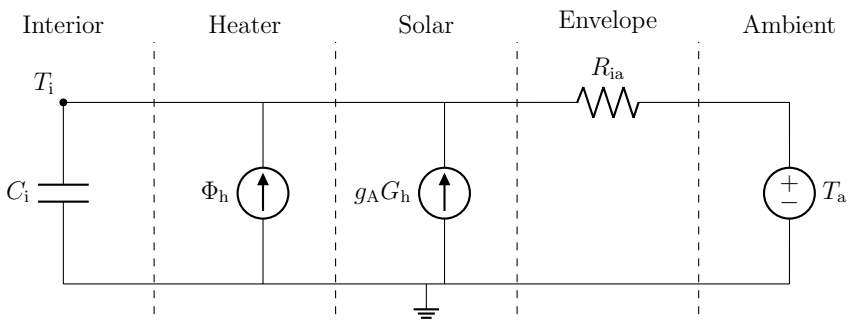

Figure 5.11: RC-network of the T_i model.

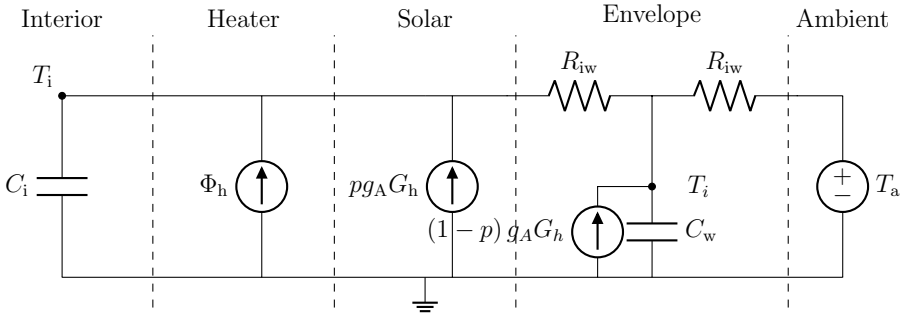

Figure 5.12: RC-network of the T_iT_wp model.

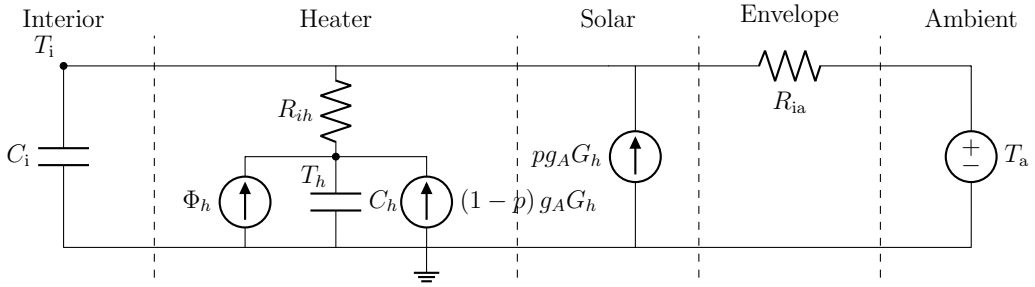

Figure 5.13: RC-network of the T_iT_hp model.

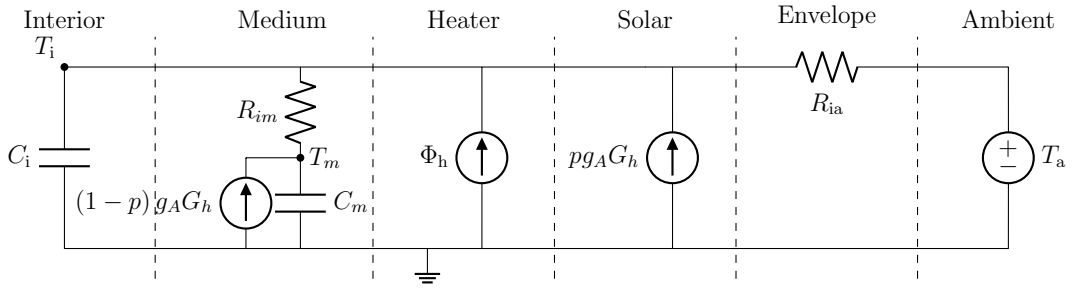

Figure 5.14: RC-network of the T_iT_mp model.

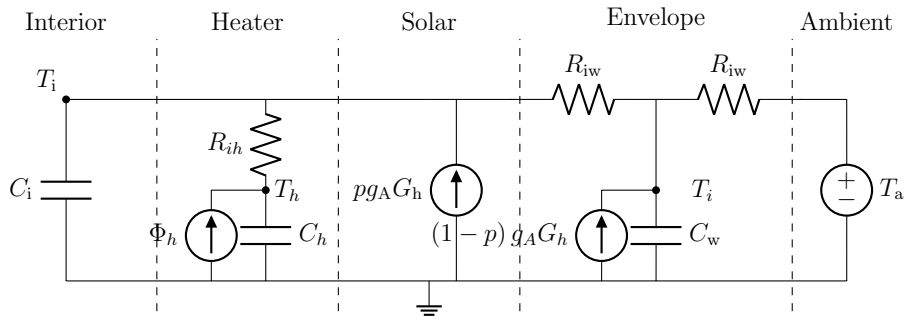

Figure 5.15: RC-network of the $T_i T_h T_w p$ model.

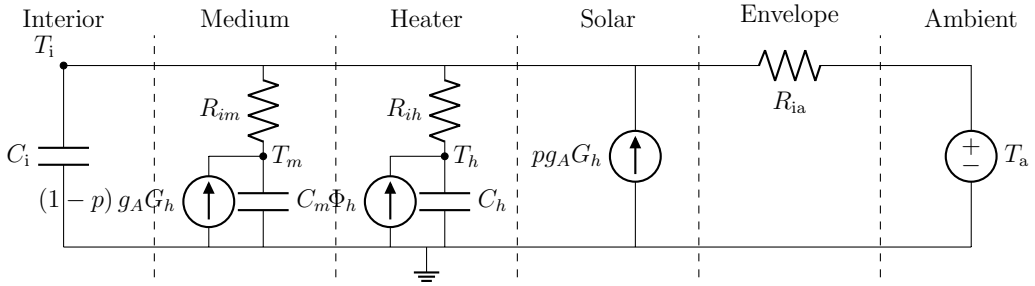

Figure 5.16: RC-network of the $T_i T_h T_m p$ model.

Parameter Estimation Building Model

The time series used to estimate the parameters is generated using TRNSYS. The building envelope is designed using TRNBuild and then imported into TRNSYS. The building has one thermal zone and a heated living area of 175 m^2 & volume of 481.25 m^3. The heat transmission coefficients of the building envelope are shown in Table 5.6. The heat

Table 5.6: U-values of the building envelope.

Component	U	Units
Floor	0.12	W/m^2K
External Wall	0.11	W/m^2K
Window	0.62	W/m^2K
Roof	0.12	W/m^2K

load is determined according to the European norm EN 12831 and corresponds to 3.5 kW at an outdoor temperature of -12°C [92]. The building has a ventilation system with a heat recovery efficiency of 85%. The air exchange rate of the room is 0.5 h^{-1}.

The considered time period of the building simulation is 513 hours. The results are illustrated in Figure 5.17 and show the temporal variation of the room temperature as a function of various inputs and disturbances. The on/off status of the heating system

corresponds to a pseudo random binary sequence (PRBS), which is a deterministic signal with white-noise properties [93]. The heating system is operated during short and long periods of time in order to be able to record the dynamics of the components with small and large time constants more precisely. The measured state variable is the room temperature $\boldsymbol{T}_{i,t}$. The observation equation is written as follows:

$$Y_k = \boldsymbol{T}_{i,k} + e_{i,k}, \tag{5.48}$$

where $e_{i,k}$ is the measurement error with variance $\sigma^2_{2,i}$. The results of the parameter estimation are shown in Table 5.7. Further investigations of the auto-correlation in Figure 5.18 indicates white noise characteristics of the one step prediction error for the $T_iT_hT_mp$ model. The two blue lines mark the 95 % confidence band. An analysis of the time series in Figure 5.19 indicates smaller deflections of the $T_iT_hT_mp$ residuals in comparison to the T_i . Superimposing the residuals, inputs and disturbances shows that the $T_iT_hT_mp$ model covers all important building dynamics.

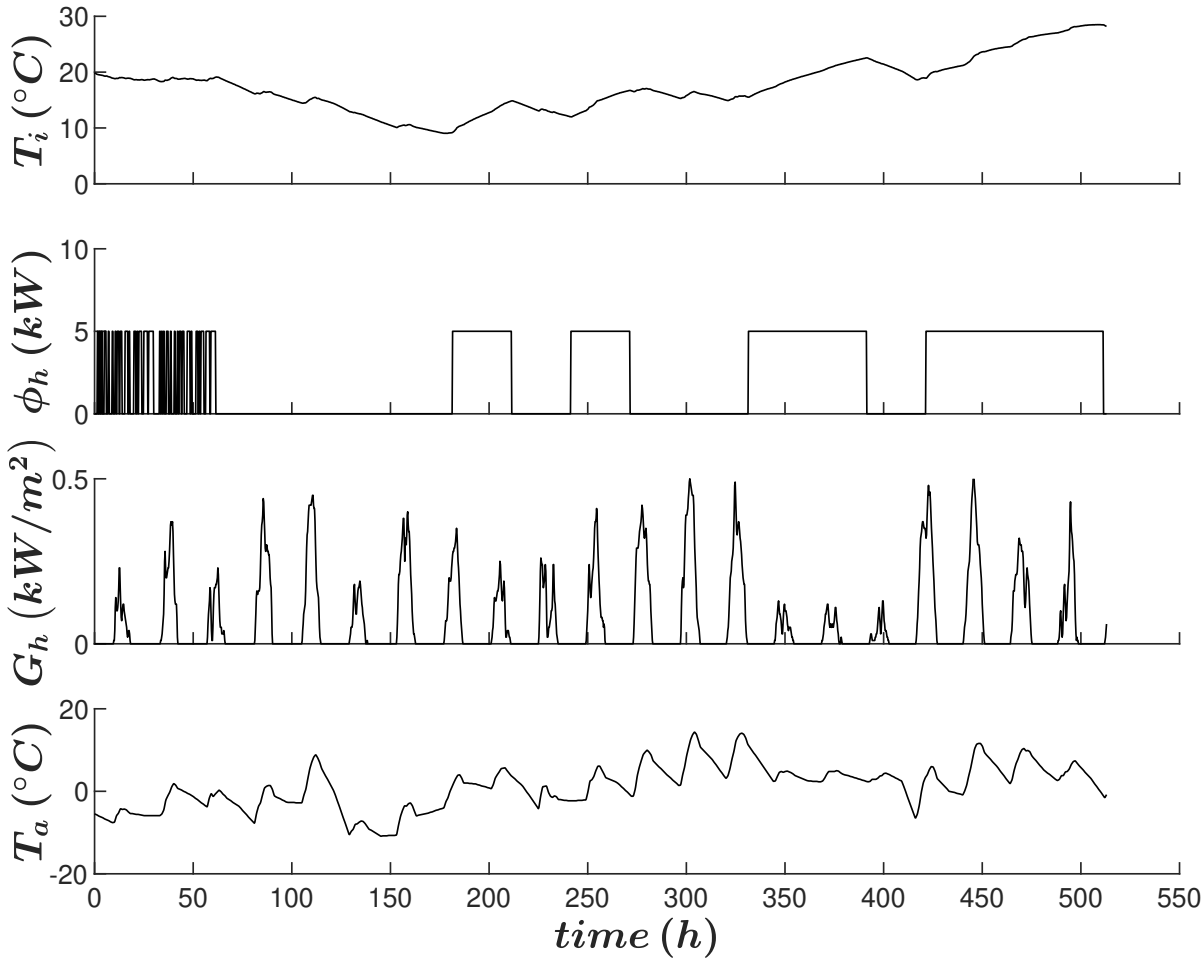

Figure 5.17: Graph illustrating the time series of the room temperature, heating power, global horizontal radiation and ambient temperature.

Table 5.7: Numerical parameter values for the building.

Parameter	Value	Units
C_i	0.51	kWh/K
C_h	17.64	kWh/K
C_m	5.69	kWh/K
R_{ia}	5.52	K/kW
R_{ih}	0.34	K/kW
R_{im}	2.65	K/kW
g_A	8.12	m^2
p	0.32	$-$
$\sigma_{1,i}$	$9.54 \cdot 10^{-7}$	$^\circ C$
$\sigma_{1,h}$	$4.17 \cdot 10^{-5}$	$^\circ C$
$\sigma_{1,m}$	$0.25 \cdot 10^{-5}$	$^\circ C$
$\sigma_{2,i}$	$1.05 \cdot 10^{-4}$	$^\circ C$

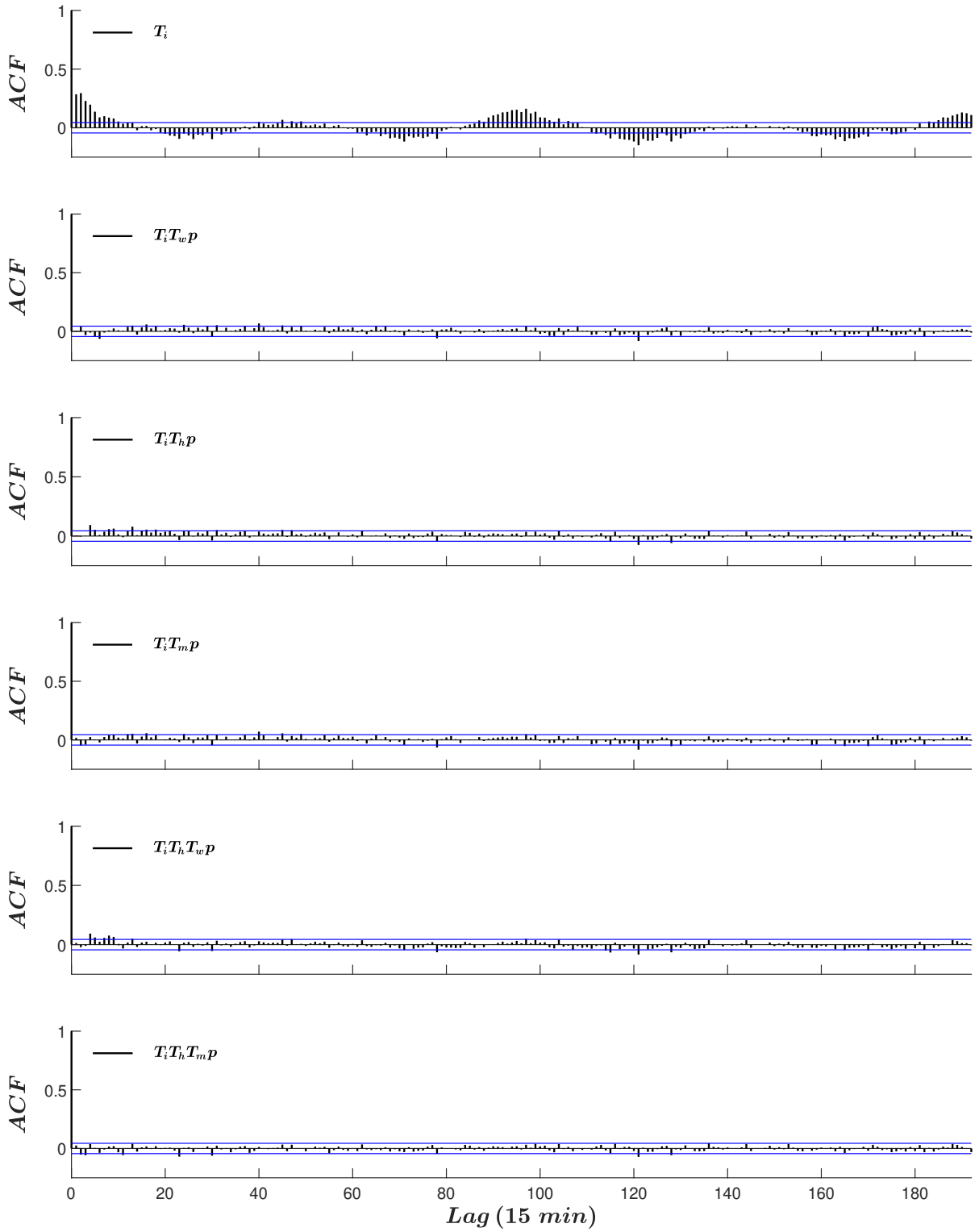

Figure 5.18: The auto-correlation of the residuals for the T_i, T_iT_wp, T_iT_hp, T_iT_mp, $T_iT_hT_wp$, and $T_iT_hT_mp$ model.

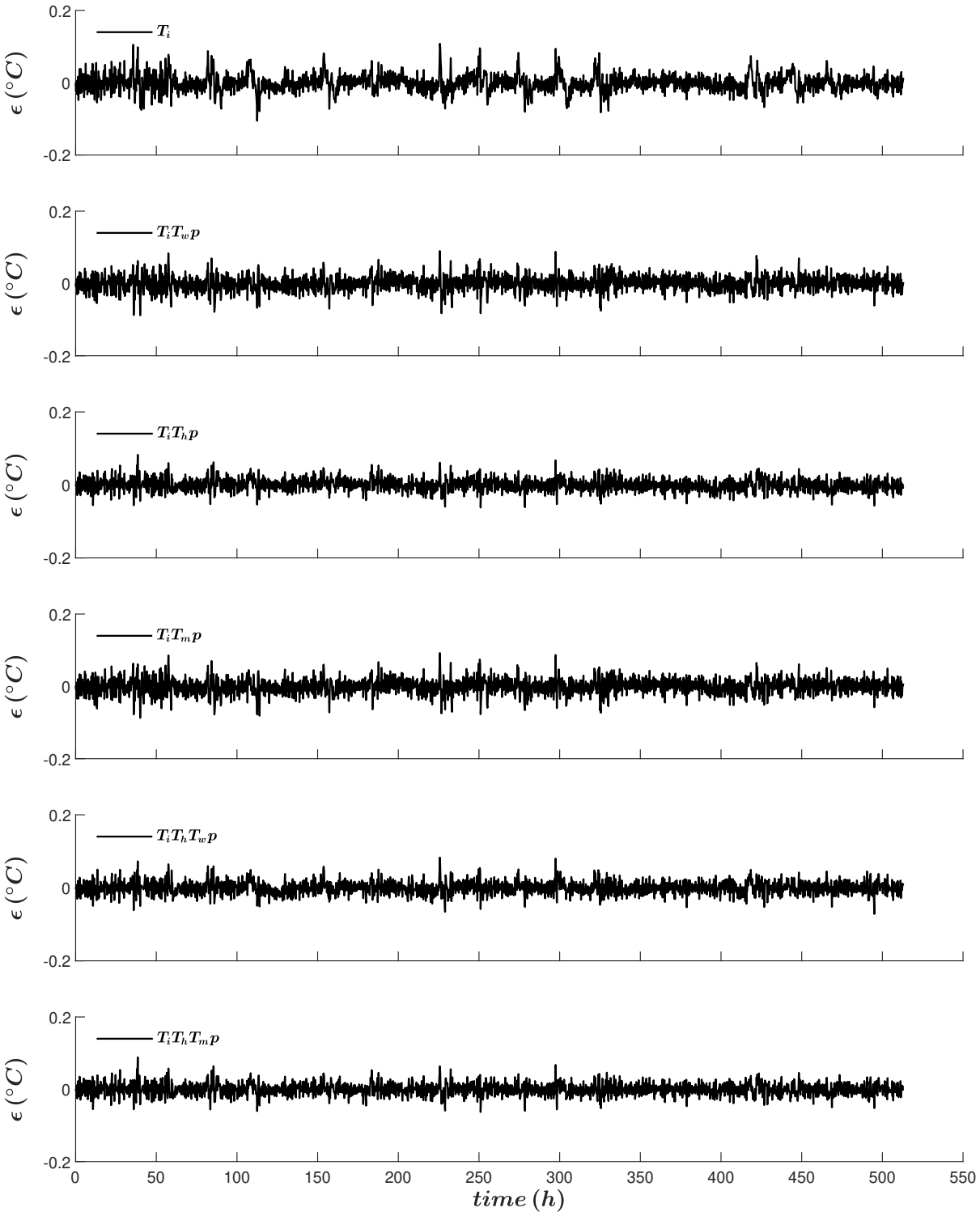

Figure 5.19: The one-step prediction error of the residuals for the T_i, T_iT_wp, T_iT_hp, T_iT_mp, $T_iT_hT_wp$, and $T_iT_hT_mp$ model.

Chapter 6

Electrical Power Balance and Objective Function

This chapter illustrates the mathematical formulation of the electrical power balance and objective function. The electrical power balance is established to ensure that the sum of power generated by the distributed energy resources and the main grid matches the load. The power balance at a given time step is represented with the following equation:

$$\dot{\boldsymbol{P}}_{buy,t} + \dot{\boldsymbol{P}}_{dch,t} + \dot{P}_{pv,t} = \dot{\boldsymbol{P}}_{sell,t} + \dot{\boldsymbol{P}}_{ch,t} + \dot{\boldsymbol{P}}_{dshp,t} + \dot{P}_{slp,t} \tag{6.1}$$

with $\dot{\boldsymbol{P}}_{buy,t}$ and $\dot{\boldsymbol{P}}_{sell,t}$ are respectively the electrical power bought from the main grid or sold to the main grid. $\dot{P}_{pv,t}$ represents the electrical power provided by photovoltaic panels (PV), whereas $\dot{P}_{slp,t}$ describes the electrical power requested by the consumers. It is not possible to buy/sell electricity from/to the main grid simultaneously. This condition is mathematically expressed, using the big M method. To do so, two penalty constants M_{buy} and M_{sell} are used:

$$\dot{\boldsymbol{P}}_{buy,t} - M_{buy}\boldsymbol{buy}_t \leq 0 \tag{6.2}$$

$$\dot{\boldsymbol{P}}_{sell,t} - M_{sell}\boldsymbol{sell}_t \leq 0 \tag{6.3}$$

$$\boldsymbol{buy}_t + \boldsymbol{sell}_t \leq 1 \tag{6.4}$$

$$0 \leq \dot{\boldsymbol{P}}_{buy,t} \leq \dot{P}_{buy,max} \tag{6.5}$$

$$0 \leq \dot{\boldsymbol{P}}_{sell,t} \leq \dot{P}_{sell,max} \tag{6.6}$$

with $\boldsymbol{buy}_t$ and $\boldsymbol{sell}_t$ binary variables indicating whether electricity is bought or sold to the main grid. The electrical power constraints are expressed by means of $\dot{P}_{buy,max}$ and $\dot{P}_{sell,max}$.

The objective of the MPC problem is to minimise the total cost of the energy system over a certain scheduling horizon. The costs arise from electricity import/export from the public power grid and violating hard constraints. The objective function is given in Eq. (6.7), where $c_{elec,t}$ is the price for electricity import/export, ρ_t the cost penalty and $\boldsymbol{s}_t$ the slack variable at a given time step.

$$\begin{aligned} Min \sum_t \Big(& c_{elec,t}\dot{\boldsymbol{P}}_{buy,t} - c_{elec,t}\dot{\boldsymbol{P}}_{sell,t} + \rho_{SH,t}\boldsymbol{s}_{SH,t} + \rho_{DHW,t}\boldsymbol{s}_{DHW,t} \\ & + \rho_{SC,t}\boldsymbol{s}_{SC,t} + \rho_{BSS,t}\boldsymbol{s}_{BSS,t} + \rho_{i,t}\boldsymbol{s}_{i,t} \Big). \end{aligned} \tag{6.7}$$

Chapter 7

Model Predictive Controller Design

This chapter deals with the design aspect of the predictive controller, which is used in a laboratory setting. In this context, the exogenous inputs are first discussed in more detail. The chapter concludes with the integration of exogenous inputs into the controller structure.

7.1 Exogenous Inputs

The control problem in this thesis requires predictions of exogenous variables. It is apparent from Chapter 5 that the prediction of the following data is relevant to the model predictive controller. This thesis assumes perfect forecasts for the following inputs:

- Weather data containing radiation-, temperature and wind readings
- Electricity production of photovoltaic (PV) panels
- Profiles describing electricity consumption, domestic hot water consumption, and the presence of residents
- Electricity price data

This thesis assumes perfect forecast scenarios.

Weather Data

Luxembourg's Agricultural Weather Service operates automated weather stations that are distributed throughout the country. The weather data can be viewed online from 2010 onwards and provide information on outdoor temperature, global horizontal radiation and wind speed, among other things with a time resolution of one hour [94]. Missing data are supplemented with the arithmetic mean of the measured values from the previous and following day. Time series with a resolution of less than one hour are generated with a piecewise cubic Hermite interpolating polynomial. Figure 7.1 shows the annual variation of the outdoor temperature T_a and global radiation G_h. The annual average temperature is 9.96 °C and the annual yield of global radiation is 1135.4 kWh/m^{2}a.

To capture the phase transition process within the ice storage, the scheduling horizon

should ideally be equal to one year. However, a MILP-Model of such dimension is impossible to solve within a reasonable time frame. To reduce the computational effort, the typical day approach is adopted [95]. For this purpose the year is divided into a winter, spring, summer and autumn season. The medoid is determined for each season using a k-medoid clustering approach in Matlab. A medoid day is defined as the day of a season whose average dissimilarity to all days in the season is minimal. The city block metric is used to quantify the distance between the medoid and its cluster members. The typical day for each season is shown in Figure 7.2.

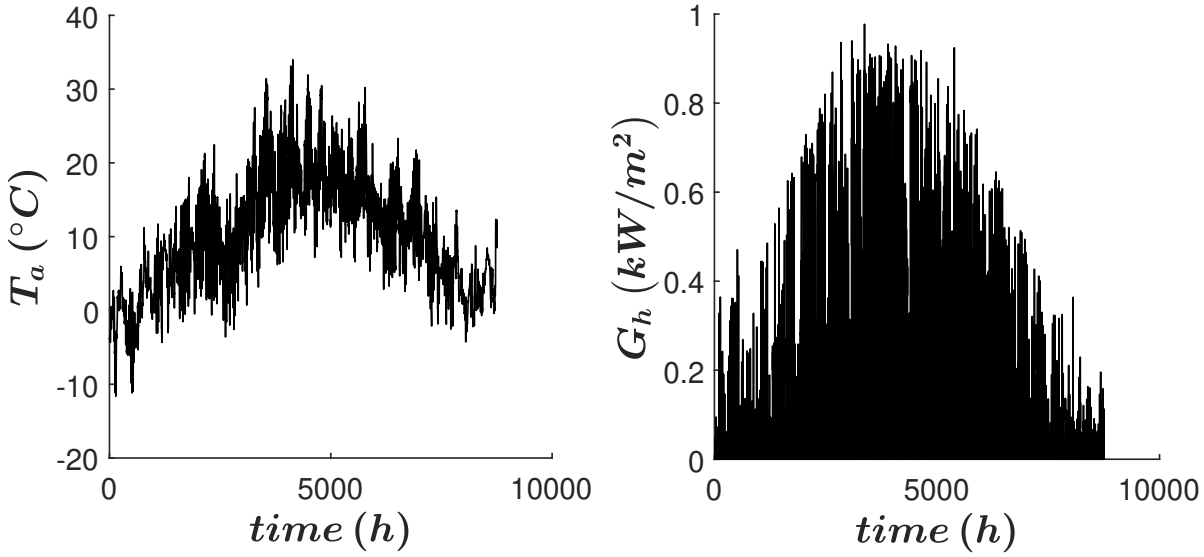

Figure 7.1: Annual time series of outdoor temperature and global radiation.

Photovoltaic Electrical Power Production

Forecasting the power production of PV panels is a constantly evolving field of research. In general, PV forecasting methods can be divided into three major categories [96]: (1) time-series statistical methods, (2) physical methods and (3) ensemble methods. In the context of this work the PV panels are emulated with the help of a direct current power supply. It is assumed that 15 PV modules are distributed on 2 strings each. The monocrystalline PV panel is a Premium incell L mono black 250 by Solar-Fabrik AG, whose maximum power point (MPP), open ciruit (OC) and short circuit (SC) characteristics are summarized in Table 7.1 for standard testing conditions (STC). The U-I curve of the PV generator is calculated using a physical approach according to [97]. Forecasted PV power production profiles assume the operating mode at the MPP. The module temperature is calculated according to [75].

Occupancy Behavior

The energy-related profiles are based on a real building construction in Luxembourg, whose energy consumption is shown on a scale of 1:125 in Table 7.2. The space heating demand depends mainly on the physical properties of the building. However, the thermal behaviour of the building is also influenced by its occupants. This is due to internal loads

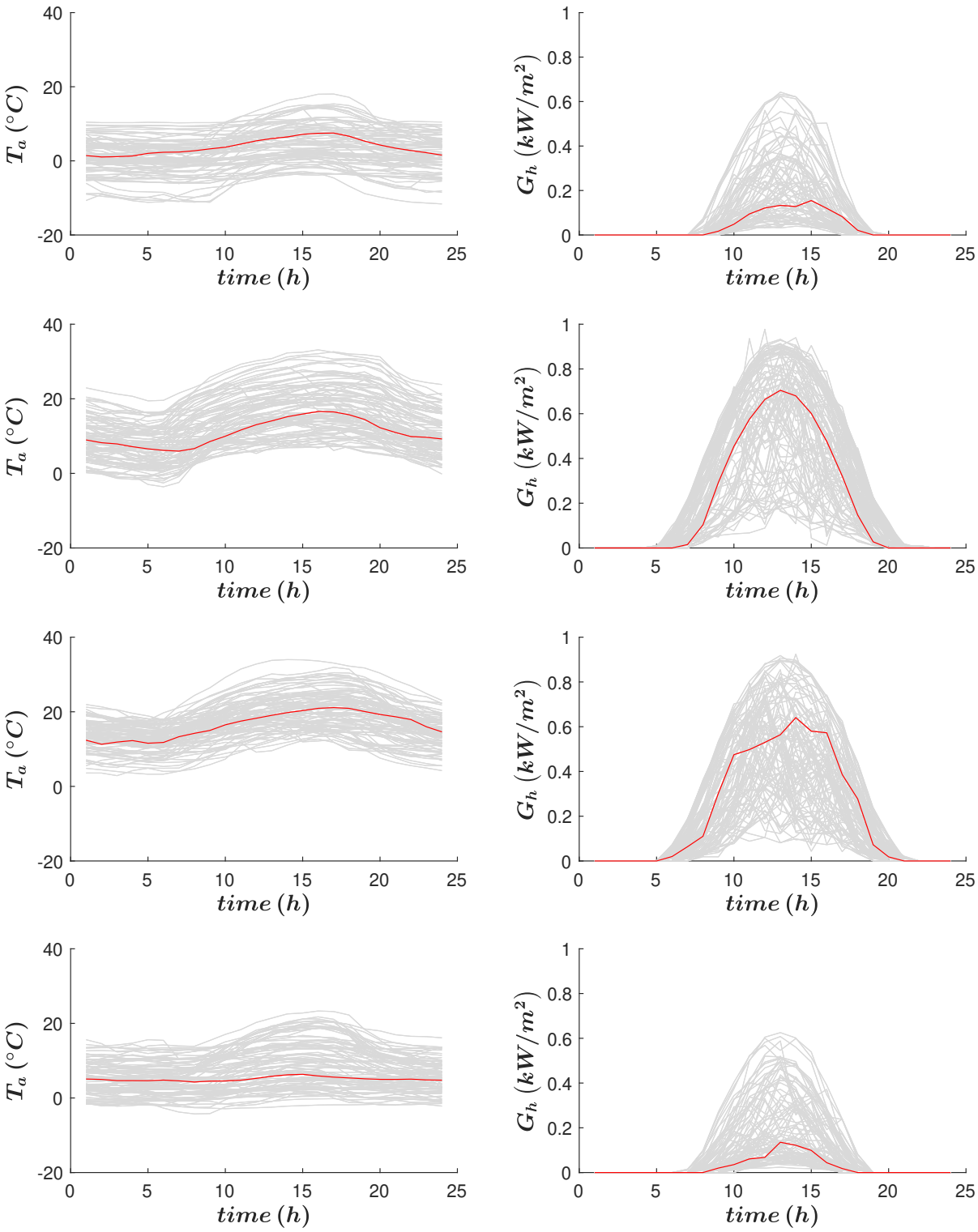

Figure 7.2: Red line plot indicating the medoid for the winter, spring, summer and autumn period from top to bottom.

$\dot{Q}_L$ caused by electrical equipment and person-related heat gains. Heat gains caused by one inhabitant are divided into a convective and radiative part which correspond to 20 W and 60 W respectively [98]. In this thesis, a residential building is considered,

Table 7.1: Electrical parameters of a PV panel at standard testing conditions.

Parameter	Value	Units
$\dot{P}_{MPP}$	0.25	kW
U_{MPP}	30	V
U_{OC}	37.8	V
I_{MPP}	8.2	A
I_{SC}	9.75	A

Table 7.2: Annual energy demands.

Energy	Value	Units
Space Heating	5900.00	kWh/an
Domestic Hot Water	4255.90	kWh/an
Electricity	6647.20	kWh/an

whose occupation profile is described by a factor changing every hour. The profile is assumed to be identical for every day and reflects a four-person household. Synthetic electrical load profiles (SLP) describe the electricity consumption $\dot{P}_{SLP}$ of the building. Standard load profiles are provided by the grid operators for different consumer groups and are normalised to an annual electrical energy demand of 1000 kWh/an [99]. This thesis assumes a SLP for households (H0) which is extrapolated to an annual electrical energy demand of 6647.20 kWh/an. The diurnal demand of DHW $\dot{Q}_{DHW}$ is described with tapping profiles according to DIN EN 16147 [100]. Tapping profile L is chosen with a daily energy demand of 11.66 kWh/d. Figure 7.3 shows the occupancy, internal loads, DHW and SLP profiles.

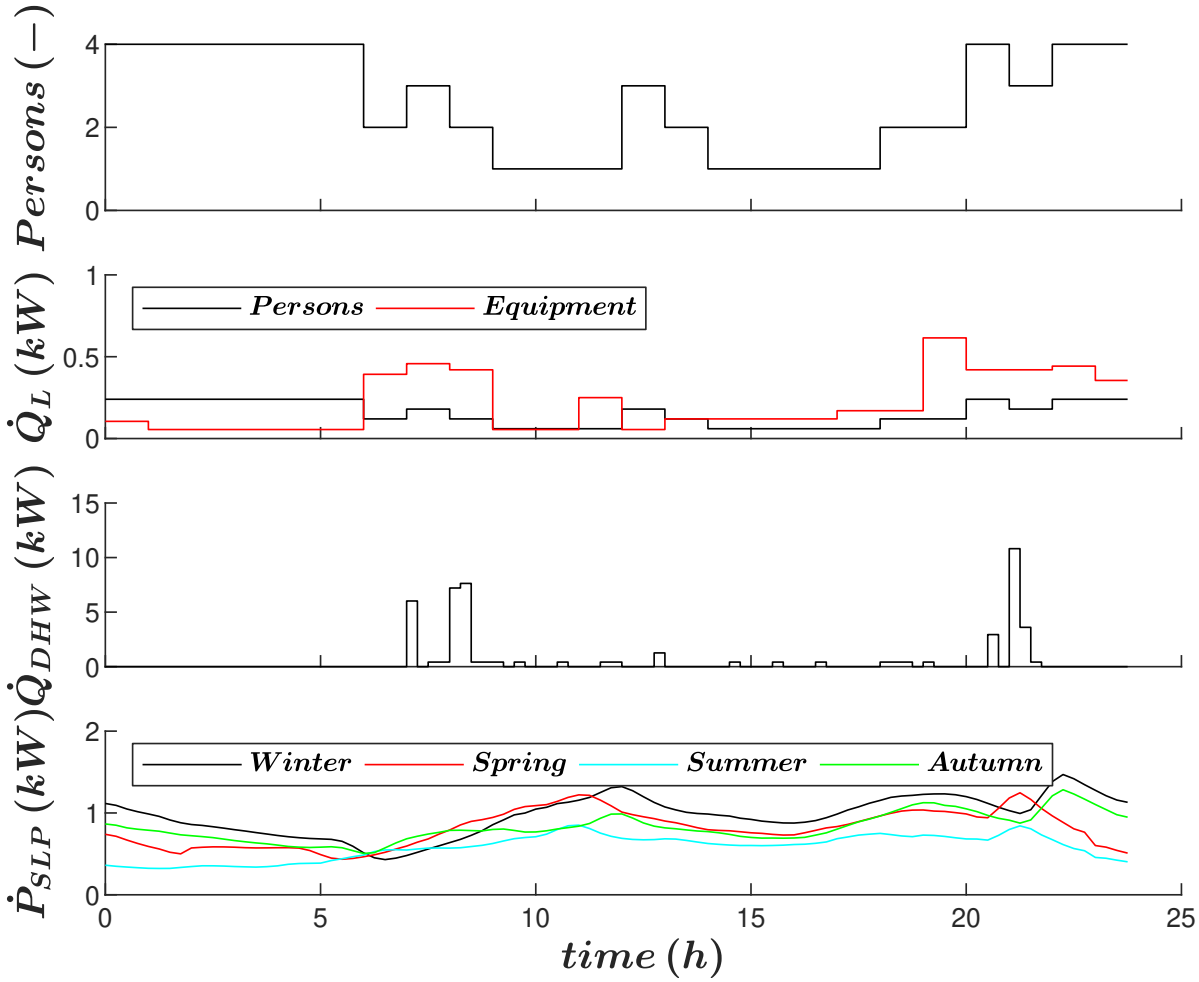

Figure 7.3: Profiles related to behavior of occupants.

Electricity Market

The price for electricity import/export $c_{elec,t}$ in Eq. (6.7) is based on historical data from the European power exchange (EPEX) of central Europe's energy day ahead market for the year 2017. The average electricity price is 0.034 €/kWh. However, these costs represent only the direct acquisition costs. Interest margins, grid fees and taxes are not considered in this work. Figure 7.4 shows the hourly changing electricity prices of the EPEX Spot for the typical days.

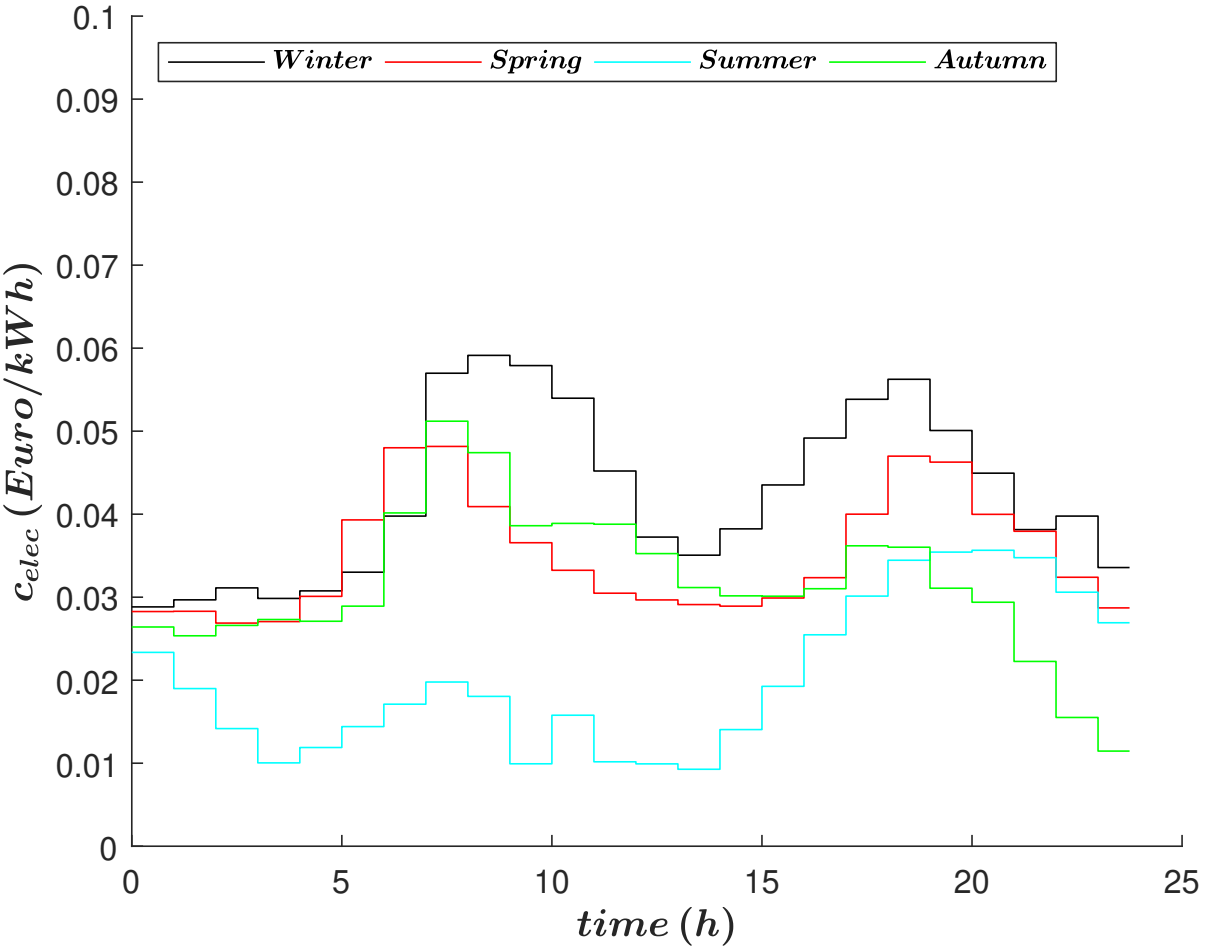

Figure 7.4: Time series of EPEX Spot day-ahead market for typical days.

7.2 Controller Design

Figure 7.5 illustrates the operating principle of the predictive controller. The different blocks of the controller are as follows:

- *MPC* computes the control input every 900 seconds by solving an optimal control problem based on the filtered state of the system and forecasted weather- , occupancy- and electricity profiles. The prediction horizon equals 12 hours with a time step of 900 seconds. The optimal control problem minimises the objective function defined in Eq. (6.7) subject to system dynamics of the building energy system and energy balance described in Chapter 5 and Chapter 6 respectively. The optimisation problem consists of continuous and binary decision variables, which results in a mixed integer linear programming problem.

- *Building Energy System* translates the control input by providing energy setpoints for convectors, power setpoints for the public power grid and charging signal for thermal energy storage. The thermal energy dissipated by the convectors is provided to the virtual building model in TRNSYS.

- *Kalman Filter* processes control inputs and measurements to compute the filtered state of the building energy system.

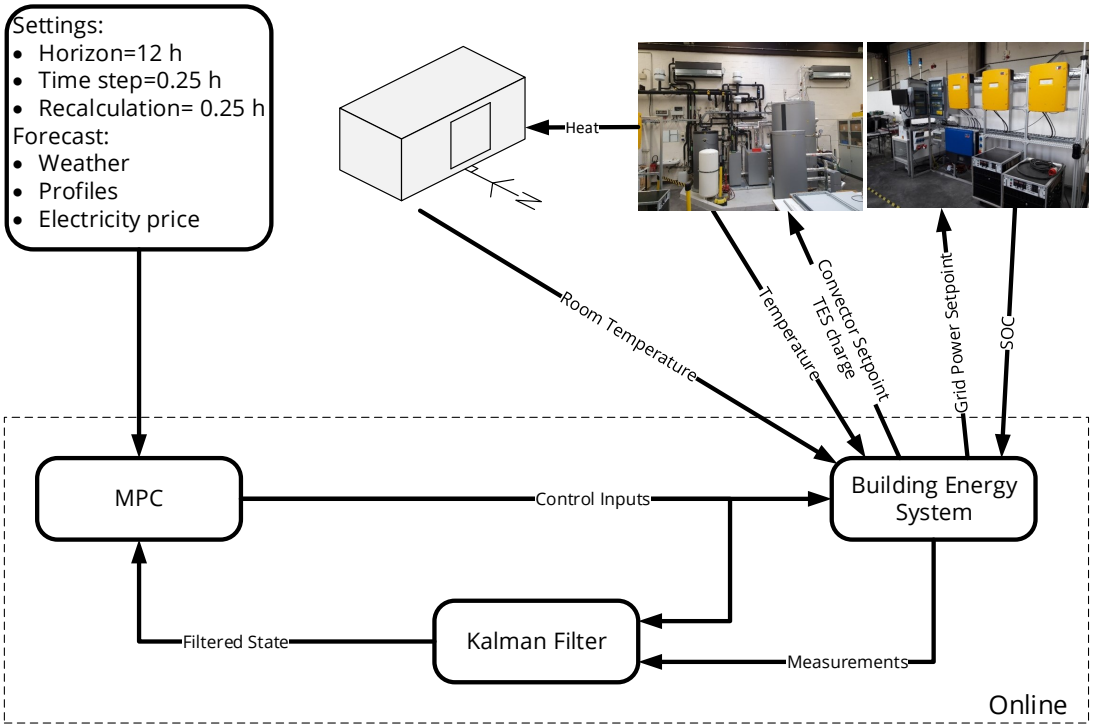

Figure 7.5: Model predictive controller structure.

Chapter 8

Economic MPC Simulations

This chapter investigates the simulation results of the mathematical models from Chapter 5 in the context of certainty equivalent economic MPC discussed in section 2.1. The simulation results partially originate from the publications [13] and [14].

8.1 Simulation Settings

Economic MPC is used to compute the optimal scheduling for a time frame of one day. The scheduling horizon is discretized into intervals of 900 seconds, which results in 96 time steps in total. The models are tested using the typical day approach and exogenous inputs presented in Chapter 7. The performance of the controller is evaluated using a reference scenario. The reference scenarios do not assume varying electricity prices but a fixed electricity price which is the arithmetic mean of the spot market price for the particular typical day. The figures used to compare the scenarios represent power flows, temperature levels, weather information and market data during the optimal scheduling of the energy system for the typical winter day and its reference scenario. Reasonable starting conditions for the hidden states of the building model in Eq. (5.42) and Eq. (5.43) are important as these determine the heating requirements of the building to a large extent. The initial states of the building are determined by means of a two-week building simulation so that the building is in a thermally stable state. This simulation is performed prior to each typical day scenario, as different weather conditions cause different states. The calculation is carried out with GUROBI 8.1 and the Matlab/Simulink toolbox Yalmip on a Windows PC with four cores and 8 GB of RAM. The relative optimality gap is equivalent to one per cent. The total number of binary and continuous decision variables is indicated in Table 8.1.

Table 8.1: Number of decision variables for the simulation environment.

Decision Variable	Number
Binary	1730
Continuous	13075

8.2 Typical Winter Simulation Results

Figure 8.1 and 8.2 represent the simulation results of the typical winter day and its reference scenario. Relevant building simulation parameters for the typical day scenario are shown in Table 8.2. The room temperature is always in the thermal comfort zone between $20°C$ and $22°C$. Temperatures in the SH and DHW TES never drop below the minimum threshold temperatures T_{hc} and T_{dhw} when heat is required. Temperatures in the SC TES remain constant as there is no cooling demand. The main environmental energy source of the DSHP is IST and WISC.

The results show that electricity prices have a considerable influence on system dynamics. Varying electricity prices lead to the fact that the DSHP mainly runs at times when the electricity price is low. This means that the heat pump mainly operates in time intervals 1-24 and 48-60. The SH TES and DHW TES are overheated to avoid electricity price peaks. The BSS fully charges during low electricity prices at the time intervals 1-20 and 53-56. Discharge occurs during peak prices by selling its energy to the market to maximise profit during the time intervals 30-40 and 73-76.

Constant electricity prices cause the heating of domestic hot water to be distributed evenly throughout the day. Overheating of the SH TES is avoided and the DSHP runs increasingly in the time intervals 48-66 to benefit from the PV production. The BSS is merely discharged, which can be traced back to efficiency losses and the associated increased energy consumption. The initial state of charge is gradually reduced from its initial SOC of 0.75 to 0.5. The total operational cost for the typical winter day equals 3.01 € and 3.76 € for the corresponding reference scenario.

Table 8.2: Building simulation parameters for typical winter day.

Parameter	Value	Units
$T_{i,min}$	20	$°C$
$T_{i,max}$	22	$°C$
$\Phi_{h,min}$	0	kW
$\Phi_{h,max}$	5	kW
$\Delta\Phi_{h,min}$	-1	kW
$\Delta\Phi_{h,max}$	1	kW

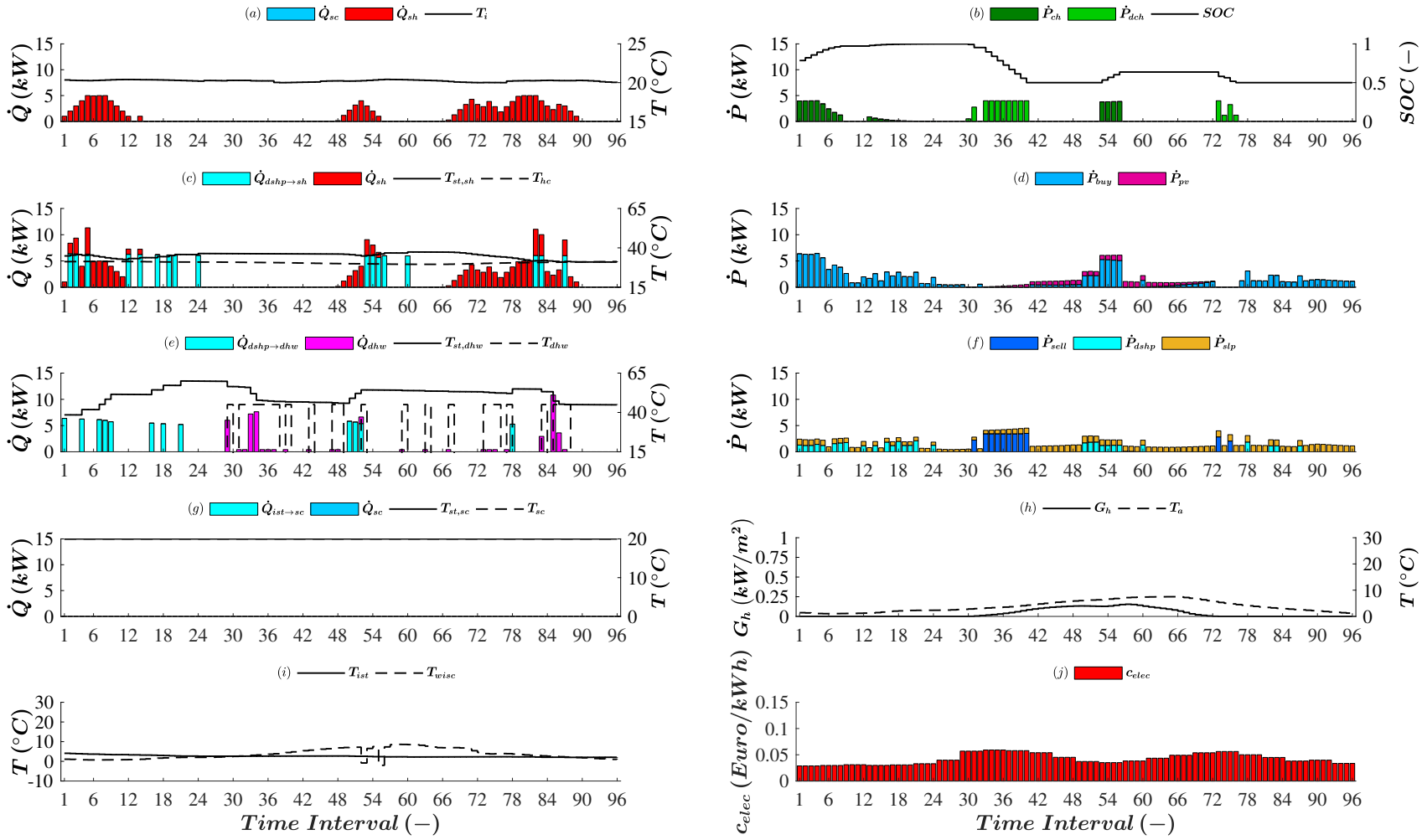

Figure 8.1: Typical winter day: (a) Power flows and temperature for building (b) Power flows and state of charge of BSS (c) Power flows and temperature for SH TES (d) Electricity produced (e) Power flows and temperature for DHW TES (f) Electricity consumed (g) Power flows and temperature for DHW TES (h) Irradiation and ambient temperature (i) Temperature for IST and WISC (j) Electricity price

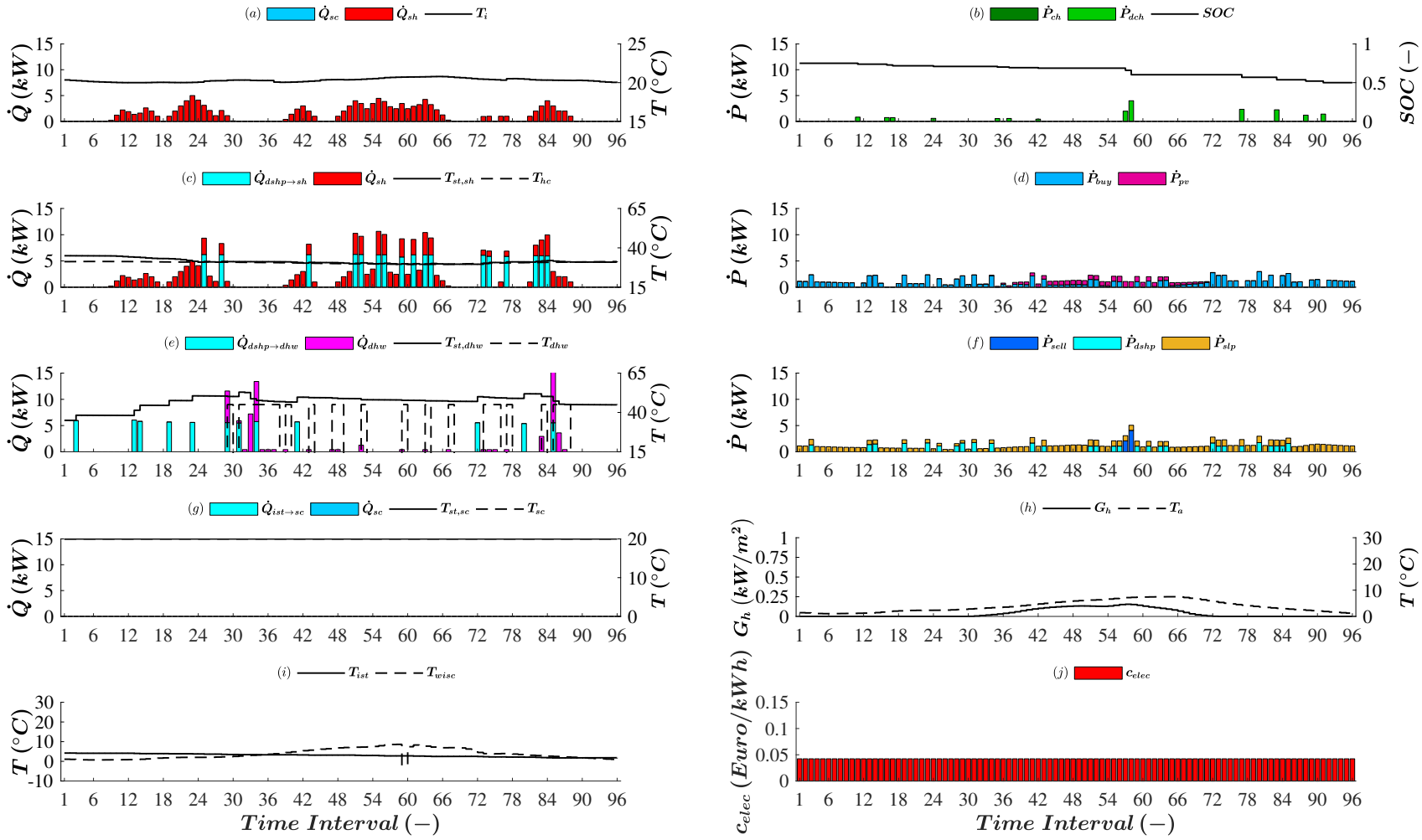

Figure 8.2: Typical winter reference day: (a) Power flows and temperature for building (b) Power flows and state of charge of BSS (c) Power flows and temperature for SH TES (d) Electricity produced (e) Power flows and temperature for DHW TES (f) Electricity consumed (g) Power flows and temperature for DHW TES (h) Irradiation and ambient temperature (i) Temperature for IST and WISC (j) Electricity price

8.3 Typical Spring Simulation Results

Figure 8.3 and 8.4 represent the simulation results of the typical spring day and its reference scenario. Relevant building simulation parameters for the typical day scenario are shown in Table 8.3. The room temperature is always in the thermal comfort zone between $20°C$ and $22°C$. Temperatures in the SC TES never exceed the maximum threshold temperature T_{sc} when cooling is required. The initial temperature of SC TES is low enough to cover the cooling demand of the building. This means that ice storage is not used for natural cooling. Temperatures in the DHW TES never drops below the minimum threshold temperature T_{dhw} when space heating is required. Temperatures in the SH TES remain constant as there is no space heating demand. The primary environmental energy source of the DSHP is IST and WISC. WISC is used to regenerate IST.

The results show that electricity prices have a considerable influence on system dynamics. Varying electricity prices lead to the fact that the DSHP mainly runs at times when the electricity price is low and PV production is high. Most of the space cooling energy is transferred to the building in the time intervals 28-36. The BSS fully charges during low electricity prices during the time intervals 9-16 and 53-60. Discharge occurs during peak prices by selling its energy to the market to maximise profit during the time intervals 25-32 and 73-80.

Constant electricity prices cause PV power production to be sold to a large extent. The rest is used to operate the DSHP and to cover the electricity needs of the inhabitants. The BSS is not subject to any charging process and is discharged from its initial SOC of 0.75 to 0.5. The total operational cost for the typical spring day equals -2.77 € and -2.84 € for the corresponding reference scenario.

Table 8.3: Building simulation parameters for typical spring day.

Parameter	Value	Units
$T_{i,min}$	20	$°C$
$T_{i,max}$	22	$°C$
$\Phi_{h,min}$	-3.2	kW
$\Phi_{h,max}$	0	kW
$\Delta\Phi_{h,min}$	-1	kW
$\Delta\Phi_{h,max}$	1	kW

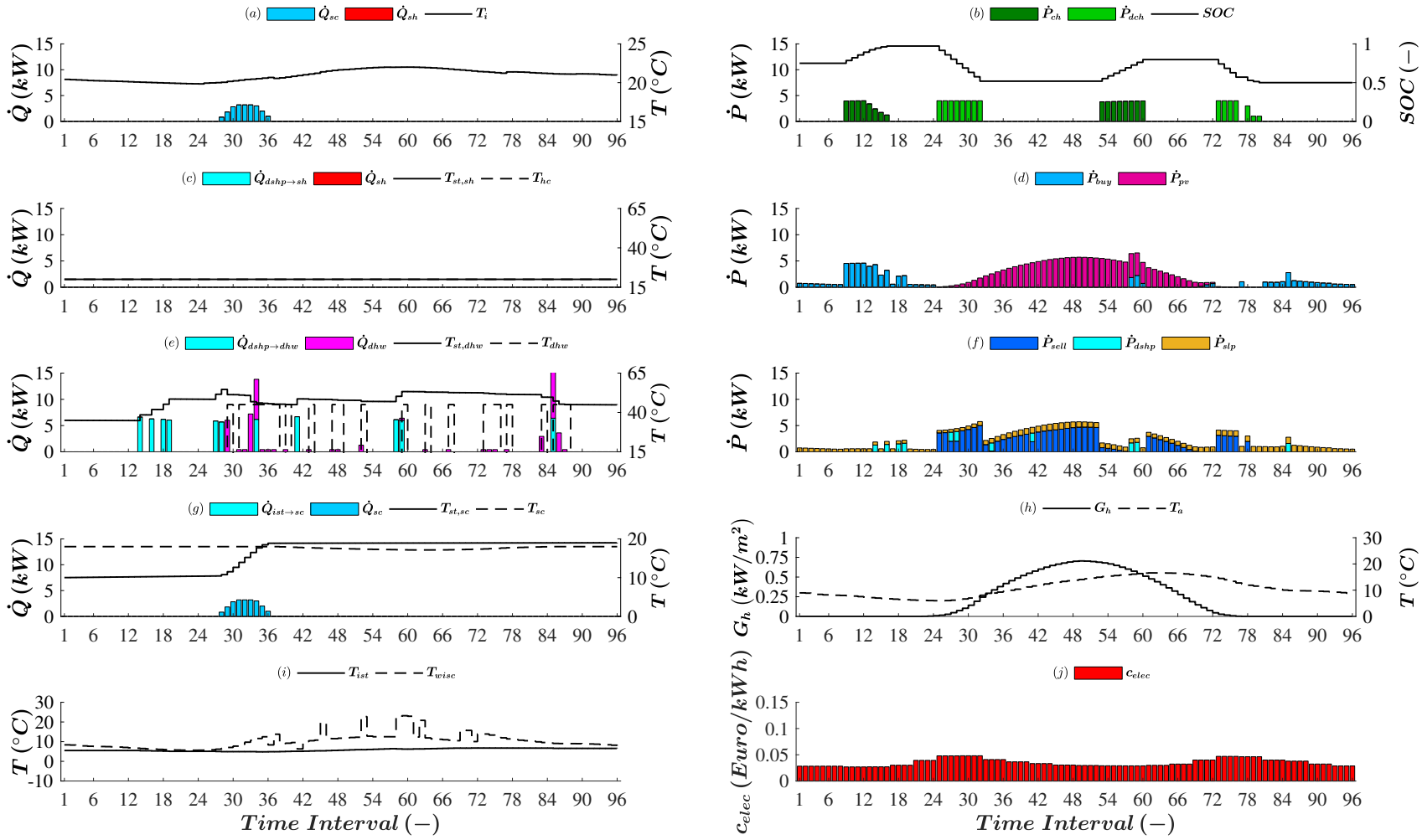

Figure 8.3: Typical spring day: (a) Power flows and temperature for building (b) Power flows and state of charge of BSS (c) Power flows and temperature for SH TES (d) Electricity produced (e) Power flows and temperature for DHW TES (f) Electricity consumed (g) Power flows and temperature for DHW TES (h) Irradiation and ambient temperature (i) Temperature for IST and WISC (j) Electricity price

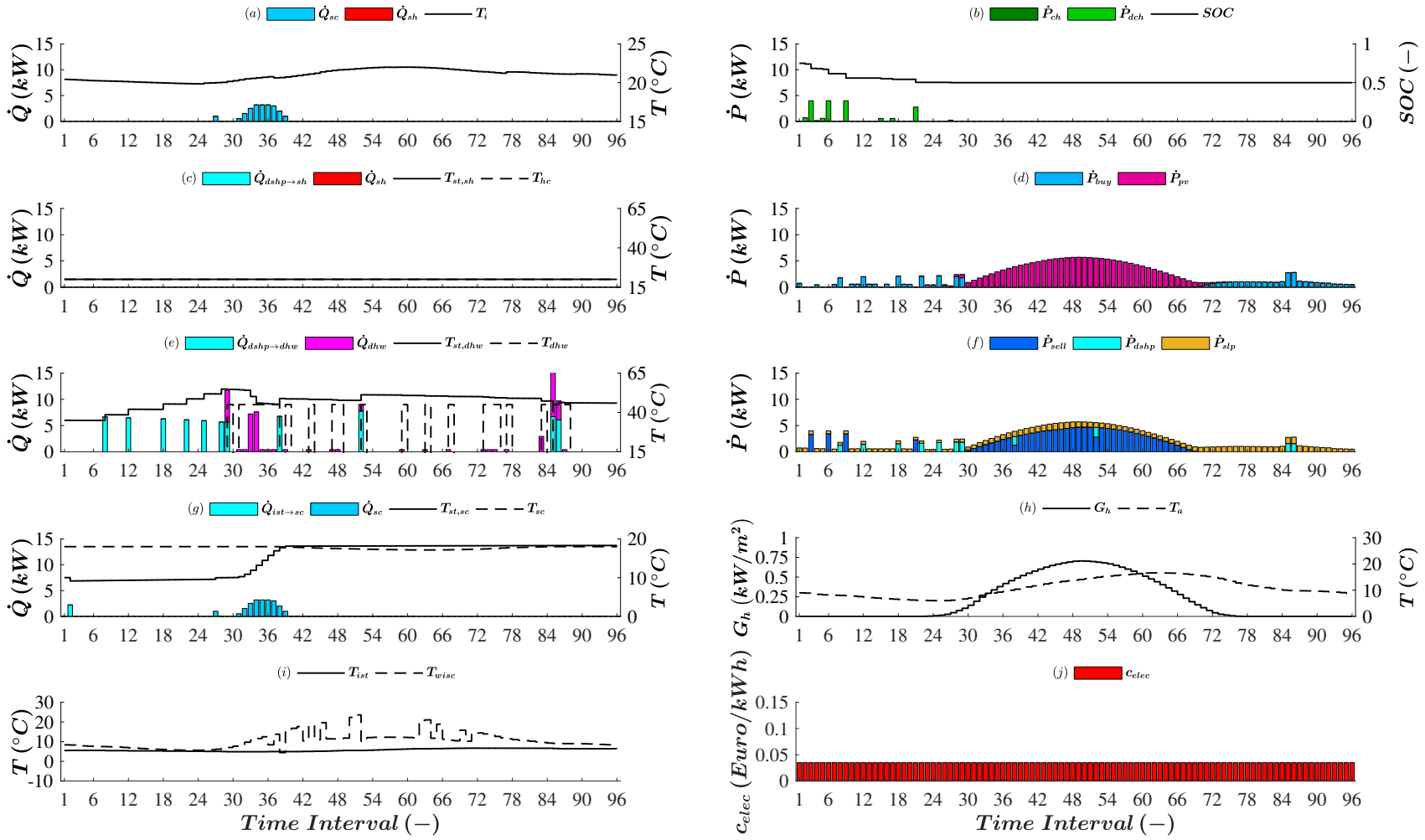

Figure 8.4: Typical spring reference day: (a) Power flows and temperature for building (b) Power flows and state of charge of BSS (c) Power flows and temperature for SH TES (d) Electricity produced (e) Power flows and temperature for DHW TES (f) Electricity consumed (g) Power flows and temperature for DHW TES (h) Irradiation and ambient temperature (i) Temperature for IST and WISC (j) Electricity price

8.4 Typical Summer Simulation Results

Figure 8.5 and 8.6 represent the simulation results of the typical summer day and its reference scenario. Relevant building simulation parameters for the typical day scenario are shown in Table 8.4.The room temperature is always in the thermal comfort zone between $20°C$ and $22°C$. Temperatures in the SC TES never exceed the maximum threshold temperature T_{sc} when cooling is required. The temperature of the SC TES is reduced by the natural cooling process of the IST. Temperatures in the DHW TES never drop below the minimum threshold temperature T_{dhw} during tapping cycles. Temperatures in the SH TES remain constant as there is no space heating demand. The main environmental energy source of the DSHP is IST and WISC. WISC is used to regenerate IST.

The results show that electricity prices have a considerable influence on system dynamics. Varying electricity prices lead to the fact that the DSHP mainly runs at times when the electricity price is low, and PV production is high. The BSS fully charges during low electricity prices and high PV production. Discharge occurs during peak prices by selling its energy to the market to maximise profit.

Constant electricity prices cause PV power production to be sold to a large extent. The rest is used to operate the DSHP and to cover the electricity needs of the inhabitants. The BSS is not subject to any charging process and is discharged from its initial SOC of 0.75 to 0.5. The total operational cost for the typical summer day equals -1.82 € and -1.77 € for the corresponding reference scenario.

Table 8.4: Building simulation parameters for typical summer day.

Parameter	Value	Units
$T_{i,min}$	20	$°C$
$T_{i,max}$	22	$°C$
$\Phi_{h,min}$	-3.2	kW
$\Phi_{h,max}$	0	kW
$\Delta\Phi_{h,min}$	-1	kW
$\Delta\Phi_{h,max}$	1	kW

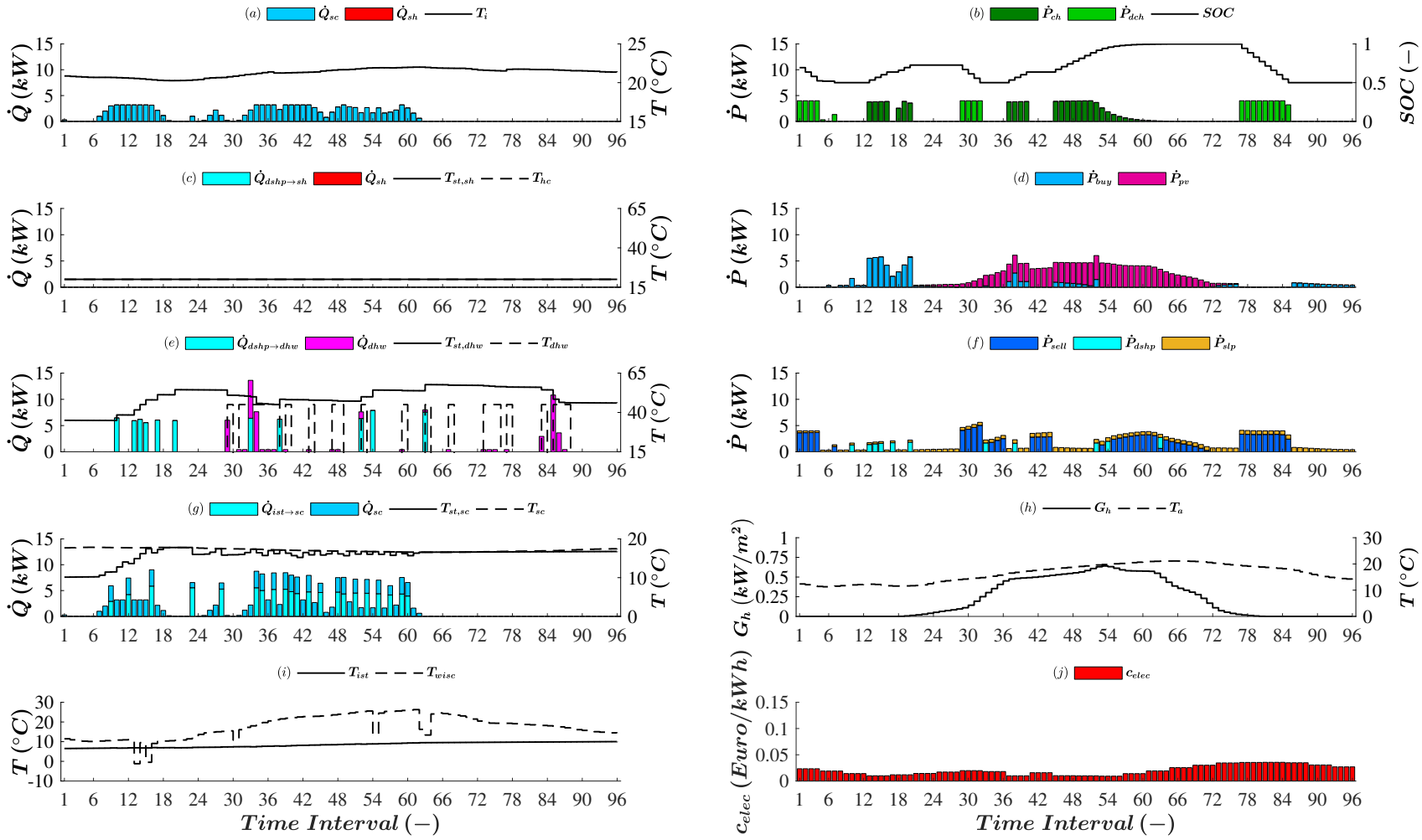

Figure 8.5: Typical summer day: (a) Power flows and temperature for building (b) Power flows and state of charge of BSS (c) Power flows and temperature for SH TES (d) Electricity produced (e) Power flows and temperature for DHW TES (f) Electricity consumed (g) Power flows and temperature for DHW TES (h) Irradiation and ambient temperature (i) Temperature for IST and WISC (j) Electricity price

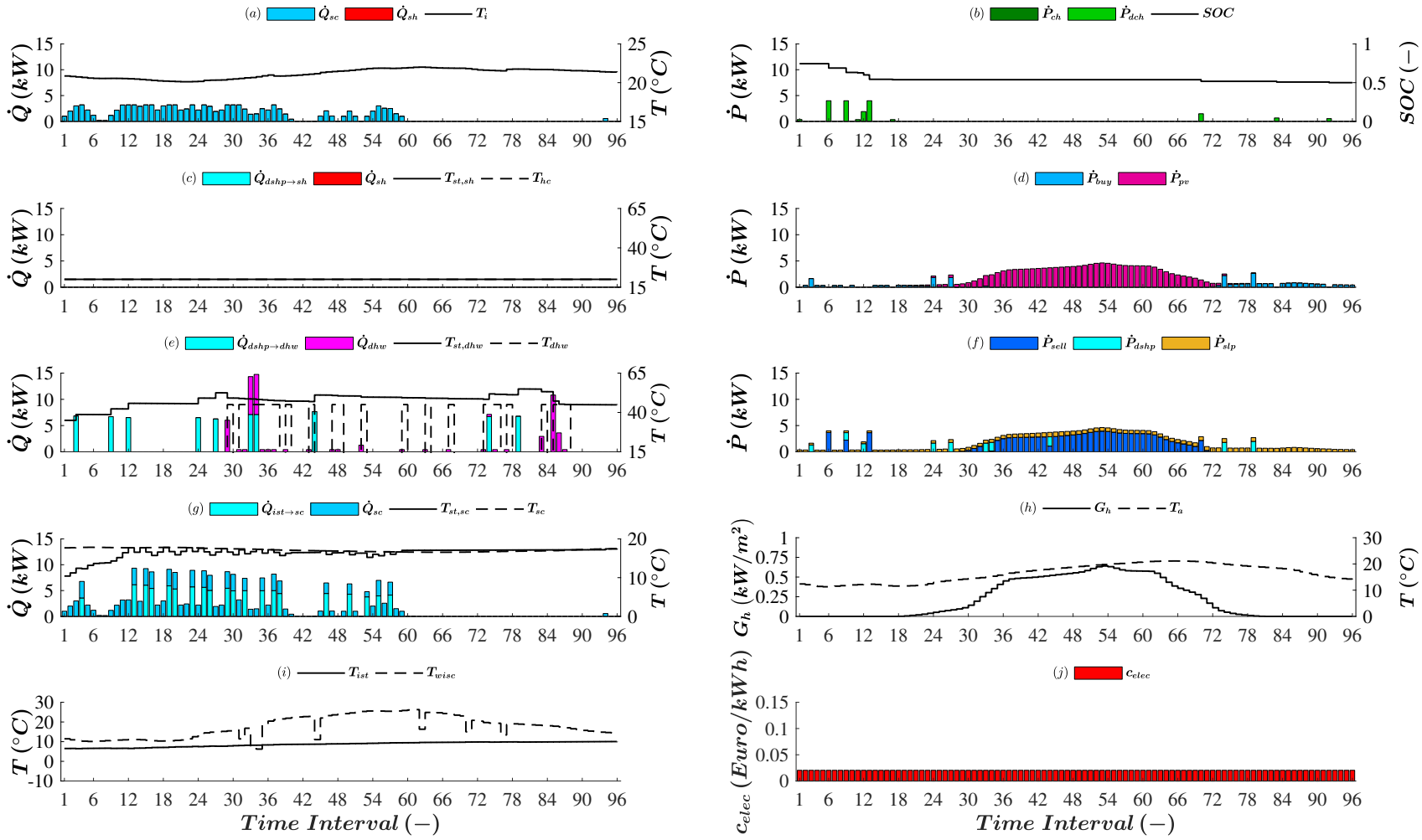

Figure 8.6: Typical summer reference day: (a) Power flows and temperature for building (b) Power flows and state of charge of BSS (c) Power flows and temperature for SH TES (d) Electricity produced (e) Power flows and temperature for DHW TES (f) Electricity consumed (g) Power flows and temperature for DHW TES (h) Irradiation and ambient temperature (i) Temperature for IST and WISC (j) Electricity price

8.5 Typical Autumn Simulation Results

Figure 8.7 and 8.8 represent the simulation results of the typical autumn day and its reference scenario. Relevant building simulation parameters for the typical day scenario are shown in Table 8.5. The room temperature is always in the thermal comfort zone between $20°C$ and $22°C$. Temperatures in the SH and DHW TES never drop below the minimum threshold temperatures T_{hc} and T_{dhw} when heat is required. Temperatures in the SC TES remain constant as there is no cooling demand.

The results show that electricity prices have a considerable influence on system dynamics. Varying electricity prices lead to the fact that the DSHP mainly runs at times when the electricity price is low. The heat pump runs increasingly in the time intervals 1-24. The main environmental energy source of the DSHP is IST. Most of the room heating energy is transferred to the building in the time intervals 1-24. The reasons for this are twofold: (1) electricity prices are low, which means that heating up the storage tank by the DSHP is more economical and (2) an earlier withdrawal of heat from the SH TES reduces the cumulative heat losses of the storage tank. The SH TES and DHW TES are overheated to avoid electricity price peaks. The BSS fully charges during low electricity prices during the time intervals 1-12. Discharge occurs during peak prices by selling its energy to the market to maximise profit during the time intervals 29-36.

Constant electricity prices lead to the DHW TES being heated up shortly before the first water tap. This avoids unnecessary heat losses. Overheating of the SH TES is avoided and the DSHP runs increasingly in the time interval 36-66 to use PV production. The BSS is not subject to any charging process and is discharged from its initial SOC of 0.75 to 0.5. The total operational cost for the typical autumn day equals 1.79 € and 2.40 € for the corresponding reference scenario.

Table 8.5: Building simulation parameters for typical autumn day.

Parameter	Value	Units
$T_{i,min}$	20	$°C$
$T_{i,max}$	22	$°C$
$\Phi_{h,min}$	0	kW
$\Phi_{h,max}$	5	kW
$\Delta\Phi_{h,min}$	-1	kW
$\Delta\Phi_{h,max}$	1	kW

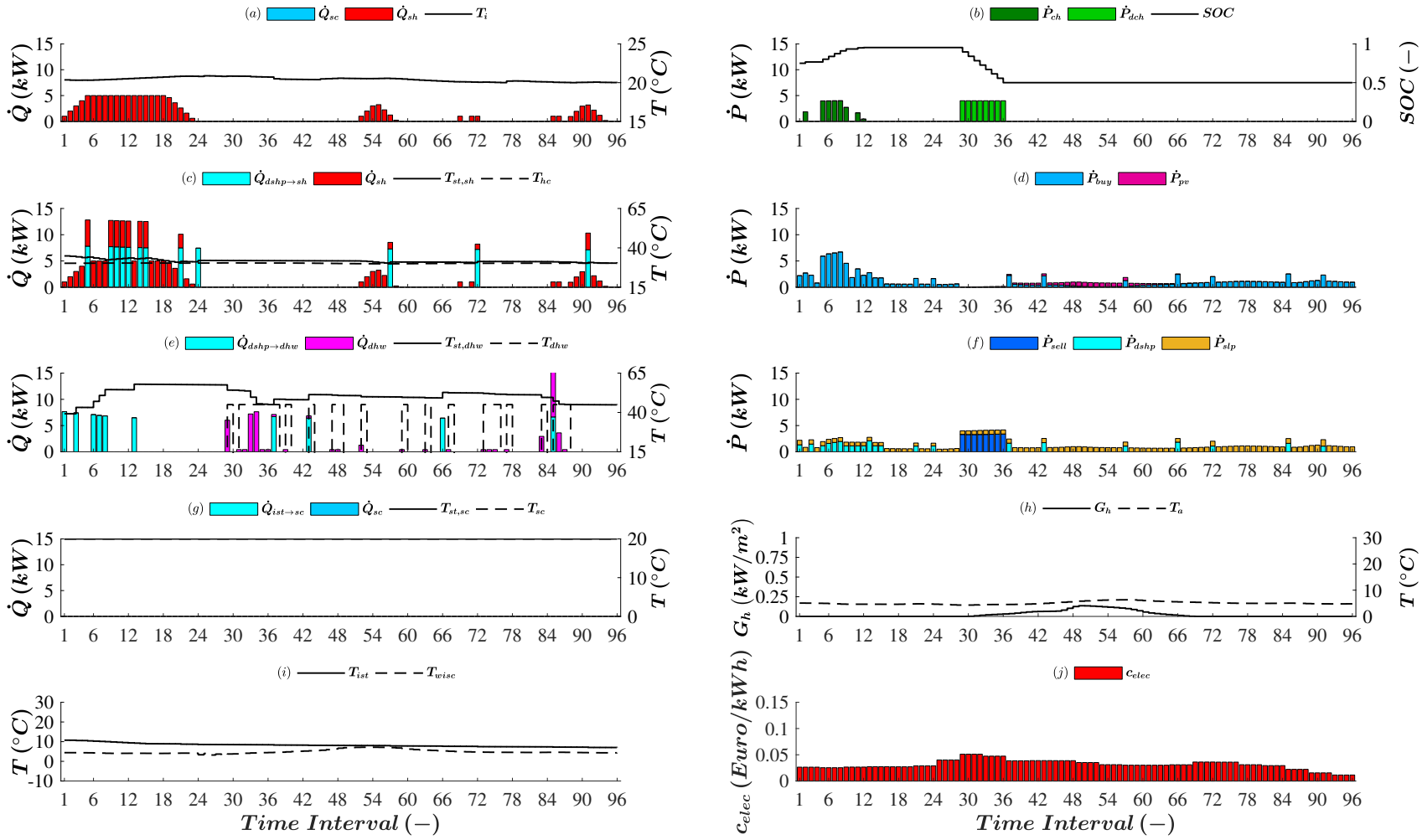

Figure 8.7: Typical autumn day: (a) Power flows and temperature for building (b) Power flows and state of charge of BSS (c) Power flows and temperature for SH TES (d) Electricity produced (e) Power flows and temperature for DHW TES (f) Electricity consumed (g) Power flows and temperature for DHW TES (h) Irradiation and ambient temperature (i) Temperature for IST and WISC (j) Electricity price

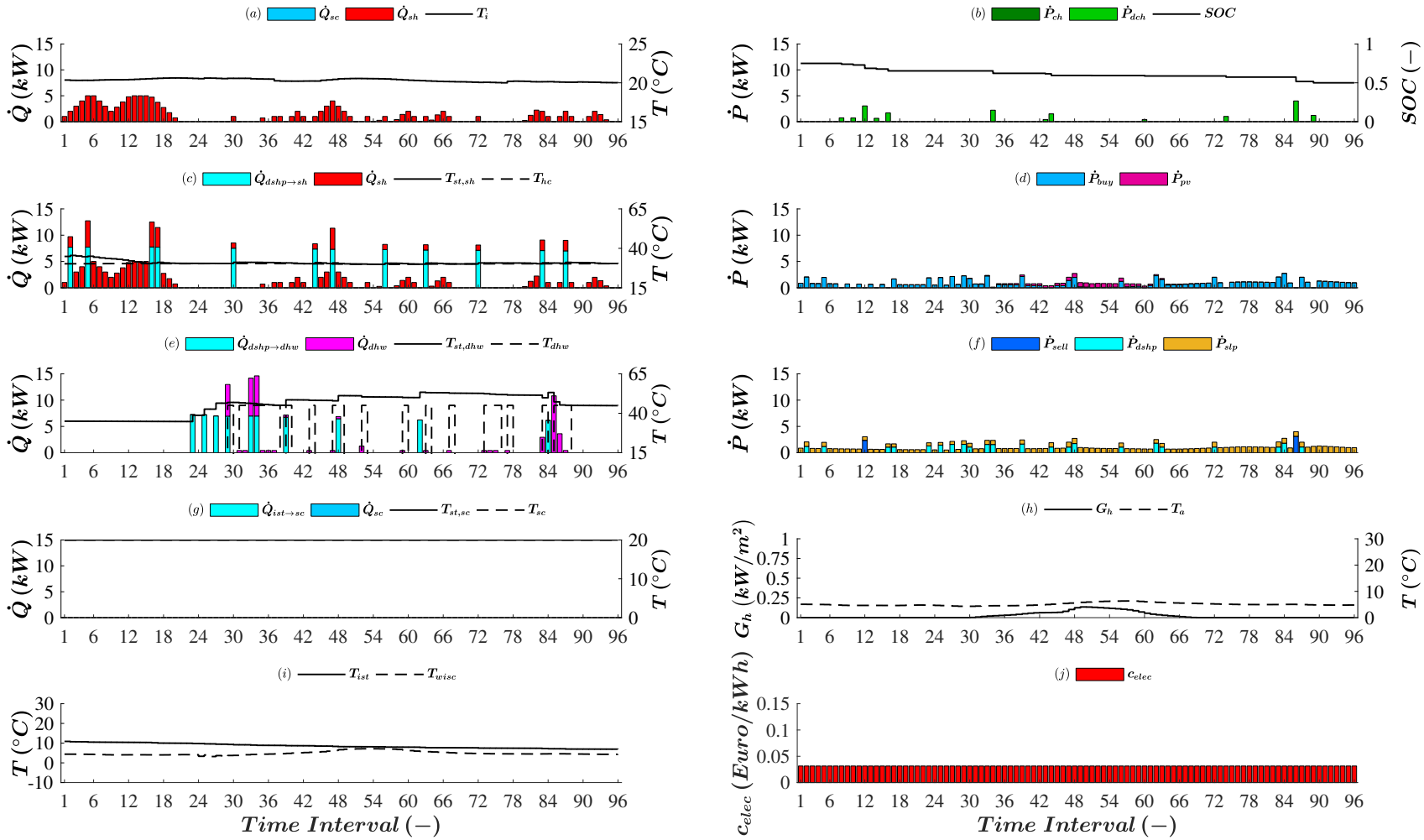

Figure 8.8: Typical autumn reference day: (a) Power flows and temperature for building (b) Power flows and state of charge of BSS (c) Power flows and temperature for SH TES (d) Electricity produced (e) Power flows and temperature for DHW TES (f) Electricity consumed (g) Power flows and temperature for DHW TES (h) Irradiation and ambient temperature (i) Temperature for IST and WISC (j) Electricity price

8.6 Summary

The simulation results show that time-varying electricity prices have a decisive influence on the dynamic behaviour of the energy system. The DSHP, as well as the heating and cooling circuits of the building, are mainly operated at times when electricity prices are low. The BSS is charged at times of low electricity prices and discharged at times of high electricity prices. The BSS is not charged in the reference scenario because efficiency losses drive up energy consumption and the associated electricity costs. Constant electricity prices and identical purchase and sales prices make BSS a redundant investment from an economic point of view. The PV production is mainly fed into the grid in both cases. The rest is used to charge the BSS, operate the DSHP and cover the electricity consumption of the residents. A comparison of the scenarios in terms of operating costs reveals an economic advantage for the scenario subject to varying electricity prices. This is the case for the typical winter, summer and autumn days. For the typical spring day, the scenario with constant electricity prices has an economic advantage. This can be explained by the low variance of the electricity price and an increased PV production. The simulation time is 85 seconds for the typical spring day and exceeds 900 seconds for the typical winter, summer and autumn day. It can, therefore, be concluded that a 24-hour calculation horizon with a time resolution of 900 seconds and a relative optimality gap of one per cent is not suitable in the present MPC setting. For this reason, the scheduling horizon is reduced to 12 hours whereas the maximum calculation time is limited to two minutes.

Chapter 9

Experimental Setup

The performance of the model predictive controller and the accuracy of the BES models are tested and validated in close to real-life conditions in the Laboratory of Energy Mix at the University of Luxembourg. For this purpose, a laboratory setup has been designed, planned and constructed based on the energy concept in Chapter 5. The laboratory setup offers the possibility to emulate a real NZEB energy system including electrical & thermal energy production, storage and consumption.

The chapter begins by highlighting the electrical components of the laboratory setup, followed by the hydraulic part. Finally, the topic of interconnectivity in the context of data exchange between the individual components of the BES is discussed.

Figure 9.1: Electrical side of the BES.

Figure 9.2: Hydraulic side of the BES.

9.1 Electrical Installation Side

PV production is volatile and is therefore unsuitable as a sole grid former. This requires additional energy storage systems to bridge the time shift between energy generation and production. The energy storage system must be regulated to ensure that the consumers have enough energy available at low solar radiation. Conversely, there can also be an overproduction of energy, which can then be used to charge the electrical energy storage system and for feeding into the public power grid. All these operations must be carefully coordinated to provide a stable grid.

This functionality is implemented using the *flexible storage system with battery backup function* by *SMA*. Illustrated in Figure 9.3, this system enables operation on- and off-grid. In the event of a grid failure, a PV system generally disconnects from the grid for

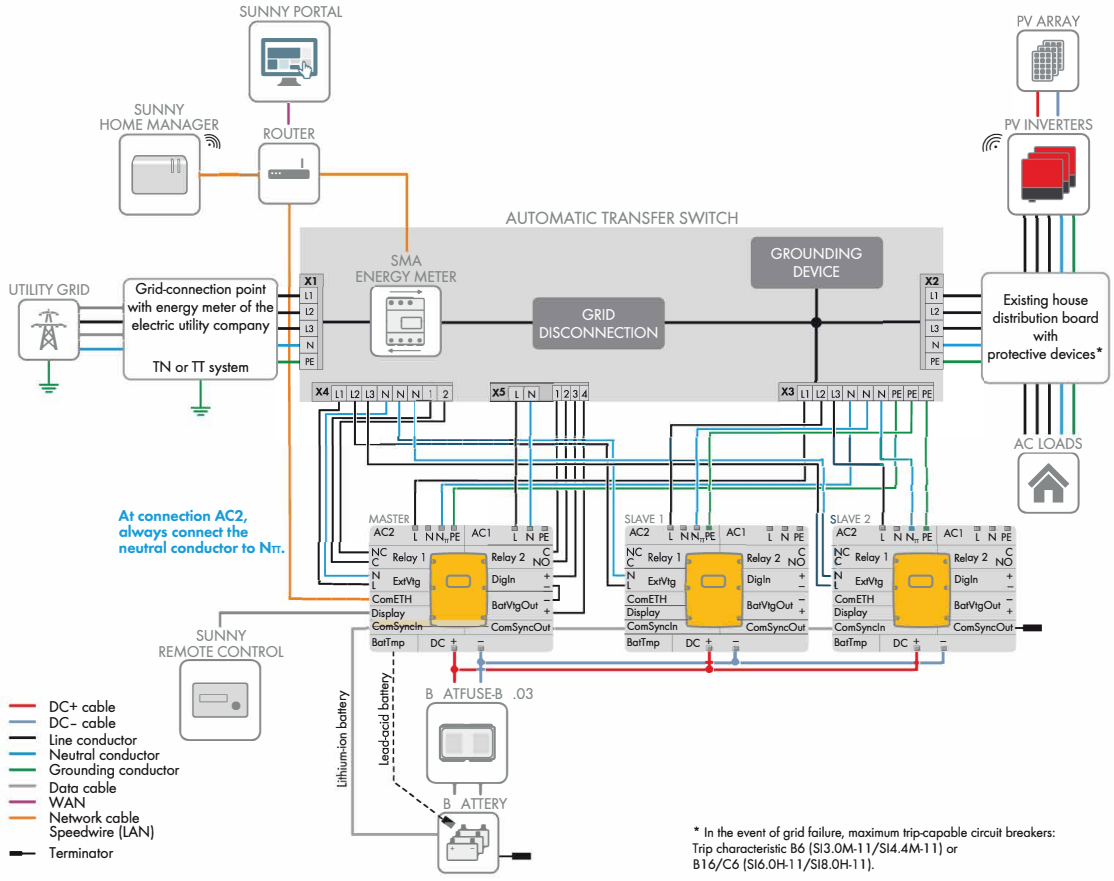

Figure 9.3: SMA Flexible Storage with Battery Backup [5].

safety reasons. As a result, the consumers are cut off from energy supply. The present system topology has an automatic transfer switch that disconnects the household grid with the PV system from the public power grid. The battery inverter Sunny Island subsequently generates a battery backup grid and the PV system can supply the consumers. When the energy demand of the active consumers exceeds the current capacity of the PV system, the battery provides the energy shortfall.

The main components of the electrical energy system are summarised in Table 9.1

Table 9.1: Main components of the electrical energy system.

Type	Description
SMA Sunny Island SI6.0H-11	Battery inverter
Hoppecke sun power VR L 2-520	Lead-gel batteries
SMA Tripower STP15000TL-10	Three-phase solar inverter
Magna-Power TSD600-24	600V 24A DC power supply
Enwitec switching box	Three-phase battery backup distribution

Battery Inverter

The single-phase battery inverter is a *Sunny Island 6.0H* manufactured by *SMA*. To create a three-phase grid, three inverters must be used. One *Sunny Island* acts as master and the other two as slaves. These battery inverters play a central role, as they specifically control the power flows of the PV system, the batteries and the public power grid. In addition, they act as a grid former in the event of a failure of the utility grid grid. The *Sunny Island* can supply a continuous power of 4.6 kW and a continuous AC current of of 20 A.

Battery

The energy storage consists of lead-gel batteries type *sun power VR L 2-520* manufactured by *Hoppecke*. A battery module has a nominal voltage of 1.8 V and a capacity of 470 Ah at C10. To meet the voltage requirements of the battery inverter, 24 battery modules are connected in series.

PV Inverter

Solar cells generate direct current which has to be converted into alternating current. The *SMA Tripower STP15000TL-10* is a three-phase solar inverter with an AC power output of 15 kW.

Solar Power Source

The PV modules must be emulated so that different scenarios can be investigated at any time of the year. For this purpose a programmable DC power supply of *Magna-Power* type *TSD600-24* is used, which provides an output power of 15 kVA. The characteristic current-voltage curves are generated in a *LabVIEW* application as a function of various module parameters, solar radiation and ambient temperature.

Switching Box

In our system, the switching box is responsible for disconnecting and grounding the connection between the public power grid and the consumer power grid. The master *Sunny*

Island automatically controls these via its two multifunctional relays. The switch box is supplied by the company *Enwitec Electronic GmbH & Co. KG*.

9.2 Thermal Installation Side

The presented thermo-hydraulic laboratory set up consists of thermal energy storing, producing and consuming components, which are presented in the following section. A detailed piping and instrumentation diagram (P&ID) is illustrated in Appendix A.

The main components of the thermal energy system are summarised in Table 9.2

Table 9.2: Main components of the thermal energy system.

Type	Description
Viessmann Vitocal 300 G BWC 301.B06	Dual source heat pump
Viessmann ES-B 10	Underground ice storage tank
Askoflow AHR-B-C	Flow heater
Viessmann AC-Box	Active cooling box
Viessmann Vitocell 100-V-CVW	DHW thermal energy storage
Viessmann Vitocell 100-E	SH thermal energy storage
ACF 00500 R	SC thermal energy storage
Denco Happel Flex Geko GF83.UWC1.FE0A1	Convector

Thermal Energy Production

A dual-source brine/water heat pump is used as a primary thermal energy producer. The used heat pump model is a *Vitocal 300 G BWC 301.B06* from Viessmann with a nominal heat capacity of 5.69 kW_{th}. Environmental energy sources are WISC type *SLK* or IST type *ES-B 10* with a volume of 10000 liters. Once the temperatures inside the ice tank are too high, it cannot be used to cool the building with natural cooling. For this specific case, the active cooling (AC) box can reverse the process of the DSHP. The evaporation process inside the heat pump keeps the SC TES within the desired temperature range. The heat, which is released on the condenser side is stored in the heat buffer for DHW or SH.

The described approach to generate heat and cold with a dual source heat pump, which draws environmental energy from WISC or IST, is a concept developed by Viessmann. In contrast to common air/water heat pumps, this concept offers the possibility to attain a higher seasonal performance factor. This results in a reduced yearly electrical energy consumption of the heat pump. In order to work independently from the weather throughout the experiments, the solar air absorbers are replaced with an electrical flow heater type *AHR-B-C* by *Askoflow*. The thermal power output is determined according to Eq. 5.19.

Thermal Energy Storage

The experimental set-up is equipped with of TES for SH, DHW and SC with respectively 2 m^3, 0.39 m^3 and 0.5 m^3. On the one hand, the TES make it possible to bridge the time lag between thermal energy generation and energy consumption, and on the other hand to increase the running time of the heat pump, which cannot be modulated.

Thermal Energy Consumption

The laboratory setup does not provide the possibility to include real thermal consumers. The time series which reflects the thermal dynamics of a building is created with TRNSYS. The elimination of thermal energy with respect to the calculated heating and cooling profiles is realized with two fan coil units type *Flex Geko GF83.UWC1.FE0A1* by *Denco Happel*, which are connected to SH and SC TES. Hot water consumption is realized with real tapping cycles according to Section 7.1.

9.3 Communication

To guarantee the interconnectivity of the BES, an adequate fieldbus system is required. In the present configuration, *Modbus TCP* and *Modbus RTU* turn out to be the greatest common denominator. Central control and monitoring of devices that do not have a *Modbus* interface is implemented by special fieldbus-specific gateways. *Modbus* is an open serial communication protocol which is based on the server/client principle. The *Modbus* protocol is a so-called application layer protocol. This means that it operates on the top level of the OSI layer model. The data transmission can take place via different channels. *Modbus RTU* uses the serial RS-485 interface and *Modbus TCP* the TCP/IP protocol.

Figure 9.4 illustrates the fieldbus connections of the laboratory setup. In the present constellation, a *Compact Rio 9039* from *National Instruments* represents the master. This reconfigurable modular embedded acquisition system includes a reconfigurable FPGA chassis and a controller programmable in *NI LabVIEW* programming language. Using the *Modbus* protocol the *Compact Rio 9039* realizes the data acquisition and control of its slaves. A human machine interface (HMI) allows a convenient selection of different test scenarios.

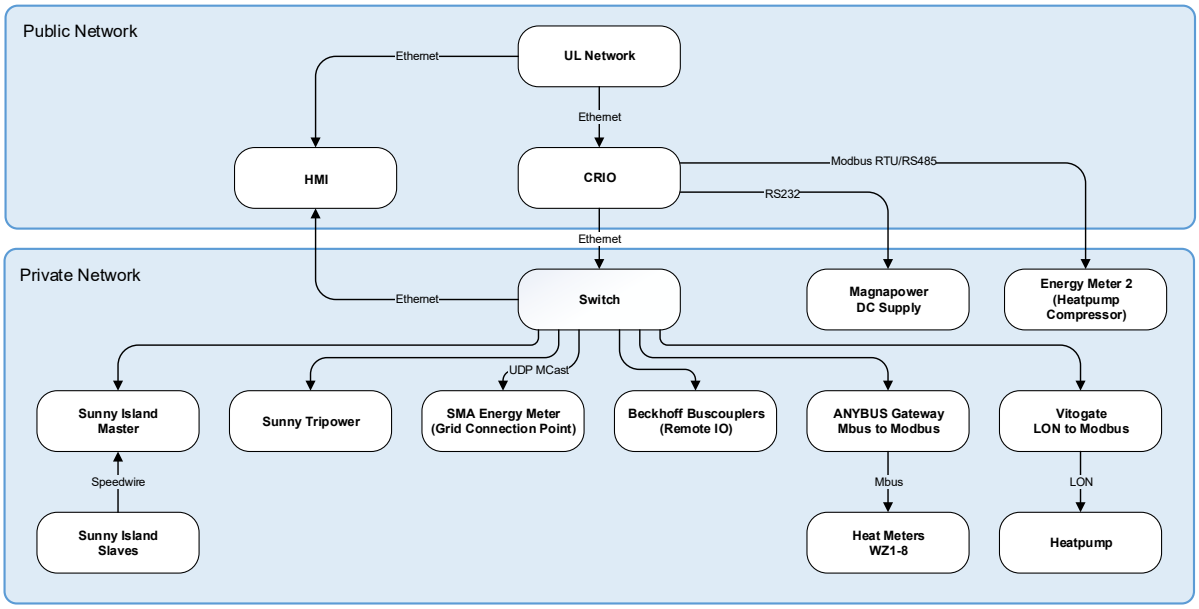

Figure 9.4: Fieldbus communication topology.

Chapter 10

Lab-Based Economic MPC

In this chapter, the specific application of MPC and RHC in a laboratory test cycle is examined. Also, individual test runs for TES and BSS are discussed in order to examine their dynamics and possible model deficits in greater detail. The comprehensive MILP framework applies the mathematical models from Chapter 5 in the context of certainty equivalent economic MPC discussed in section 2.1.

10.1 Test Run Settings

Economic MPC is used to compute the optimal scheduling for a time frame of 12 hours. The scheduling horizon is discretized into intervals of 900 seconds, which results in 48 time steps in total. The RHC approach is used to recalculate the optimal planning of the energy flow every 900 s. The predictive controller specifies which TES is to be heated, the amount of heat to be dissipated by the convectors and the power exchange with the power grid. The charging and discharging power of the BSS results indirectly from the setpoint, which determines the power exchange with the grid. The thermal energy dissipated by the convectors corresponds to the heating energy supplied to TRNSYS. The states of the BES components are determined using a Kalman filter.

In the first step, the dynamics of the BES for the typical winter day are investigated. The figures used to analyse the typical winter day scenario represent power flows, temperature levels, weather information and market data during the optimal scheduling of the energy system for the typical winter day. Power flows and temperatures correspond to real measurements. TRNSYS determines the room temperature of the NZEB. The initial states of the building are determined using a two-week building simulation so that the building is in a thermally stable state. Starting conditions for TES and BSS are chosen according to the values in section 8.2. The calculation is carried out with GUROBI 8.1 and the Matlab/Simulink toolbox Yalmip on a Windows PC with four cores and 8 GB of RAM. Matlab/Simulink exchanges data with TRNSYS and a LabVIEW application running on a Compact Rio. The relative optimality gap is equivalent to one per cent. The maximum calculation time is set to 120 s. The total number of binary and continuous decision variables is indicated in Table 10.1.

In a second step, the dynamics of the mathematical models for BSS and TES will be compared with laboratory measurements. Starting from identical initial conditions, the time series of the states are compared.

Table 10.1: Number of decision variables for the laboratory environment.

Decision Variable	Number
Binary	866
Continuous	6595

10.2 Typical Winter Laboratory Results

Figure 10.1 represents the results of the typical winter day during the laboratory test run. Relevant building simulation parameters for the typical day scenario are shown in Table 10.2. The room temperature is always in the thermal comfort zone between $20°C$ and $22°C$. Temperatures in the SH never drop below the minimum threshold temperatures T_{hc}. On the other hand, the temperature curves $T_{st,dhw}$ in the DHW TES are conspicuous, as these fall below the minimum setpoint temperature T_{dhw} in the time intervals 32-54. The reason for this is that $T_{st,dhw}$ represents the average temperature in the DHW TES. The upper temperature $T_{st,dhw,top}$ equals approximately $55°C$, which is higher than the minimum setpoint temperature T_{dhw}. The state vector of TES DHW is initialized with $T_{st,dhw}$. Therefore, the heat pump should receive the command to heat up the DHW TES in the time intervals 32-54. However, this command is not implemented because the upper temperature in the heat storage tank has reached $55°C$. Section 10.3 deals with temperature stratification in more detail.

The results show that electricity prices have a considerable influence on system dynamics. Varying electricity prices lead to the fact that the DSHP mainly runs at times when the electricity price is low. This means that the heat pump mainly operates in time intervals 1-24 and 48-66. The SH TES and DHW TES are overheated to avoid electricity price peaks. The BSS fully charges during low electricity prices at the time intervals 1-20. Discharge occurs during peak prices by selling its energy to the market to maximise profit during the time intervals 30-40 and 73-76. During the time intervals 35-48 there is a reduced discharge or even charging of the BSS because the predictive controller estimates a power consumption of the heat pump. Accordingly, the setpoint for power exchange with the grid is specified. The total operational cost for the typical winter day equals 3.46 €.

Table 10.2: Building simulation parameters for typical spring day.

Parameter	Value	Units
$T_{i,min}$	20	$°C$
$T_{i,max}$	22	$°C$
$\Phi_{h,min}$	0	kW
$\Phi_{h,max}$	2.5	kW
$\Delta\Phi_{h,min}$	-1	kW
$\Delta\Phi_{h,max}$	1	kW

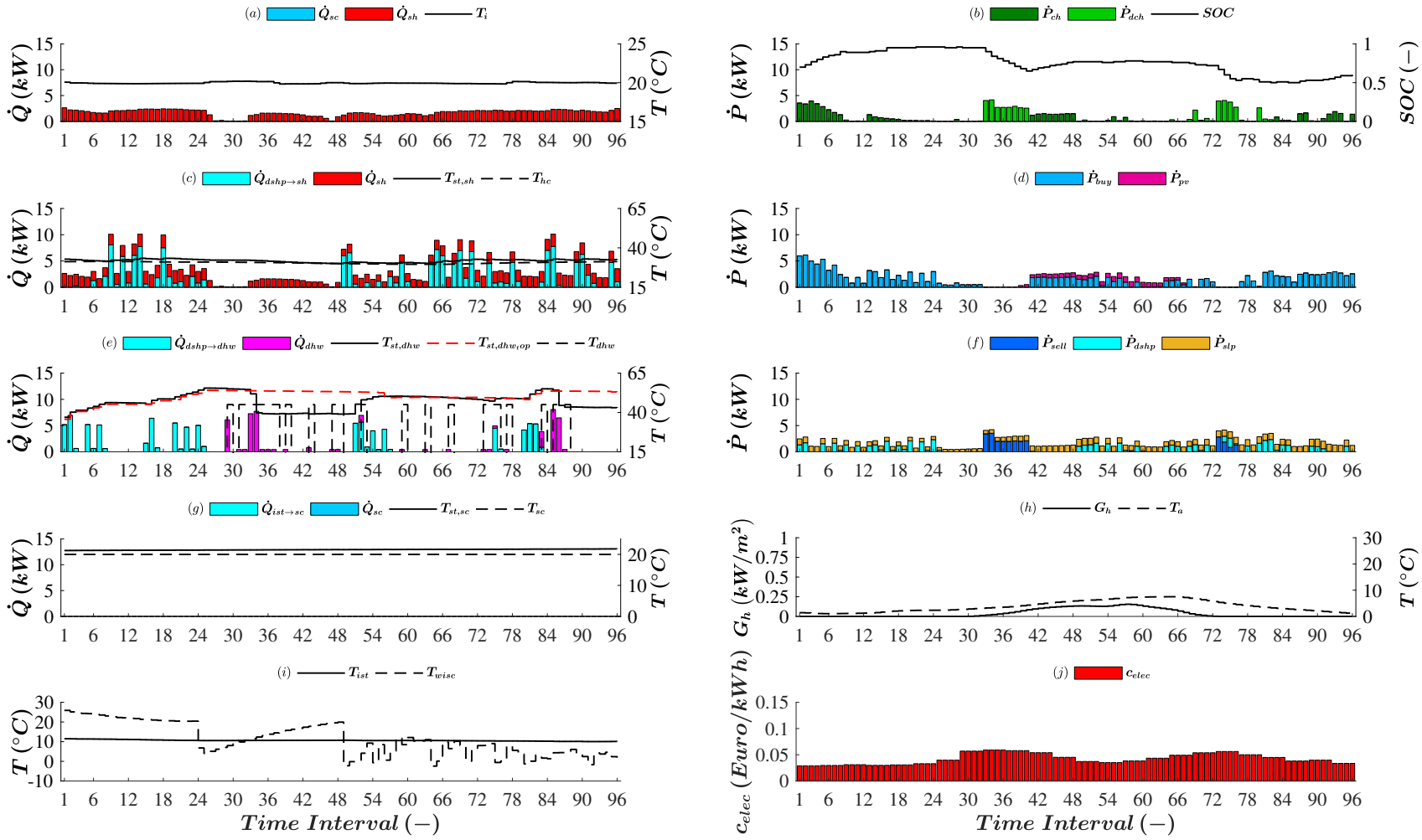

Figure 10.1: Typical Winter day: (a) Power flows and temperature for building (b) Power flows and state of charge of BSS (c) Power flows and temperature for SH TES (d) Electricity produced (e) Power flows and temperature for DHW TES (f) Electricity consumed (g) Power flows and temperature for DHW TES (h) Irradiation and ambient temperature (i) Temperature for IST and WISC (j) Electricity price

10.3 Simulation vs Measurements

Figure 10.2- 10.5 compare simulation results with laboratory measurements. For this purpose, both BSS and TES (SH, DHW and SC) were operated for 24 hours within their normal operating range. The simulation time step is 900 s. The results show that the fundamental system dynamics are captured. The root mean squared error (RMSE) is used to quantify model performance. In the case of TES, the statement can be made that the RMSE is higher if the temperature shift over the observation period is increased. This finding is best explained by the results for the DHW TES. Between hour 5 and 10 there is a major hot water tapping. During this time cold water is filled into the tank from below. A temperature stratification occurs, which can be detected by the temperature difference between $T_{st,dhw,top}$ and $T_{st,dhw,bot}$. The mathematical models for TES are not able to capture temperature stratification. For this reason, the prediction error increases as temperature stratification occurs.

Table 10.3: RMSE for BSS and TES.

Component	RMSE
BSS	0.09 (-)
SH TES	0.12 $°C$
DHW TES	8.74 $°C$
SC TES	3.76 $°C$

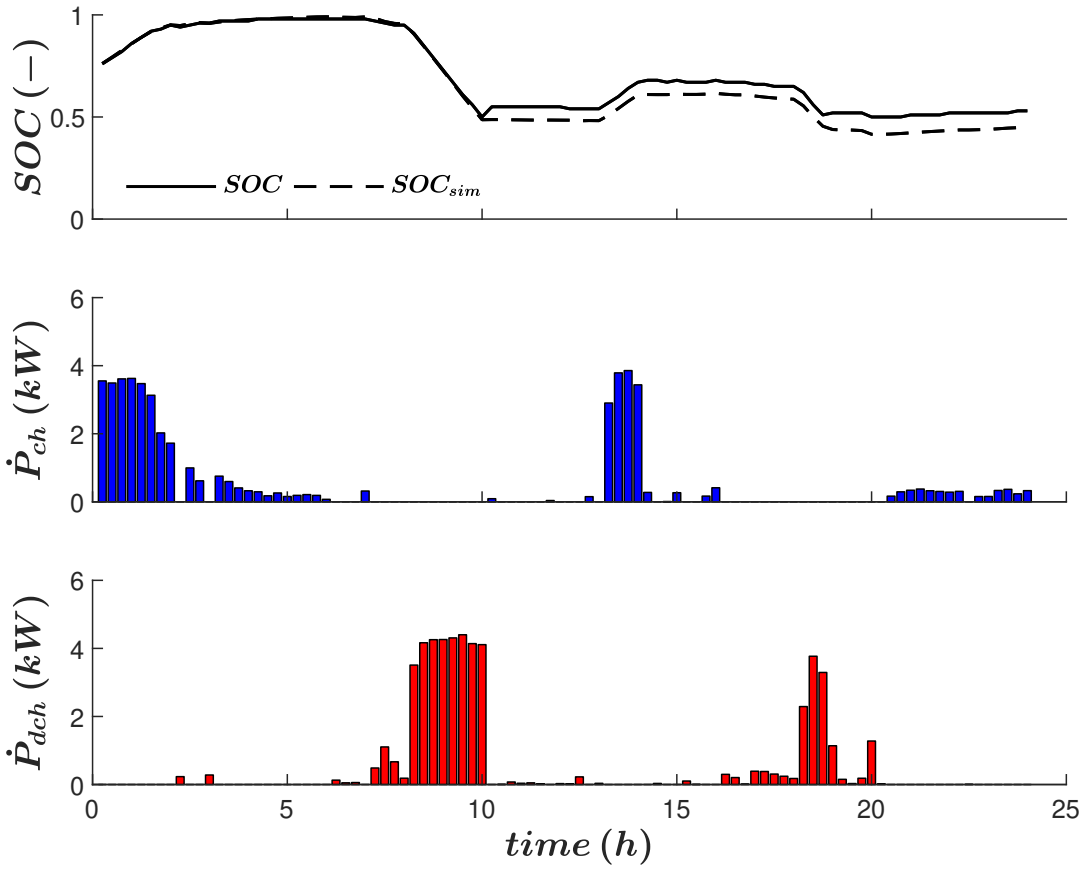

Figure 10.2: Time series laboratory measurements vs simulation for BSS.

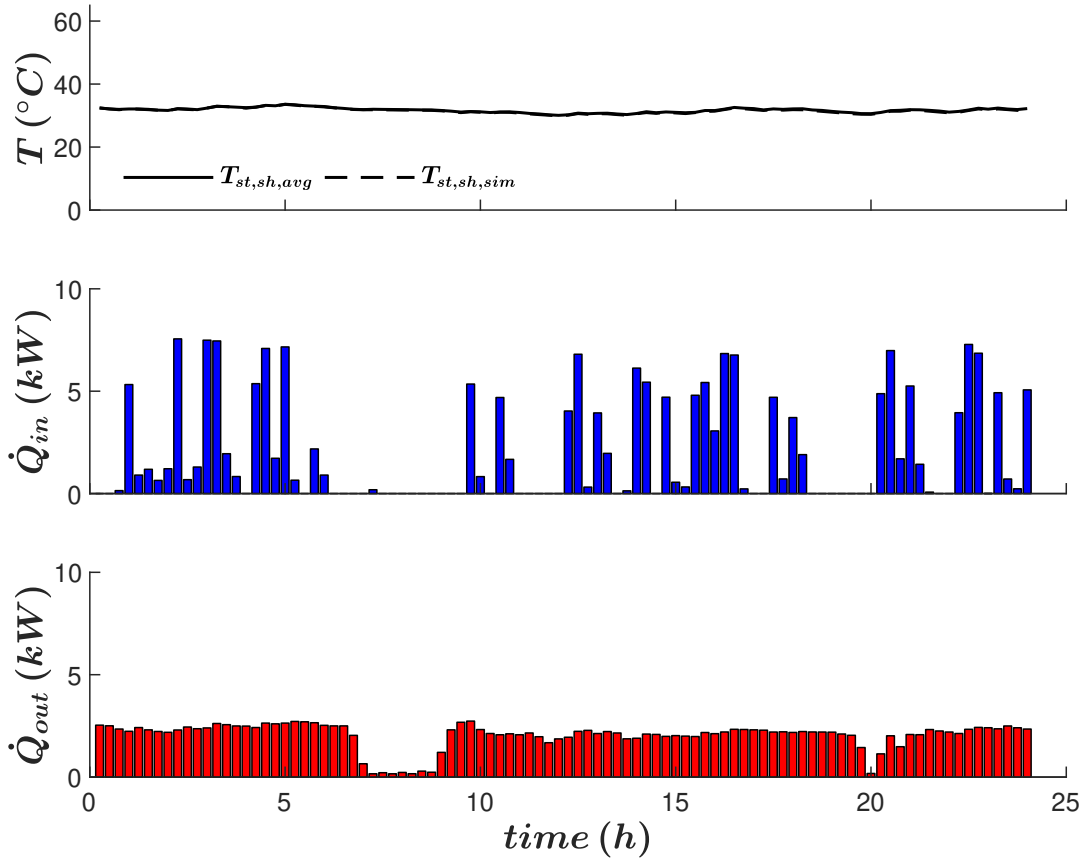

Figure 10.3: Time series laboratory measurements vs simulation for SH TES.

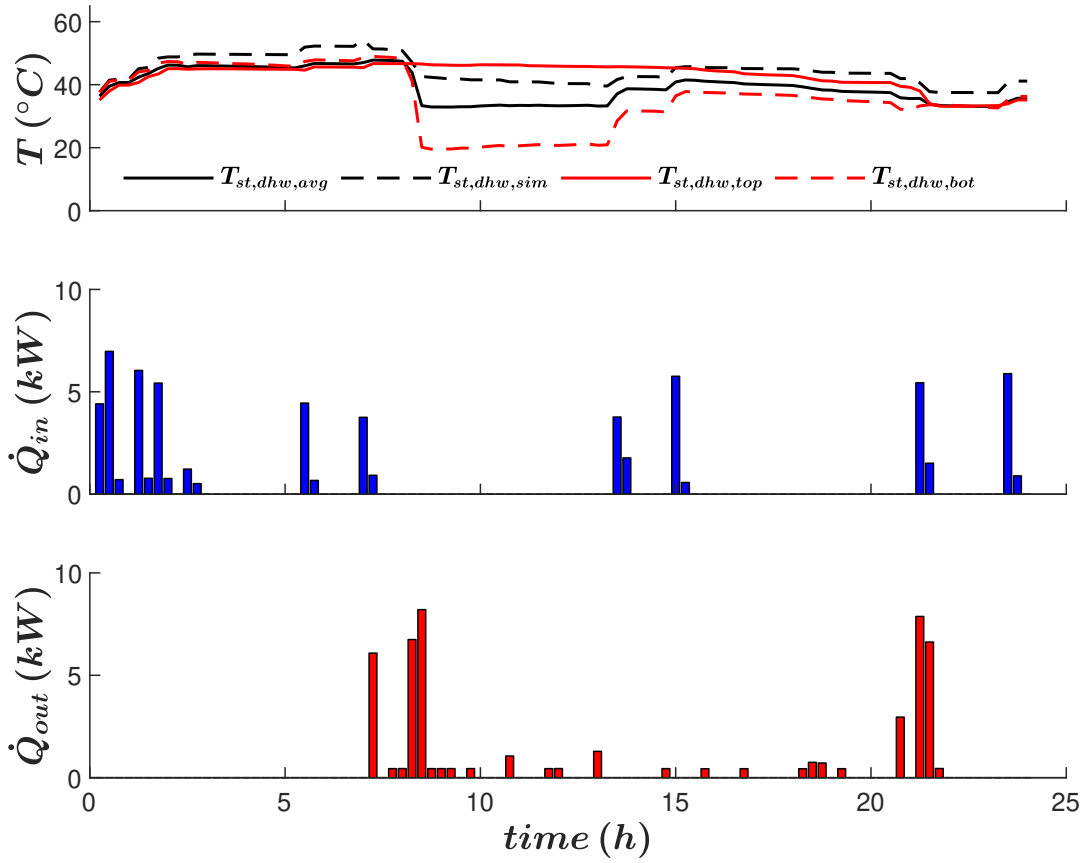

Figure 10.4: Time series laboratory measurements vs simulation for DHW TES.

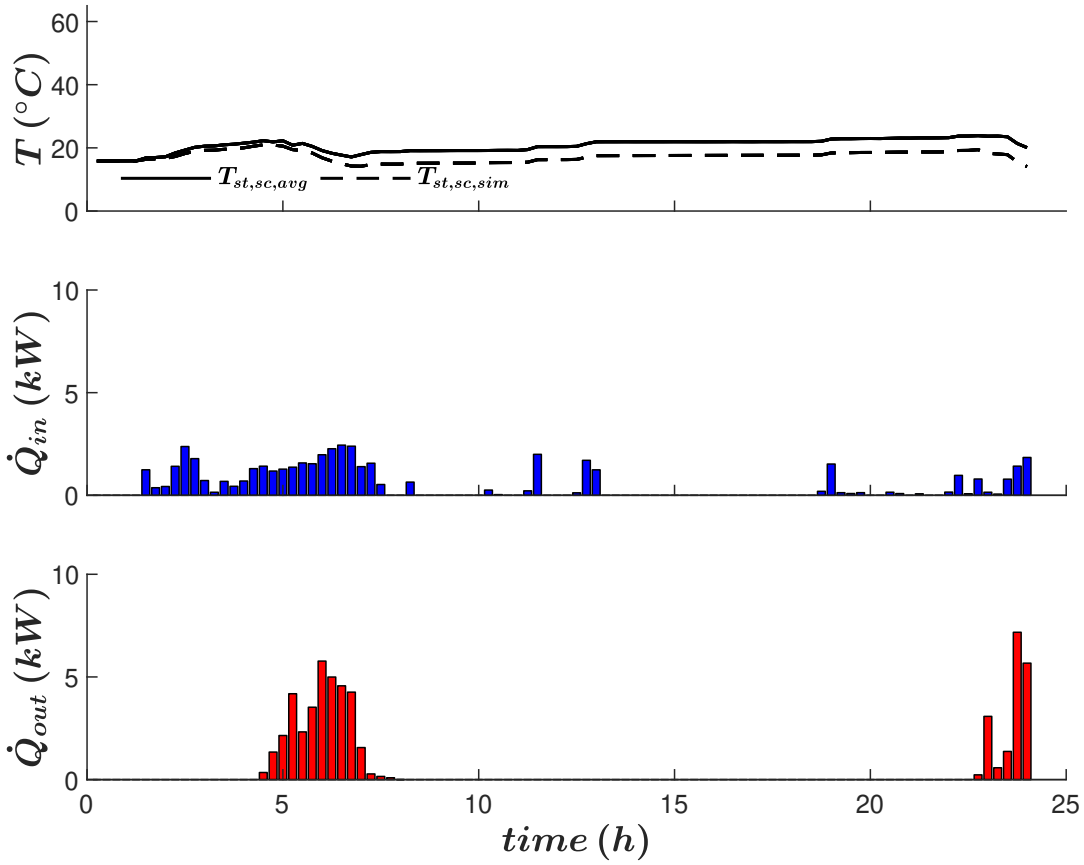

Figure 10.5: Time series laboratory measurements vs simulation for SC TES.

Chapter 11

Conclusion and Outlook

11.1 Conclusion

This work has explored the optimal operation scheduling of a building energy system in a deterministic setting using certainty equivalent economic model predictive control. The energy system consists of thermal and electrical energy storage, production and consumption units. The proposed optimisation model minimises the total costs over a scheduling horizon of 12 or 24 hours with respect to varying electricity prices. The costs arise from electricity import/export from/to the public power grid and violating hard constraints. To do so, the energy system components are modelled within a mixed integer linear programming formulation.

As part of this work, a laboratory setup was designed, planned and constructed, which is capable of covering any building-relevant types of energy, namely thermal (space heating, space cooling and domestic hot water) and electrical energy. The laboratory setup interacts with a virtual building model which is integrated into the building simulation software TRNSYS Simulation Studio.

Suitable linearised models are used to capture the dynamics of the building energy system. The models proposed in this thesis are grey box models, which apply physical information to capture the system dynamics. Model-specific parameters are determined using the maximum likelihood estimation technique. The time series required for this matter are generated with measurement series from the laboratory setup.

The level of detail of the MILP framework is determined in two ways: (1) analysis of the savings potential using various scenarios with different electricity price structures and (2) application of MPC and RHC during different test cycles in the laboratory.

The simulation results provided the insight that there is enormous cost-saving potential for demand response concerning building energy systems. However, this requires a significant variance in electricity prices to shift the operation of the BES towards periods with low tariffs. Further analysis of the MILP framework performance was done during a 24h laboratory test run using RHC. The results showed that the model reduction of the DHW TES to a single state variable can lead to complications in certain situations. This is due to the temperature stratification that occurs in the context of larger DHW tapping

cycles.

11.2 Outlook

Experts agree that MPC has many advantages over traditional control approaches in buildings. However, several challenges stand in the way of large-scale market penetration. These challenges should be addressed in future research projects. The most important of these are explained in more detail in the following.

One of the greatest challenge is the development of a predictive control system that is resilient over long periods of time against unforeseeable events such as forecast errors, sensor failures or model deviations.

Furthermore, the detailed modelling of a building energy system remains a time and cost-intensive procedure that requires expert knowledge. Learning to transfer the knowledge gained from modelling one building to another can speed up the modelling procedure immensely. These types of transfer learning are currently hotly debated in academia. However, they are still far from being widely applied in practice.

Optimal control of a complex building energy system requires continuous data acquisition, storage, visualisation and manipulation. However, decentralised topologies of energy systems, locally limited computing power and a lack of expert knowledge make this endeavour difficult. These challenges can be addressed with cloud-based solutions and should be part of future research.

Concerning extension proposals for the current laboratory setup, it is recommended to address the issue of e-mobility and shiftable loads, as these will play an important key role in the future energy system.

Bibliography

[1] European Commission. Energy Roadmap 2050. Technical Report April, 2012.

[2] Bioregional. Implementing One Planet Living: A manual. (April), 2018.

[3] M. Killian and M. Kozek. Ten questions concerning model predictive control for energy efficient buildings. *Building and Environment*, 105:403–412, 2016.

[4] Fannar Thordarson. *Grey Box Modelling of Hydrological Systems*. PhD thesis, Technical University of Denmark, 2011.

[5] SMA. Flexible Storage System with Battery Backup Function. Technical report, Niestetal, 2016.

[6] United Nations. The Paris Agreement, 2015.

[7] European Commission. A Clean Planet for all. A European long-term strategic vision for a prosperous, modern, competitive and climate neutral economy. *Com(2018) 773*, page 114, 2018.

[8] European Parliament. Directive 2018/844, 2018.

[9] European Commission. Directive 2010/31/EU on the energy performance of buildings, 2016.

[10] Federal Energy Regulatory Commission. Reports on Demand Response and Advanced Metering, 2017.

[11] Hassan Harb. *Predictive Demand Side Management Strategies for Residential Building Energy Systems*. 2017.

[12] Sasan Rafii-Tabrizi, Jean-Régis Hadji-Minaglou, Frank Scholzen, and Florin Capitanescu. Methodology for Optimally Sizing a Green Electric and Thermal Eco-Village. In *From Science To Society*. Springer, Cham, 2018.

[13] Sasan Rafii-Tabrizi, Jean-Régis Hadji-Minaglou, and Frank Scholzen. Mixed integer linear programming model for the optimal operation of a dual source heat pump. *2019 6th International Conference on Control, Decision and Information Technologies, CoDIT 2019*, 2019.

[14] Sasan Rafii-Tabrizi, Jean-Régis Hadji-Minaglou, Frank Scholzen, and Florin Capitanescu. Optimal Operation of Nearly Zero Energy Buildings using Mixed Integer Linear Programming. In *2019 International Conference on Smart Energy Systems and Technologies (SEST)*, Porto, sep 2019. IEEE.

[15] Steffen Bechtel, Sasan Rafii-Tabrizi, Frank Scholzen, and Jean-Régis Hadji-Minaglou. Demand-Side-Management Potentials for Heat Pumps in Residential Buildings. In V. et al. Corrado, editor, *16th International Conference of the International Building Performance Simulation Association*, Rome, 2019. International Building Performance Simulation Association.

[16] Steffen Bechtel, Sasan Rafii-Tabrizi, Frank Scholzen, Jean-Régis Hadji-Minaglou, and Stefan Maas. Influence of thermal energy storage and heat pump parametrization for demand-side-management in a nearly-zero-energy-building using model predictive control. *Energy and Buildings*, nov 2020.

[17] J. Richalet, A. Rault, J.L. Testud, and J. Papon. Model predictive heuristic control. *Automatica*, 14(5):413–428, sep 1978.

[18] Charles R. Cutler and B. L. Ramaker. Dynamic matrix control. A computer control algorithm. In *Proceedings of the Joint Automatic Control Conference*, San Francisco, 1979.

[19] J.M. Maciejowski, P.J. Goulart, and E.C. Kerrigan. Constrained Control Using Model Predictive Control. In *Advanced Strategies in Control Systems with Input and Output Constraints*, volume 346, pages 273–291. Springer Berlin Heidelberg, Berlin, Heidelberg, 2007.

[20] E. F. Camacho and C. Bordons. *Model Predictive control*. Number 2 in Advanced Textbooks in Control and Signal Processing. Springer London, London, 2007.

[21] James Rawlings, David Mayne, and Moritz Diehl. *Model Predictive Control: Theory, Computation and Design*, volume 197. Nob Hill Publishing, Santa Barbara, 2 edition, 2017.

[22] Jiří Cigler, Jan Siroky, Milan Korda, and Colin N. Jones. On the Selection of the Most Appropriate MPC Problem. *Clima - RHEVA World Congress*, 2013.

[23] Francesco Smarra, Achin Jain, Tullio de Rubeis, Dario Ambrosini, Alessandro D'Innocenzo, and Rahul Mangharam. Data-driven model predictive control using random forests for building energy optimization and climate control. *Applied Energy*, 226(September 2017):1252–1272, 2018.

[24] Sebastian Kuboth, Florian Heberle, Andreas König-Haagen, and Dieter Brüggemann. Economic model predictive control of combined thermal and electric residential building energy systems. *Applied Energy*, 240(February):372–385, 2019.

[25] Tom Terlouw, T. Alskaif, Christian Bauer, and Wilfried van Sark. Optimal energy management in all-electric residential energy systems with heat and electricity storage. *Applied Energy*, 254(July):113580, 2019.

[26] Laura Standardi. *Economic Model Predictive Control for Large-Scale and Distributed Energy Systems*. PhD thesis, Technical University of Denmark, 2015.

[27] Amin Khodaei. Microgrid Optimal Scheduling With Multi-Period Islanding Constraints. *IEEE Transactions on Power Systems*, 29(3):1383–1392, may 2014.

[28] John Bagterp Jørgensen, Leo Emil Sokoler, Laura Standardi, Rasmus Halvgaard, Tobias Gybel Hovgaard, Gianluca Frison, Niels Kjølstad Poulsen, and Henrik Madsen. Economic MPC for a linear stochastic system of energy units. *2016 European Control Conference, ECC 2016*, pages 903–909, 2017.

[29] Melanie N. Zeilinger, Manfred Morari, and Colin N. Jones. Soft constrained model predictive control with robust stability guarantees. *IEEE Transactions on Automatic Control*, 59(5):1190–1202, 2014.

[30] George Dantzig. *Linear Programming and Extensions*, volume 114. RAND Corporation, 1963.

[31] N. Karmarkar. A new polynomial-time algorithm for linear programming. *Combinatorica*, 4(4):373–395, dec 1984.

[32] Radosław Hofman. Why LP cannot solve large instances of NP-complete problems in polynomial time. *Lecture Notes in Engineering and Computer Science*, pages 596–599, 2007.

[33] A. H. Land and A. G. Doig. An Automatic Method of Solving Discrete Programming Problems. *Econometrica*, 28(3):497, jul 1960.

[34] R. J. Dakin. A tree-search algorithm for mixed integer programming problems. *The Computer Journal*, 8(3):250–255, mar 1965.

[35] Alessandro Beltramin and Matteo Fischetti. *Modern branch-and-cut solvers for Mixed-Integer Linear Programming: a computational comparison.* magistrale in ingegneria informatica mixed-integer, Università degli studi di Padova, 2014.

[36] Ralph E. Gomory. Outline of an Algorithm for Integer Solutions to Linear Programs. *Bulletin of the American Mathematical Society*, 64(5):275–278, 1958.

[37] P. C. Gilmore and R. E. Gomory. A Linear Programming Approach to the Cutting-Stock Problem. *Operations Research*, 9(6):849–859, 1961.

[38] Johan Efberg. YALMIP : A toolbox for modeling and optimization in MATLAB. *IEEE*, pages 284–289, 2004.

[39] LLC Gurobi Optimization. Gurobi Optimizer Reference Manual, 2019.

[40] IBM. IBM ILOG CPLEX Optimization Studio, 2019.

[41] Sebastian Kuboth, Florian Heberle, Andreas König-Haagen, and Dieter Brüggemann. Economic model predictive control of combined thermal and electric residential building energy systems. *Applied Energy*, 240(December 2018):372–385, 2019.

[42] Clara Verhelst. *Model Predictive Control of Ground Coupled Heat Pump Systems.* Number April. 2012.

[43] Michael Sterner and Ingo Stadler. *Handbook of Energy Storage*. Springer Berlin Heidelberg, Berlin, Heidelberg, 2019.

[44] Søren Østergaard, Anna Marszal-pomianowska, Roberto Lollini, Wilmer Pasut, Armin Knotzer, Peter Engelmann, Anne Stafford, and Glenn Reynders. IEA EBC Annex 67 Energy Flexible Buildings. *Energy & Buildings*, 155(2017):25–34, 2020.

[45] G. J. Levermore. *Building Energy Management Systems: Applications to Low-energy HVAC and Natural Ventilation Control*. E & FN Spon, London, 2 edition, 2000.

[46] Mohammad Royapoor, Anu Antony, and Tony Roskilly. A review of building climate and plant controls , and a survey of industry perspectives. *Energy & Buildings*, 158:453–465, 2018.

[47] Damien Picard and Lieve Helsen. Cloud-based implementation of white-box model predictive control for a GEOTABS office building : A field test demonstration. *Journal of Process Control*, 88:63–77, 2020.

[48] H Viot, A Sempey, L Mora, J C Batsale, and J Malvestio. Energy & Buildings Model predictive control of a thermally activated building system to improve energy management of an experimental building : Part I - Modeling and measurements. *Energy & Buildings*, 172:94–103, 2018.

[49] H Viot, A Sempey, L Mora, J C Batsale, and J Malvestio. Energy & Buildings Model predictive control of a thermally activated building system to improve energy management of an experimental building : Part II - Potential of predictive strategy. *Energy & Buildings*, 172:385–396, 2018.

[50] Daniel Wolf and Clemens Pollerberg. Supervisory model predictive control for PV battery and heat pump system with phase change slurry thermal storage. 2020.

[51] Felix Bünning, Benjamin Huber, Philipp Heer, Ahmed Aboudonia, and John Lygeros. Experimental demonstration of data predictive control for energy optimization and thermal comfort in buildings. 211, 2020.

[52] Enrico Reticcioli and Alessandro D Innocenzo. NeurOpt: Neural network based optimization for building energy management and climate control. *Systems and Control*, 2020.

[53] Henrik Madsen. Modelling Non-Linear and Non-Stationary Time Series. Technical report, Technical University of Denmark, Copenhagen, 2006.

[54] Philip Delff Andersen. *Models for the energy performance of low-energy houses*. PhD thesis, Technical University of Denmark, 2013.

[55] Charles F Van Loan. Computing Integrals Involving. *IEEE Transactions on Automatic Control*, 23(3):395–404, 1978.

[56] Henrik Madsen. *Time Series Analysis*. Chapman and Hall/CRC, nov 2007.

[57] Rune Juhl, Jan Kloppenborg Møller, and Henrik Madsen. ctsmr - Continuous Time Stochastic Modeling in R. Technical Report June, Technical University of Denmark, Copenhagen, 2016.

[58] R. E. Kalman. A new approach to linear filtering and prediction problems. *Journal of Fluids Engineering, Transactions of the ASME*, 82(1):35–45, 1960.

[59] Anna Scaglione and Ronald Melton. Information processing for the power switch. *IEEE SIGNAL PROCESSING MAGAZINE*, (SEPTEMBER):55–67, 2012.

[60] John S. Vardakas, Nizar Zorba, and Christos V. Verikoukis. A Survey on Demand Response Programs in Smart Grids: Pricing Methods and Optimization Algorithms. *IEEE Communications Surveys & Tutorials*, 17(1):152–178, 2015.

[61] University of Wisconsin-Madison. Solar Energy Laboratory. *TRNSYS, a transient simulation program*. Madison, Wis. : The Laboratory, 1975., 1975.

[62] Walter Grassi. *Heat Pumps, Fundamentals and Applications*. Springer International Publishing, 2018.

[63] Viessmann. Technical Guide Vitocal 300-G. Technical report, 2018.

[64] Paul Stadler, Araz Ashouri, and François Maréchal. Model-based optimization of distributed and renewable energy systems in buildings. *Energy and Buildings*, 120:103–113, 2016.

[65] Somil Miglani, Kristina Orehounig, and Jan Carmeliet. Design and optimization of a hybrid solar ground source heat pump with seasonal regeneration. *Energy Procedia*, 122:1015–1020, 2017.

[66] Thomas Hasler. A methodology for the optimal operation of a residential building's heating system with focus on thermal modelling of GSHPs. In *PROCEEDINGS OF ECOS 2017*, 2017.

[67] Chih Chien Tang. *Modeling Packaged Heat Pumps in a Quasi-Steady State Energy Simulation Program*. PhD thesis, Oklahoma State University,, 2005.

[68] Rasmus Halvgaard, Niels Kjølstad Poulsen, Henrik Madsen, and John Bagterp Jørgensen. Economic Model Predictive Control for building climate control in a Smart Grid. *2012 IEEE PES Innovative Smart Grid Technologies, ISGT 2012*, pages 1–6, 2012.

[69] J. A. Candanedo, V. R. Dehkordi, and M. Stylianou. Model-based predictive control of an ice storage device in a building cooling system. *Applied Energy*, 111:1032–1045, 2013.

[70] Farkhondeh Jabari, Behnam Mohammadi-Ivatloo, Mohammad Bagher Bannae-Sharifian, and Hadi Ghaebi. Short-Term Co-Optimization of Multi-Chiller Plants and Ice Storage System. *Proceedings - 2018 Smart Grid Conference, SGC 2018*, pages 1–6, 2018.

[71] A. Heidari, S. S. Mortazavi, and R. C. Bansal. Stochastic effects of ice storage on improvement of an energy hub optimal operation including demand response and renewable energies. *Applied Energy*, 261(September 2019):114393, 2020.

[72] Jonathan West and James E. Braun. Modeling partial charging and discharging of area-constrained ice storage tanks. *HVAC and R Research*, 5(3):209–228, 1999.

[73] Christian Winteler, Ralf Dott, Thomas Afjei, Bernd Hafner, and Viessmann Werke Gmbh. Heat Pump, Solar Energy and Ice Storage Systems - Modelling and Seasonal Performance. pages 1–12, 2014.

[74] Velasolaris. Polysun user manual. *Vela Solaris*, page 162, 2015.

[75] John A. Duffie, William A. Beckman, and Jon McGowan. *Solar Engineering of Thermal Processes*, volume 53. 2013.

[76] G. N. Tiwari, Arvind Tiwari, and Shyam. *Handbook of Solar Energy*. Energy Systems in Electrical Engineering. Springer Singapore, Singapore, 2016.

[77] Hong Li and Hongxing Yang. Potential application of solar thermal systems for hot water production in Hong Kong. *Applied Energy*, 86(2):175–180, 2009.

[78] Hansani Weeratunge, Guillermo Narsilio, Julian de Hoog, Simon Dunstall, and Saman Halgamuge. Model predictive control for a solar assisted ground source heat pump system. *Energy*, 152:974–984, 2018.

[79] Deutsches Institut für Normung e.V. DIN EN 12975 - Thermal solar systems and components, 2006.

[80] Luisa Cabeza. *Advances in Thermal Energy Storage Systems*. 2015.

[81] Rasmus Halvgaard, Peder Bacher, Bengt Perers, Elsa Andersen, Simon Furbo, John B. Jørgensen, Niels K. Poulsen, and Henrik Madsen. Model predictive control for a smart solar tank based on weather and consumption forecasts. *Energy Procedia*, 30:270–278, 2012.

[82] Thomas Schütz, Rita Streblow, and Dirk Müller. A comparison of thermal energy storage models for building energy system optimization. *Energy and Buildings*, 93:23–31, 2015.

[83] Rasmus Halvgaard. *Model Predictive Control for Energy Systems Management*. PhD thesis, Technical University of Denmark, 2014.

[84] Deutsches Institut für Normung e.V. DIN EN 41773 - Static power convertors; semiconductor rectifier equipment with IU-characteristics for charging of lead-acid batteries, guidelines, 1979.

[85] Despoina Christantoni, Simeon Oxizidis, Damian Flynn, and Donal P. Finn. Implementation of demand response strategies in a multi-purpose commercial building using a whole-building simulation model approach. *Energy and Buildings*, 131:76–86, 2016.

[86] Marcel Macarulla, Miquel Casals, Núria Forcada, and Marta Gangolells. Implementation of predictive control in a commercial building energy management system using neural networks. *Energy and Buildings*, 151:511–519, 2017.

[87] G. T. Costanzo, S. Iacovella, F. Ruelens, T. Leurs, and B. J. Claessens. Experimental analysis of data-driven control for a building heating system. *Sustainable Energy, Grids and Networks*, 6:81–90, 2016.

[88] H. Madsen and J. Holst. Estimation of continuous-time models for the heat dynamics of a building. *Energy and Buildings*, 22(1):67–79, mar 1995.

[89] Klaus Kaae Andersen, Henrik Madsen, and Lars H. Hansen. Modelling the heat dynamics of a building using stochastic differential equations. *Energy and Buildings*, 31(1):13–24, 2000.

[90] M. J. Jiménez, H. Madsen, J. J. Bloem, and B. Dammann. Estimation of non-linear continuous time models for the heat exchange dynamics of building integrated photovoltaic modules. *Energy and Buildings*, 40(2):157–167, 2008.

[91] Peder Bacher and Henrik Madsen. Identifying suitable models for the heat dynamics of buildings. *Energy and Buildings*, 43(7):1511–1522, 2011.

[92] Deutsches Institut für Normung e.V. DIN EN 12831 - Energy performance of buildings, 2017.

[93] K.R. Godfrey. Correlation Methods. In *5th IFAC Symposium on Identification and System Parameter Estimation*, volume 16, Darmstadt, 1980. Pergamon Press Limited.

[94] Administration des Services techniques de l'agriculture. AgriMeteo, 2010.

[95] José M Cejudo-López, Antonio Carrillo-Andrés, Fernando Domínguez-Munoz, and Manuel Gallardo-Salazar. Selection of typical demand days for CHP optimization. *Energy and Buildings*, 43:3036–3043, 2011.

[96] Sobrina Sobri, Sam Koohi-Kamali, and Nasrudin Abd Rahim. Solar photovoltaic generation forecasting methods: A review. *Energy Conversion and Management*, 156(November 2017):459–497, 2018.

[97] Deutsches Institut für Normung e.V. DIN EN 50530 - Overall efficiency of photovoltaic inverters, 2009.

[98] Ralf Dott, Michel Yaller, Jörn Ruschenburg, Fabian Ochs, and Jacques Bony. The Reference Framework for System Simulations of the IEA SHC Task 44 / HPP Annex 38. Technical report, Fachhochschule Nordwestschweiz, Muttenz, 2013.

[99] Creos. Versorgung der Kunden auf Grundlage synthetischer Lastprofile, 2020.

[100] Deutsches Institut für Normung e.V. DIN EN 16147 - Heat pumps with electrically driven compressors, 2017.

[101] Jonathan Hadji-Minaglou. Temperature measurement and acquisition with PT100 thermocouples. Technical report, University of Luxembourg, Luxembourg, 2017.

Appendices

Appendix A

Piping and Instrumentation Diagram

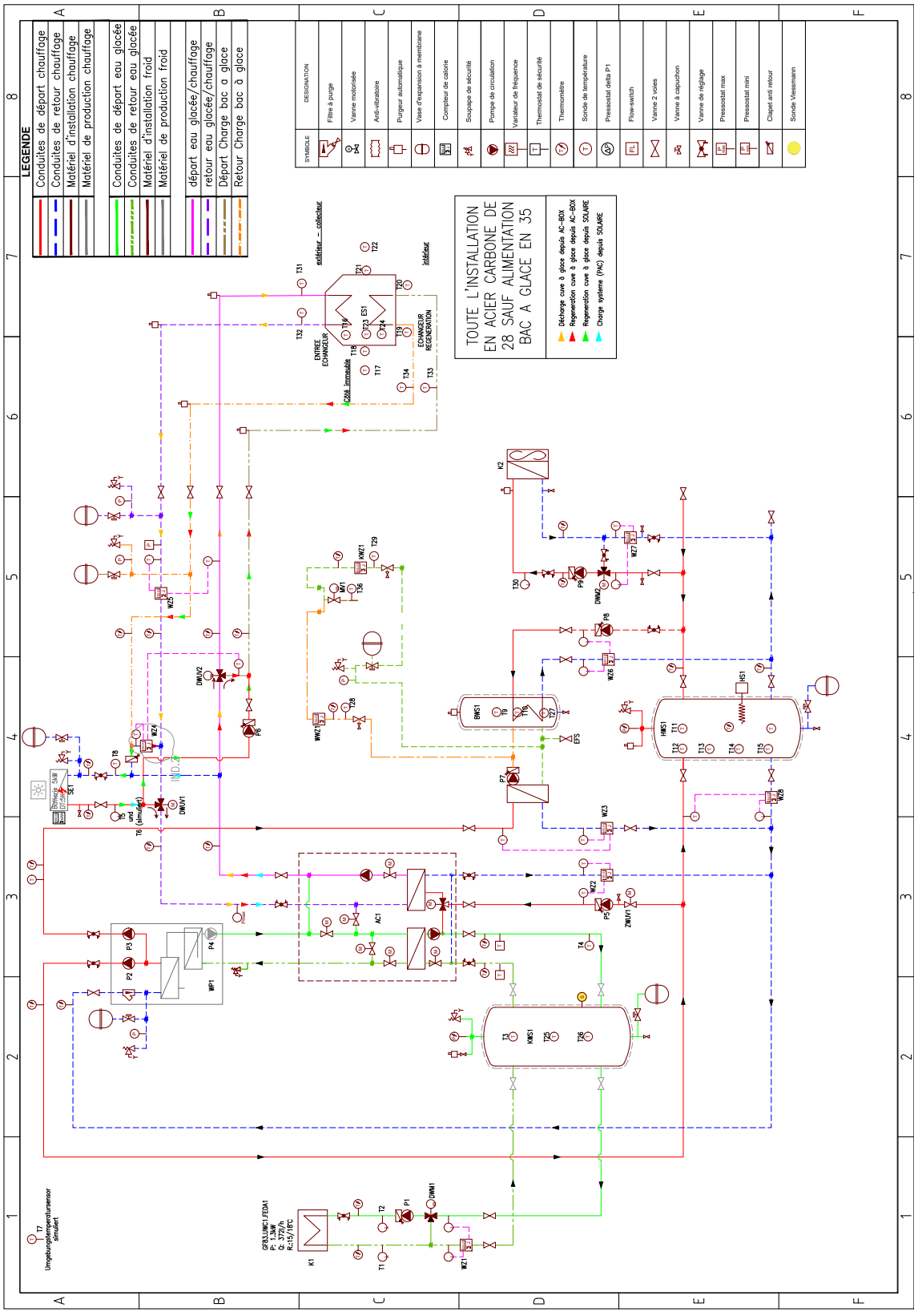
LEGENDE
Conduites de départ chauffage
Conduites de retour chauffage
Matériel d'installation chauffage
Matériel de production chauffage
Conduites de départ eau glacée
Conduites de retour eau glacée
Matériel d'installation froid
Matériel de production froid
départ eau glacée/chauffage
retour eau glacée/chauffage
Départ Charge bac a glace
Retour Charge bac à glace
SYMBOLE
DESIGNATION
Filtre à purge
Vanne motorisée
Anti-vibrateur
Purgeur automatique
Vase d'expansion à membrane
Compteur de calorie
Soupape de sécurité
Pompe de circulation
Variateur de fréquence
Thermostat de sécurité
Thermomètre
Sonde de température
Pressostat delta P1
Flow-switch
Vanne 2 voies
Vanne à capuchon
Vanne de réglage
Pressostat max
Pressostat mini
Clapet anti retour
Sonde Viessmann
TOUTE L'INSTALLATION EN ACIER CARBONE DE 28 SAUF ALIMENTATION BAC A GLACE EN 35
Décharge cuve à glace depuis AC-BOX
Regeneration cuve à glace depuis AC-BOX
Regeneration cuve à glace depuis SOLAIRE
Charge systeme (PAC) depuis SOLAIRE
extérieur — collecteur
intérieur
ENTREE ECHANGEUR
ECHANGEUR REGENERATION
Cuve immeuble
Umgebungstemperatursensor simuliert
GRS3.LWK1.FEDA1
P1 1 bar
Q: 372l/h
R:+15/18°C
Bivalenz SWT
Bivalenz WT
und (simuliert)
WD...
DWUV1
DWUV2
ZWUV1
DWM1
DWM2
WP1
AC1
KWS1
BWS1
HWS1
KWZ1
WWZ1
WWZ2
EPS
HS1
WZ1
WZ2
WZ3
WZ4
WZ5
WZ6
WZ7
WZ8
P1
P2
P3
P4
P5
P6
P7
P8
P9
K1
K2
T1
T2
T3
T4
T5
T6
T7
T8
T9
T11
T12
T13
T14
T15
T16
T17
T18
T19
T20
T21
T22
T23
T24
T25
T26
T27
T28
T29
T30
T31
T32
T33
T34
ES1
SW
A
B
C
D
E
F
1
2
3
4
5
6
7
8